High Fidelity Radiative Thermal Transport Simulations of a Scramjet Propulsion System

by

Adam Glenn Irvine

A dissertation submitted in partial fulfillment
of the requirements for the degree of
Doctor of Philosophy
(Aerospace Engineering)
in The University of Michigan
2013

Doctoral Committee:

Professor Iain D. Boyd, Chair
Assistant Professor Krzysztof Fidkowski
Dr. Nicholas Gentile
Professor Edward Larsen

For Derek, Lena, and Solveig

ACKNOWLEDGEMENTS

Finally, I thank my wife Solveig. I don't think either of us knew what we were getting ourselves into when we came here, but I know I couldn't have done it without her. She has been there with me every step of the way and I don't know that I can ever repay her for everything she has done for me. I'm grateful to have such a wonderful partner as we go into the next phase of our lives.

TABLE OF CONTENTS

LIST OF FIGURES

CHAPTER I

Introduction

This chapter provides the motivation and background information for this dissertation. The objectives of the thesis are discussed and the organization of the remaining thesis is presented.

1.1 Motivation

Scramjets have the potential to provide thrust for atmospheric vehicles at high speeds. A scramjet is a type of air-breathing propulsion system that produces thrust through the combustion of air and fuel at speeds exceeding the speed of sound, or Mach 1. Figure 1.1 shows that this type of propulsion system is capable of efficient operation from speeds of Mach 5 to over Mach 20, where specific impulse is a measure of the thrust produced by the system per unit weight of propellant used per unit time. Slowing down incoming airflow to subsonic speeds, as for turbojets and ramjets, reduces engine efficiency at high Mach number. Additionally, this deceleration results in high pressures and temperatures inside the propulsion system that can exceed the mechanical and thermal limits of practical designs[61]. At high Mach numbers, scramjets are more efficient than rocket based propulsion systems, which carry both fuel and oxidizer within the vehicle. There are a number of civilian and military applications for vehicles that can operate at hypersonic speeds including: fully or
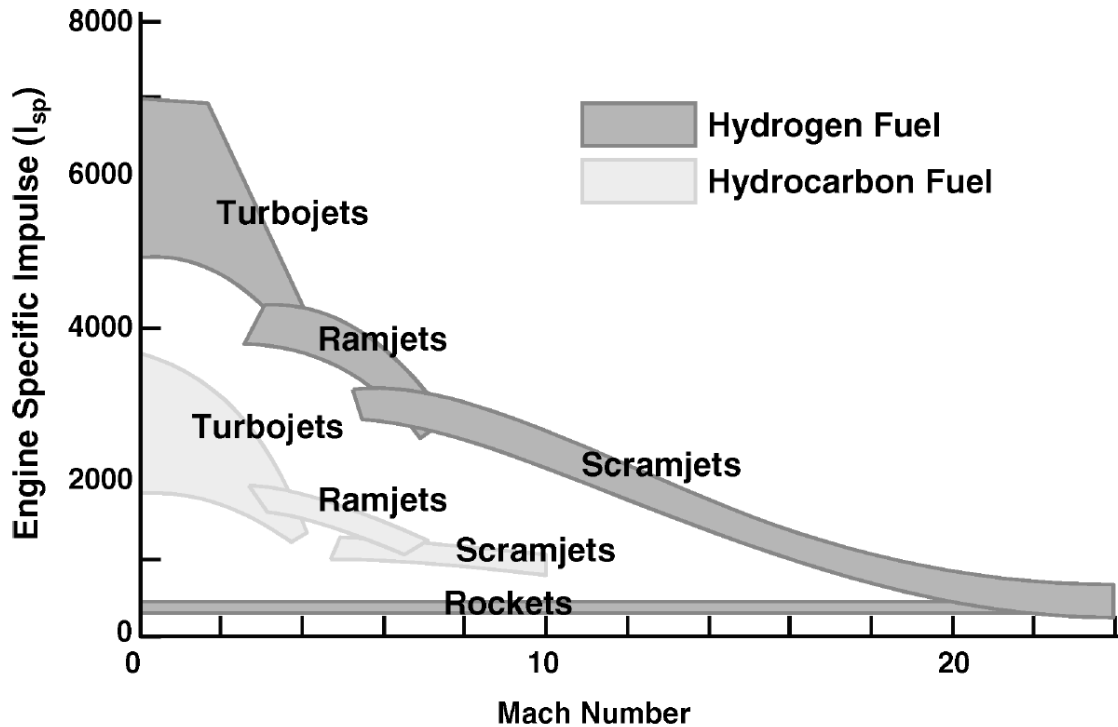
Figure 1.1: Performance of propulsion systems as a function of Mach number[19]

partially reusable single or two stage to orbit launch systems, tactical and strategic hypersonic missiles, and hypersonic transports.

Since initial experiments in the 1960s, there has been limited experimental testing of scramjets, and few successful flight tests achieving steady operation. Section 1.2.2 provides a brief history of notable test programs. Figure 1.2 shows a schematic of a scramjet combustion chamber. There are no moving parts within the engine, relying upon the geometry of the inlet and the speed of the vehicle to compress air for combustion. The isolator region isolates the inlet flow from the pressure rise within the combustion chamber due to the combustion of fuel and air. The nozzle allows the heated flow to accelerate while it expands.

Heat release in the combustor leads to an increase in pressure which, if large enough, can cause thermal choking resulting in a mass-flow reduction that can propagate to the inlet causing subsonic flow throughout the scramjet. This process is

2
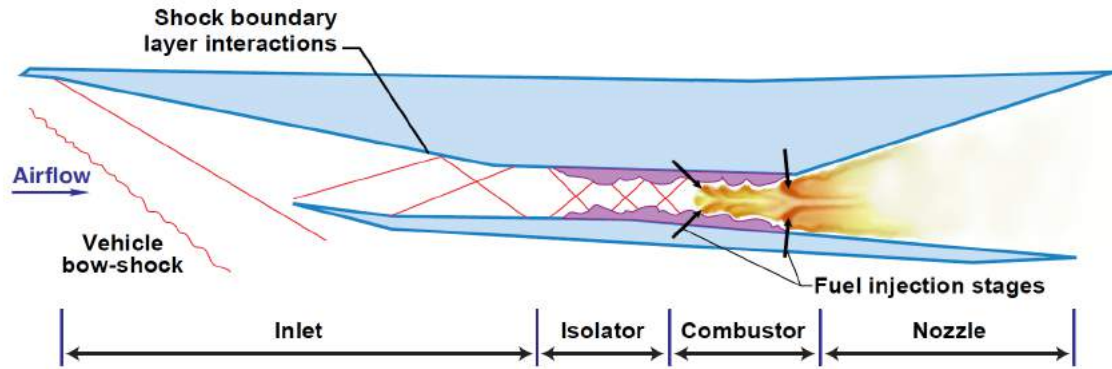
Figure 1.2: Schematic of a scramjet propulsion system[48]

called *unstart*. Figure 1.3 illustrates the propagation of an unstart event triggered by downstream mass addition. The dark portions of the flow indicate where the flow is subsonic. The initial image shows the shockwaves formed from the inlet and subsequent reflected shocks, and with the exception of the boundary layer near the wall, the flow is supersonic. Once mass injection starts a shock starts to propagate upstream followed by separated flow until the inlet is reached. This process occurs rapidly and results in a large loss of engine efficiency, potentially leading to complete flame out. Ramjets are similar to scramjets except that combustion takes place at subsonic speeds, and can also undergo unstart. From accounts of pilots in the ramjet powered A-12 program, the unstart process is rapid followed by dramatic loss of thrust constituting a "severe and serious emergency[22]." In order to specify safe operating conditions of a scramjet propulsion system, it is necessary to predict the limiting conditions where unstart is likely.

Experiments involving flight vehicles are expensive, even more so to conduct enough experiments to sample the design space. Sampling the design space using ground tests is more feasible; however, it is not practical to fully replicate the flight operating conditions for the complete flight vehicle. To date, accurate computational simulations including all of the relevant physics and unsteady phenomena have not been verified. It is the goal of the Stanford University Predictive Science Academic Al-

4 ms

7 ms

9 ms

12 ms

14 ms

14.5 ms

15 ms

19 ms

←Jet (R ~ 3.5)

←——Flow
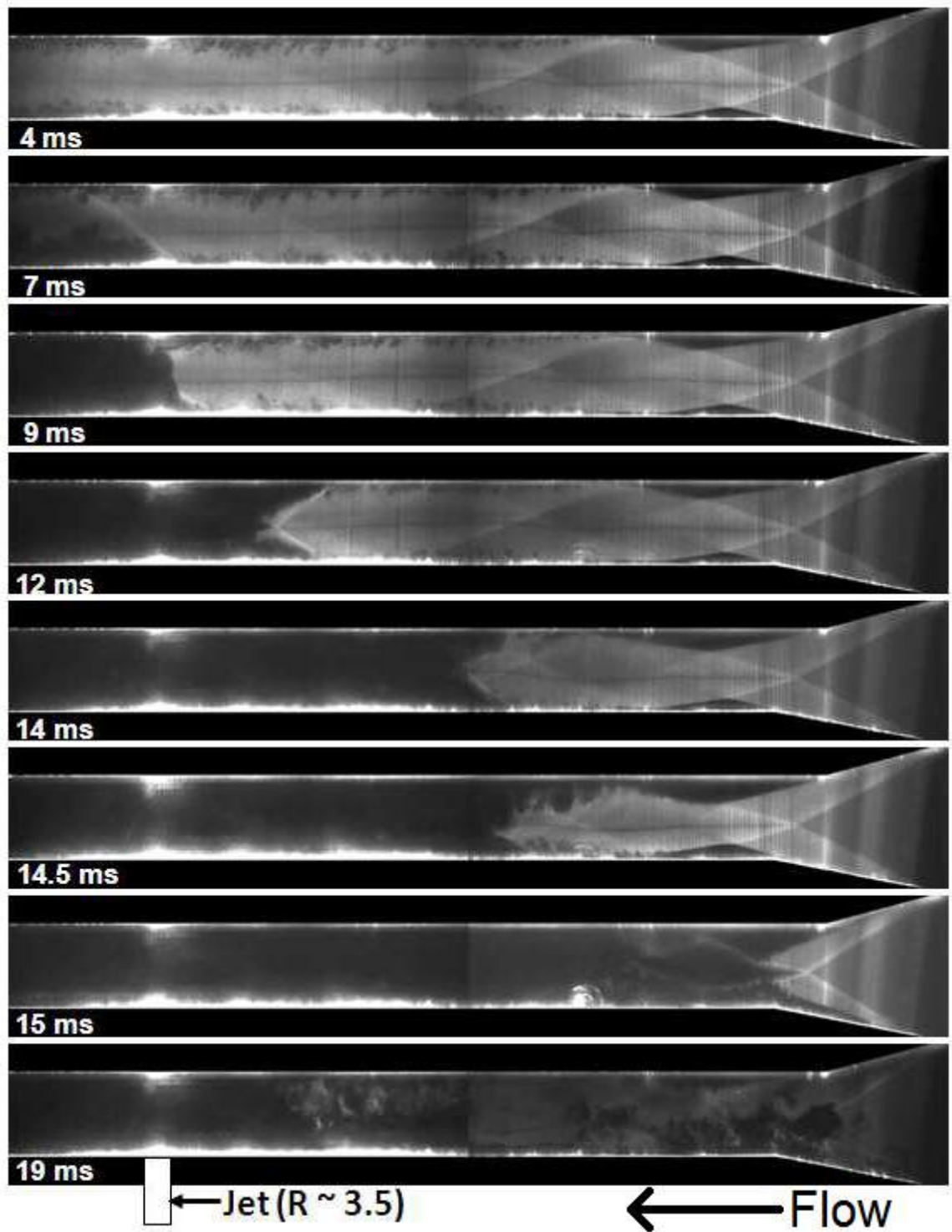
Figure 1.3: Time evolution of unstart triggered by mass addition[15]

liance Program (PSAAP) Center to improve computational predictions of a scramjet propulsion system and quantify its operational margins using experimentally validated computational models. These models and their input parameters are typically not exactly known, and have some level of uncertainty. The propagation and potential coupling of these uncertainties produce some level of uncertainty in the prediction of the onset of unstart. Therefore, the quantification of the uncertainty of unstart conditions is necessary to describe the safe operating conditions of a scramjet, and is part of the Stanford PSAAP Center's goal. There is further discussion of uncertainty quantification efforts in section 1.2.1.

In high temperature systems, thermal radiation can account for a significant fraction of the overall heat transfer. The combustion of fuel and air within the scramjet combustion chamber generates high temperatures and radiatively active species. This thesis is motivated by the quantification of the uncertainty in radiative simulations applied to a scramjet propulsion system. The radiative models utilized in this thesis are chosen based on the goal of minimizing the uncertainty of radiation simulations produced. The uncertainty of radiative solutions due to the methods used, and known uncertainties of the input parameters are quantified. Finally, a method of reducing uncertainty in radiative solutions is presented and its performance relative to common mitigation techniques assessed. An introduction to the methods used in this thesis and a review of studies on radiative thermal transport in a scramjet flow environment are presented in sections 1.2.3 and 1.3, respectively.

1.2 Background

This section provides background information on uncertainty quantification methods used by the Stanford PSAAP Center, scramjet propulsion systems, and thermal radiation and modeling techniques.

1.2.1   Uncertainty Quantification

Results from physical experiments are typically reported with some estimation of the uncertainty in the measurements. Experimental errors are caused by a number of factors including: finite accuracy of instruments, imprecision in the experimental setup (e.g. manufacturing tolerances, inconsistent performance of equipment), variability in the experimental environment (e.g. temperature, humidity, electrical noise, vibrations), unknown variables, and stochastic processes influencing the results. The influence of these errors are typically accounted for by quantifying the variation in the results of several experiments if possible, or applying an uncertainty found using the instrumentation in a similar environment.

Results from numerical studies are often reported using only the expected values of input variables. This approach ignores the inherent variability of the physical input parameters of a numerical simulation that cannot be eliminated completely, even from the most rigorously controlled experimental setup. In verification studies of numerical models, it is important to verify not only the accuracy of the expected value of the simulation, but that the variability of the simulation behaves in a manner consistent with observed experimental behavior. Additionally, to assess the quality of a numeric simulation, it is necessary to estimate the uncertainty introduced by the numerical model used.

As numerical models improve, and are used to predict the behavior of systems in lieu of experiments, it is important to quantify the sensitivity of numeric results to variations likely to be seen by a system in a real environment. Such an assessment can account for potentially undesirable behaviors of a system exposed to likely variations in environmental variables. Another potential benefit of uncertainty quantification results from coordination between numeric and experimental efforts. A sensitivity analysis of an experiment can highlight variables with the largest influence on uncertainty of the quantity of interest. This knowledge can be used to modify the

experiment to reduce the uncertainty in the experimental results.

Uncertainty can be classified as being either aleatory, or epistemic. Aleatory uncertainties are the result of the stochastic nature of the physical phenomena being modeled, and cannot be eliminated. If the process producing an aleatory uncertainty is known, then a probability distribution function can be used to describe the character of the uncertainty. Epistemic uncertainties are those uncertainties that in principle could be reduced, but typically are not due to factors such as a lack of accurate experimental data, use of approximate models, and incomplete knowledge of the physical phenomena being modeled. Since epistemic uncertainties are based upon a lack of knowledge, the distribution of these uncertainties is often described by an interval[62].

The Stanford PSAAP Center quantifies the simulation response to these types of uncertainties separately. Furthermore, the epistemic numerical uncertainty due to spatial discretization is treated separately from the epistemic uncertainties due to the computational models. Figure 1.4 shows how these three uncertainties are sampled. For each sampling of aleatory uncertainty, the epistemic modeling uncertainties are sampled, and for every one of those samples the epistemic numerical uncertainty is estimated. The aleatory uncertainty is sampled for a number of points, and the response of the solution is fitted to a surface to estimate the error due to using a finite number of samples. Epistemic modeling uncertainties are sampled depending on the source of the uncertainty. For uncertain epistemic parameters, the response of the solution to parameter variation is sampled and a response surface generated. A minimum uncertainty due to the use of approximate models is found by using the maximum and minimum results for two different approximate models. Finally, epistemic numerical error is estimated using two spatial grids at different resolutions, interpolating the coarse grid solution onto the fine grid solution, and weighting the residual of the solution by an adjoint solution to estimate the spatial discretization
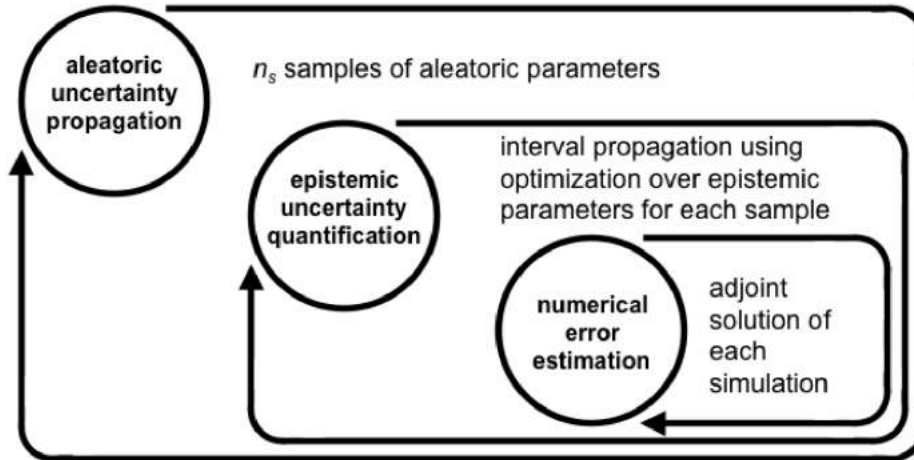
Figure 1.4: PSAAP nested uncertainty quantification loop[70]

error[70].

In addition to quantifying the uncertainty of numeric solutions, the Stanford PSAAP Center is reducing the epistemic uncertainty of their simulations through model development and reducing the uncertainty of some input parameters through physical experiments. Figure 1.5 shows a schematic illustrating the Stanford PSAAP Center goals. On the left is a plot of the expected value of scramjet thrust over time in blue at different fuel flow levels with an uncertainty in gray. At too low of a fuel flow rate, the scramjet will produce little to no thrust, and at too high of a rate the scramjet will unstart. The design margin is the amount of allowable thrust over the predicted solution. On the right is the desired outcome of refining the numerical models with the blue line representing the uncertainty of a lower fidelity model, and the red line representing the uncertainty of an improved model[6].

The availability of experimental data for the system being simulated is crucial to assessing the accuracy of computational predictions, especially for complex systems. For simple systems, there are analytical solutions that can be used for verification of solutions using computational models. However, a scramjet combustion environment is complex, involving fluid dynamics with turbulence, chemical kinetics and reactions, heat transfer, and the coupling of these phenomena. The availability of flow data

8
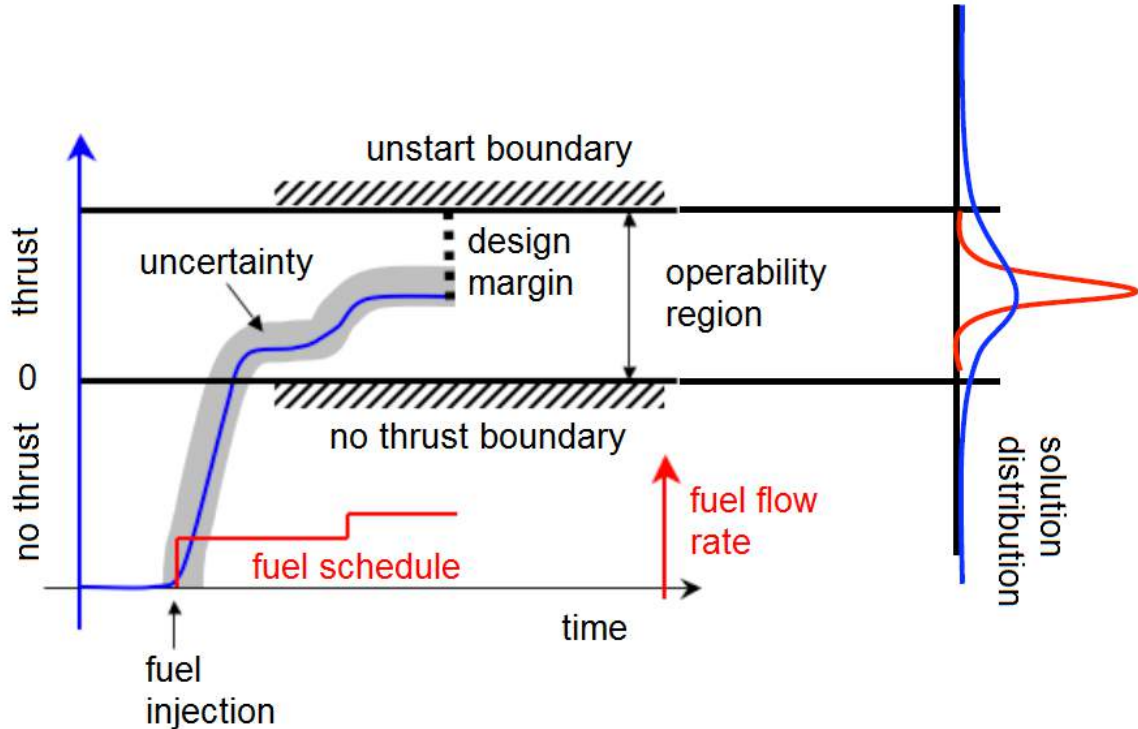
Figure 1.5: Schematic illustrating the PSAAP goal

drives the selection of the scramjet propulsion systems used for validation of the Stanford PSAAP Center numeric simulations.

1.2.2 Scramjet Propulsion Systems

While the first experimental demonstrations of steady supersonic combustion took place in the late 1950s, outside of short experimental tests there have been no operational scramjet engines produced as of today[19]. The United States Air Force (USAF) funded a hydrogen fueled scramjet concept, the Incremental Flight Test Vehicle (IFTV), that was used in ground testing experiments in the late 1960s. Interactions between the combustion chamber and inlet led to delays in the program, and the program was canceled in 1967. However, an un-powered flight test was launched in 1967[14]. The NASA Hypersonic Research Engine (HRE) project was started in 1964, and was intended to fly on the X-15A-2 aircraft. The X-15 program was canceled before a flight could occur, but extensive ground testing totaling over two hours of test

time produced valuable data on two scramjet configurations until the HRE project was canceled in 1974[61]. The National Aerospace Plane (NASP) was conceived in the early 1980s as a single stage to orbit hypersonic vehicle. The NASP program made advancements in materials research, and in a number of enabling supporting technologies for an operational hypersonic vehicle, as well as advances in computational simulations before it was restructured in 1993 and canceled in 1995[9]. Hypersonic scramjet tests in the T3 facility at the Australian National University in 1981 transitioned to the T4 tunnel at the University of Queensland in 1987. Experimental work evolved from basic combustor chambers to complete scramjet models, leading to a successful hydrogen fueled scramjet propulsion flight test of the Hyshot II vehicle on 30 July 2002[50]. In addition to data from the flight experiment, there is data available from ground tests performed at the German Aerospace Center (DLR)[58]. The USAF HyTech program started after the NASP program was canceled and led to the X-51 test program that has had two partially successful flight tests in 2010 and 2012 with one failure in 2011. The NASA Hyper-X program was also started after the end of the NASP program, and lead to the development of the X-43, which had one failure in 2001 and two successful flight tests in 2004. HIFiRE is a flight test program of a hydrocarbon fueled scramjet propulsion system that is part of a joint effort between the United States Air Force Research Laboratory (AFRL) and the Australian Defense Science and Technology Organization (DSTO)[28]. There is experimental data available from ground tests for the HIFiRE-2 scramjet combustion chamber, collected at the NASA Langley Research Center[26].

Developing a successful scramjet design requires knowledge of a number of physical phenomena which need to be accounted for to predict the operation of a scramjet. The types of flow interactions in a scramjet include turbulent and laminar flow interactions, turbulent mixing, turbulent boundary layer interactions with shockwaves, shockwave interactions with other shockwaves, and boundary layer separation. The

presence of fuel combustion requires knowledge of chemical reaction rates, heat release, wall catalysis, and flame ignition and quenching. Additionally, numerical simulations must be time dependent to capture scramjet unstart behavior. Numerical models of these physical features must be validated against experimental data to ensure the accuracy of simulations employing those models. The need for available experimental data leads to the selection of the HyShot II and HIFiRE-2 scramjet vehicles as the systems of interest for the Stanford PSAAP Center. Flight and ground testing experimental data taken at hypersonic speeds are available for both of these systems. Additionally, the geometry and operational variables of both HyShot II and HIFiRE-2 are publicly available.

1.2.3 Thermal Radiation

While radiative transport includes many physical phenomena across the electromagnetic spectrum, the discussion here is limited to thermal radiation resulting from the temperature of a material. All molecules with a temperature above 0K emit thermal radiation as a result of fluctuations in the kinetic energies of molecules causing changes in the internal energies of those molecules. There are two computational methods used to simulate the radiative thermal transport equations described in this thesis that are capable of simulating the transport equations to an arbitrary accuracy. For both methods, the spatial domain is segmented into a number of spatial cells that have discrete thermodynamic values representing the medium inside the cell. The deterministic method described is the Discrete Ordinates Method (DOM), which discretizes the transport equations into a number of angular directions[8]. The radiative thermal transport of the system is determined by solving the coupled system of equations across the angular and spatial domains. The stochastic method described in this thesis is part of a class of methods called Monte Carlo Methods (MCM) that utilize random numbers, typically simulated by software, to determine the outcome

11

of discrete interactions of particles that represent the radiation, with the medium[29]. The sum of the energy exchanged in particle interactions within the medium is the radiative heat flux solution.

In addition to the thermodynamic properties of the medium, a radiative thermal transport simulation requires knowledge of the response of the medium to radiation. Emission and absorption of thermal radiation by a molecule is tied to changes in the molecule's internal energy states. These transitions emit or absorb photons at a discrete frequency, or absorption line, that is spread out due to broadening effects. The most accurate model of these phenomena is the Line By Line (LBL) model, which uses observed and theoretical data on the characteristics of a large number of internal energy transitions to calculate the average probability of photon-molecule interactions over a path through the material, or absorption coefficient[68]. The large number of internal energy transitions that need to be considered for each species makes the use of the LBL model for every radiative interaction in a transport simulation computationally prohibitive. In this thesis, tables are constructed describing the interaction of radiation with the medium across a range of thermodynamic conditions representative of the medium within the HIFiRE-2 scramjet combustion chamber. These tables only need to be constructed once, with the absorption coefficients for a particular interaction interpolated from the tables.

The correlated-k method discretizes the absorption coefficient into a number of ranges with the number of absorption coefficient values that fall into a range represented by the variable k[46]. The cumulative distribution of k is well behaved and can be represented by a relatively small number of points. Using a large number of points to characterize the cumulative k distribution, the correlated-k method approaches the accuracy of the LBL method. The narrow band model discretizes the spectral domain into a number of ranges, where the absorption coefficient is approximated by its integral across the range, while making an assumption about the overlap of the

absorption coefficients. The wide band model is similar to the narrow band model except that the absorption coefficients are integrated for each internal vibrational mode of the species considered[65]. A gray model assumes that the absorption coefficient is constant. Finally, the weighted sum of gray gases model divides a spectrally resolved solution into a number of gray gas problems using weighted coefficients to represent the spectral properties[44].

The MCM is flexible in terms of spatial geometry and physical mechanics considered. Additionally, the method is simple to parallelize in order to distribute computational loads onto multiple computer processors and scales well as the number of computer processors utilized is increased. By increasing the number of particles in the simulation, the solution will approach the exact solution of the transport problem. However, the expected error of the simulation converges at a rate proportional to $1/\sqrt{N}$, where N is the number of particles used in the simulation. Since the computation time required for a simulation scales with N, this convergence rate can result in high computational costs when a low error in the solution is desired.

Time dependent MCM simulations of particle transport including stochastic particle emissions can exhibit a dependence of the solution on the spatial resolution of the domain. This error is called *teleportation error,* as it causes energy absorbed in one location to be "teleported" to another location in subsequent time steps. Typically, this error is mitigated in radiative thermal transport by using a method called *source tilting,* which samples particle emission locations from a linear distribution of T^4 across the neighboring spatial cells.

The DOM is capable of solving the entire problem domain at once over a number of discrete directions. An arbitrary level of accuracy can be achieved by increasing the number of directions used. However, use of a large number of directions quickly increases computational costs, and complexity of the spatial domain further increases this cost. The DOM involves the solution of a system of linear of equations, which

results in relatively poor parallel scaling. Furthermore, while the MCM can stochastically sample spectral property tables across the frequency domain, a DOM solution must be repeated for every frequency value.

In the next section it is shown that the contribution of radiative heat flux relative to the total heat flux is predicted to be small for some scramjets. When the radiative heat flux in a flow is small compared to convective heat flux, the interactions between turbulence and radiation can be neglected[16]. When this is the case, radiation can be modeled independently from the other physical phenomena in the overall simulation of a scramjet combustor environment. Radiative heat flux can then be used as a source term in the overall simulation and updated as needed to achieve convergence of the simulation.

1.3   Review of Prior Studies of Radiation in Scramjets

The first known investigation of the effects of radiation on a chemically reacting flow relevant to a scramjet is by Mani and Tiwari[38]. The system is a two dimensional channel and the incoming flow is stoichiometric premixed hydrogen and air. This mixture ignites upon interacting with the shock created by the ramp and produces radiatively active species. The radiation field is treated as a one dimensional slab, and a wide band model is used to quantify spectral properties. Figure 1.6 shows the channel dimensions and conditions on the left, and a solution for the temperature of the medium at two locations. These results predict significant radiative heating of the boundary layer, which has a relatively low speed compared to the free stream flow. Mani and Tiwari also conclude that increasing the flow speed or the size of the system will increase the radiative heat transfer. The models used by Mani and Tiwari are greatly simplified, and it is likely that there is significant uncertainty in the results.

A study by Nelson shows the radiative thermal transport from an averaged rep-
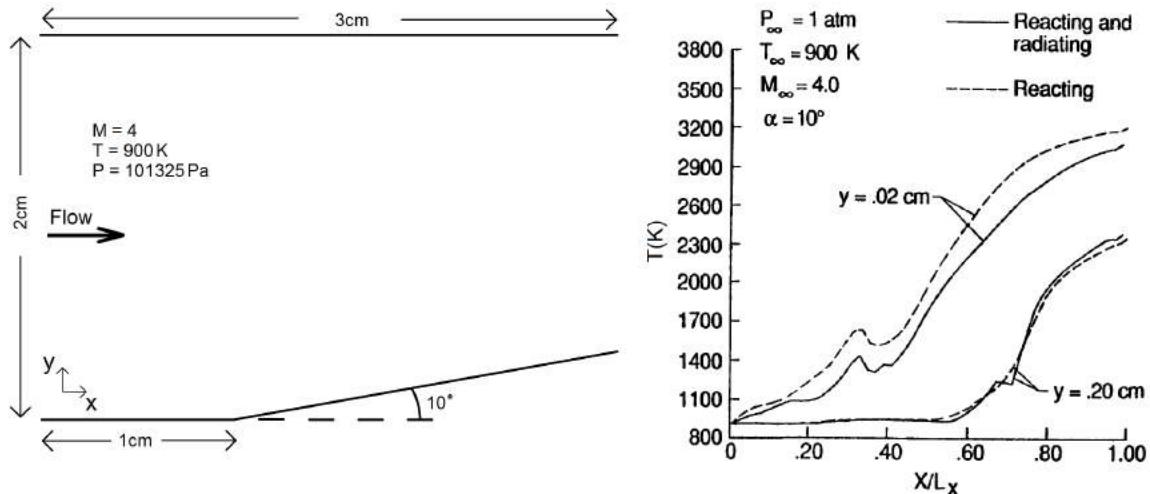
Figure 1.6: Problem domain and temperature plot by Mani and Tiwari[38]

resentation of the combustion gases in a hydrogen fueled rectangular scramjet[49].
Figure 1.7 shows the scramjet configuration on the left, and on the right is a plot
of the spectrally resolved radiative heat flux for three different combustion chamber
widths showing the increase in radiative flux with increasing combustion chamber
volume. Flow conditions for three different Mach numbers are used for radiative flux
calculations. Comparisons of total radiative heat flux to the estimated convective heat
flux for these cases show that radiation accounts for between 5 and 11 percent of the
wall heat flux. Given the uncertainty that is introduced by neglecting the spatial de-
pendence of the thermodynamic properties, this study provides more of a qualitative
assessment of the radiative thermal transport in a scramjet than quantitative.

Research by Tiwari, Pidugu, and Mohieldin characterizes the response of radiation
solutions to the variation of Mach number, equivalence ratio of hydrogen and oxygen,
and nozzle geometry[66]. Figure 1.8 shows the problem geometry on the left and
the solutions for radiative and convective heat flux at different Mach numbers on the
right. Radiative heat flux is predicted to be dominant in this problem and increasing
in magnitude with increasing Mach number. The radiation field is assumed to be a
one dimensional slab with a gray gas spectral model, which are very simplified models.

15
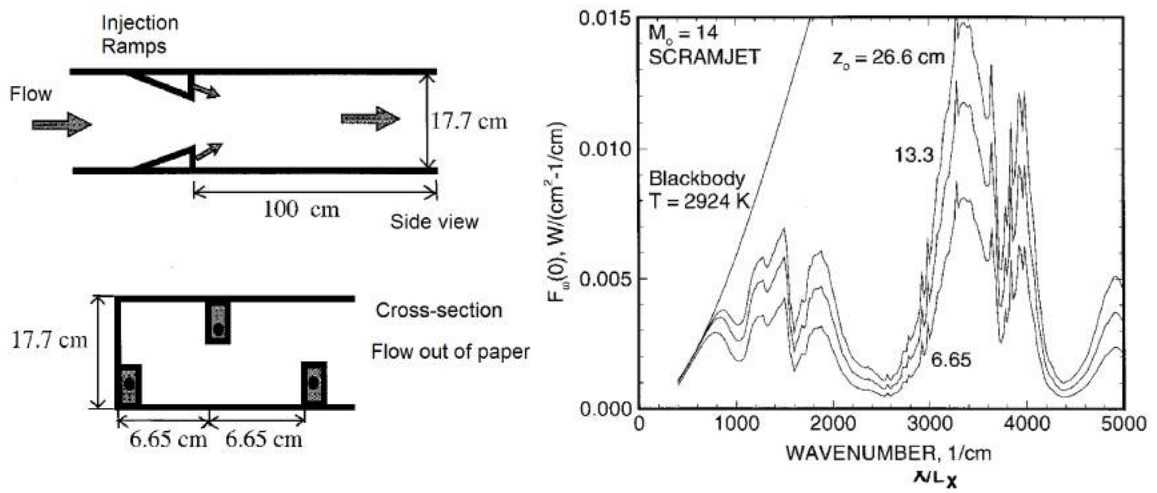
Figure 1.7: Nelson problem domain and radiative heat flux for different scramjet widths[49]
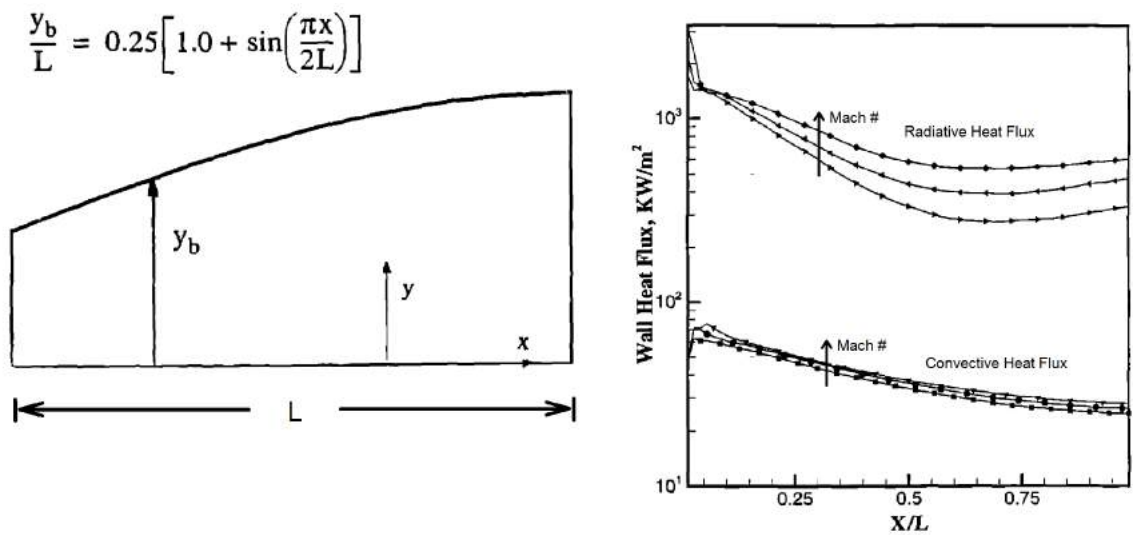
Figure 1.8: Problem and comparison of radiative and convective heat flux[66]

16
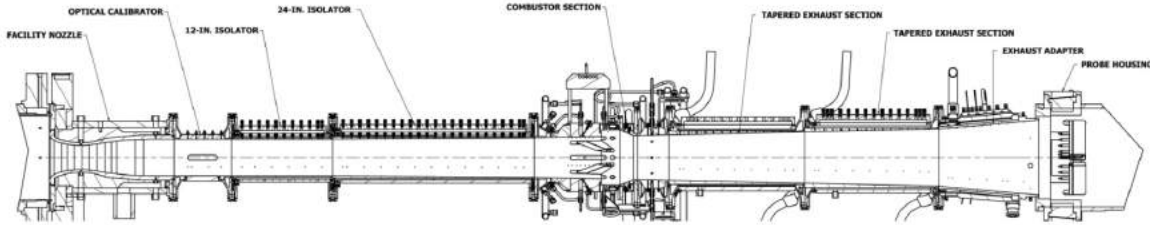
Figure 1.9: AFRL RC22 axisymmetric scramjet schematic[35]

A study by Liu and Brown reports on radiative thermal transport simulations of an axisymmetric scramjet design[35]. Figure 1.9 shows a schematic of the Air Force Research Laboratory (AFRL) RC22 hydrocarbon fueled scramjet which is approximately 100 inches long. Liu and Brown simulate radiative thermal transport using a weighted sum of gray gasses model to provide spectral properties to a discrete ordinates method transport model using an S_8 quadrature scheme. In addition to simulations of the current experimental geometry, a geometry with a factor of ten higher inlet mass flow is considered, in anticipation of future testing of larger scramjets. Radiative heat flux is shown to account for four percent of the total heat flux for most for the RC22 geometry. Contributions to the heat flux from radiation can exceed ten percent for the enlarged geometry. The minimum epistemic uncertainty of the transport model is estimated to be under seven percent by comparing the angular discretization scheme used in the reported solutions to a high resolution discretization solution. A solution using the spectral model is compared to a similar weighted sum of gray gases model that uses more spectral points to find a minimum epistemic uncertainty of under 19 percent.

As part of the Stanford PSAAP Center effort, Crow is investigating the radiative thermal transport of the HyShot II and HIFiRE-2 scramjets[13, 12]. The discrete ordinates method and a narrow band spectral model are used for simulations of the HyShot II scramjet. Figure 1.10 shows a schematic of the hydrogen fueled HyShot II scramjet highlighting the components of the vehicle as well as features in the
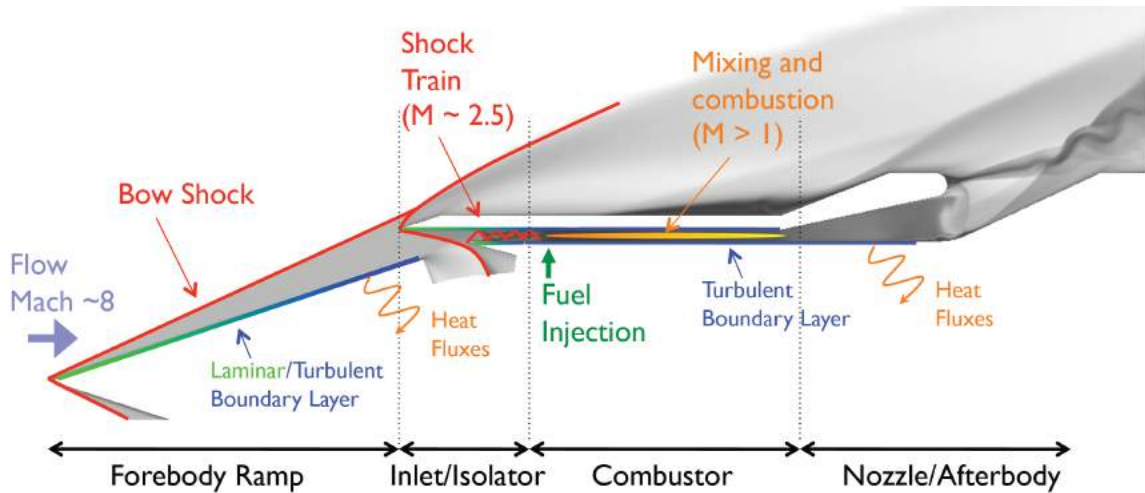
Figure 1.10: Hyshot II schematic[47]

flow. One dimensional simulations performed at a number of locations show that the radiative heat flux contribution is under a tenth of a percent of total heat flux. Crow shows through hypothetical simulations of larger Hyshot II scramjet geometries that the radiative heat flux increases by an order of magnitude. In a separate analysis, a ray tracing method solves the radiative thermal transport equations at a point by solving a large number of independent one dimensional problems along rays emanating from that point. This method is used to find the three dimensional solution at points used for the one dimensional simulations. This solution is used to quantify the epistemic uncertainty of the transport method, as well as from using a one dimensional representation of the domain.

Crow uses the more accurate correlated-k spectral model for radiative heat flux simulations of the hydrocarbon fueled HIFiRE-2 scramjet[13]. Figure 1.11 shows a cutaway of the HIFiRE-2 flight vehicle identifying the major components of the scramjet. Crow's radiation simulations of this system are in three dimensions and include the combustor and nozzle. Radiative heat flux is shown to typically contribute between one and ten percent of the total heat flux. Epistemic uncertainties of the three dimensional simulations are modeled using uncertainties found for one dimensional problems. The impact of uncertainties in the data used to create the
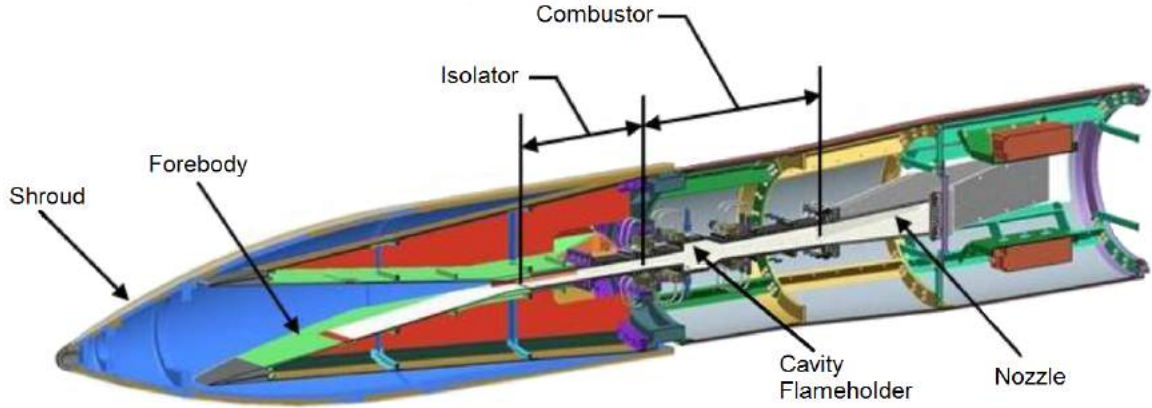
Figure 1.11: HIFiRE-2 vehicle cutaway[28]

Species	Normalized flux
H_2O	0.774
CO_2	0.208
OH	0.007
CO	0.001

Table 1.1: Normalized average radiative flux

correlated-k model are assessed by applying a constant assumed error of ten percent to the spectral model. Table 1.1 lists the normalized average radiative heat flux due to four radiative species considered by Crow[11].

1.4   Thesis Objectives

Due to the greater importance of radiation in the HIFiRE-2 scramjet, this system is the main focus of radiative thermal transport simulations for the Stanford PSAAP Center, and this thesis. While the relative contribution of radiation to the total heat flux for the HIFiRE-2 scramjet is higher than for HyShot II, the magnitude of the contribution is still low. AFRL has conducted computational simulations of the fluid dynamics of the flow, including turbulence and chemical reactions, for HIFiRE-2 scramjet ground tests. These simulations quantify thermodynamic properties of the flow, which are used as inputs for radiation simulations in this thesis.

The objectives of this thesis are outlined in the following sections

1.4.1 High Fidelity Simulation of Radiative Thermal Transport in the HIFiRE-2 Scramjet

While the work by Crow uses the most accurate models of radiation that have been applied to a scramjet environment that can be found in literature, these models still contain an unknown quantity of epistemic error. This thesis applies high accuracy radiative thermal transport simulation methods to a scramjet combustion chamber environment to produce radiative simulations with minimal epistemic uncertainty. The most accurate and flexible transport method for radiative thermal transport is the Monte Carlo Method (MCM), which is implemented in a modular, parallel, and efficient computer code as a part of this work. In order to produce accurate radiative simulations, an accurate model of the interactions between radiation and matter is required. The Line By Line (LBL) model is the most accurate spectral model available, but accurately computing interaction probabilities is impractical for every particle interaction in a MCM simulation. This thesis utilizes high resolution tables calculated by the LBL method at a sufficient number of thermodynamic conditions to ensure accurate calculation of absorption coefficients within the HIFiRE-2 scramjet flow field. This work utilizes these models to produce a reference solution of the radiative thermal transport of the HIFiRE-2 scramjet due to water vapor.

While it would be desirable to use the MCM to produce the solution data, uncertainty, and a sensitivity analysis of the radiation solution as part of the goals of the Stanford PSAAP Center, the MCM is computationally expensive compared to other methods when a low level of statistical variance is required. Typically, a sensitivity analysis requires a large number of sample solutions to characterize the system response to the relevant inputs. Instead, the MCM using LBL data is used in this thesis to quantify the uncertainty in the DOM used by Crow. To reduce computa-

tional costs, only the radiation of water vapor, a species that contributes the majority of radiative heat flux, is considered in the MCM simulations.

1.4.2 Quantification of Epistemic Error of a MCM Using LBL Tables

The Monte Carlo and LBL methods are theoretically capable of simulating radiative thermal transport with little or no uncertainty; however, in practice the variables used as inputs will carry some uncertainty that can influence the solution. The LBL method utilizes a large database containing parameters used in calculating the shape of a spectral line, and these parameters have some error. As the DOM is used with an approximate method for spectral modeling, it cannot directly sample the uncertainty of line parameters. Therefore, in order to quantify the uncertainty of the radiative solution due to the input spectral line parameters, this work conducts a sensitivity analysis of the radiative thermal transport to the uncertainties of the input line parameters.

Directly sampling the parameters of all relevant spectral lines is impractical for even simple problems. Therefore, this thesis characterizes the sensitivity of a one dimensional radiative thermal transport solution to parameter variation using small groups of spectral lines. Using the sensitivity analysis, this work creates a model of the uncertainty due to uncertainty of spectral line parameters. This model is used in the three dimensional simulations of HIFiRE-2 to quantify the epistemic uncertainty of the radiation solutions to the spectral line parameters.

1.4.3 Reduction of Teleportation Error in Monte Carlo Simulations

Currently, teleportation error is eliminated or reduced by refining the spatial grid even when using the source tilting correction method. This increases computational costs, as additional particles are needed to populate the additional cells. Additionally, the effect of teleportation error on the solution is not always obvious and can be un-

noticed in numerical solutions. This thesis presents a teleportation correction method that reduces the epistemic error in time dependent MCMs by emitting particles from sampled absorption locations. The accuracy of the teleportation correction method with decreasing spatial resolution is documented, and compared to the source tilting method. A variety of test problems are used to verify the effectiveness of the teleportation correction method in likely usage scenarios. Finally, this thesis quantifies the computational costs of the teleportation correction method relative to the source tilting method.

1.5   Thesis Organization

The remainder of this thesis is arranged as follows:

Chapter II describes the equations, terms, and assumptions of the radiative thermal transport equations used in this thesis. Two models commonly used to solve the radiative thermal transport equations, the MCM and DOM, are introduced. The physics of thermal radiation are discussed, and the equations that describe the spectral line structure of thermal radiation are explained. Finally, three models for calculating the spectral properties necessary to simulate radiative thermal transport are presented.

In Chapter III, the Implicit Monte Carlo (IMC) equations are derived with discussion of the physical interpretation of the equations. Approximations made during the derivation of these equations are highlighted. The implementation of the teleportation correction method is described. Creation of spectral property tables using the LBL method is described. The coupling of the computer codes utilizing these methods is presented.

In Chapter IV, background of the HIFiRE program is discussed with a focus on the HIFiRE-2 flight test program. The flow features and geometry of the HIFiRE-2 scramjet are described. Computational solutions of the thermodynamic properties

relevant to radiative thermal transport are shown.

In Chapter V, solutions of the radiative thermal transport for water vapor determined by the implicit Monte Carlo method using spectral properties found with the LBL method are presented. The features of the radiation solution are discussed and the statistical variation in the solution is quantified. These solutions are compared to solutions found using the DOM, and the error of the discrete ordinates solutions is quantified. Finally, a one dimensional problem is modeled to find the uncertainty in the implicit Monte Carlo simulations due to uncertainties in the spectral modeling inputs.

In Chapter VI, simulations of three problems exhibiting teleportation error are created using the source tilting method and the teleportation correction method presented in this thesis. These simulations show how teleportation error can influence the solutions to these problems, and the performance of the teleportation correction method in reducing these types of errors. Computational costs of the teleportation method relative to the source tilting method are presented.

Finally, Chapter VII reviews the major results presented in this thesis. Potential directions for future work based on the findings in this thesis are also discussed.

CHAPTER II

Radiative Thermal Transport Theory

The term *thermal radiation* is used here to describe the photons that are emitted due to the temperature of a medium. Thermal radiation is continuously generated randomly by all materials with a rate, directionality, and frequency that is determined by the emitting material properties and temperature. Relative to conductive and convective heat transfer, thermal radiation becomes more important, if not dominant, with increasing temperature. Modeling the transport of thermal radiation requires knowledge of the physical process by which photons are emitted and propagate through a medium. This chapter introduces the equations of thermal radiative transport, some transport models, and radiative property models.

2.1 Radiative Thermal Transport Theory

Where an electromagnetic wave falls within the electromagnetic spectrum can be described by its frequency, υ; wavenumber, η; wavelength, λ; or angular frequency, ω. Wavenumbers are used in this thesis and are related to the other quantities by

$$\eta = \frac{\upsilon}{c} = \frac{1}{\lambda} = \frac{\omega}{2\pi c}, \tag{2.1}$$

where c is the speed of light which is the speed at which radiation propagates through a medium and is related to the index of refraction, n, of the medium and the speed of light through a vacuum, c_o, by

$$c = \frac{c_o}{n},$$ (2.2a)

$$c_o = 2.998 \times 10^8 m/s \qquad\qquad \text{speed of light in vacuum.} \qquad (2.2b)$$

This thesis is focused on the propagation of thermal radiation through a gas that has a refractive index of near unity, and is assumed to be equal to one. As such, the speed of light is taken to be equal to its value in a vacuum throughout the medium and there are no refraction effects. The total emitted radiative flux per unit area from a surface for all wavenumbers is known as the total emissive power, E, and spectral emissive power, E_η, for a specific wavenumber over an interval. The total emissive power is simply the integral of spectral emissive power over all wavenumbers. The spectral emissive power of a surface that absorbs all incident radiation, called a blackbody, that is surrounded by a transparent medium is given by Planck's law [52].

$$E_{b\eta}(\mathbf{x}, T) = \frac{2\pi h c_o^2 \eta^3}{n^2 \left(e^{h c_o \eta / n k T} - 1\right)},$$ (2.3a)

$$h = 6.626 \times 10^{-34} J\,s \qquad\qquad \text{Planck's constant,} \qquad (2.3b)$$

$$k = 1.3806 \times 10^{-23} J/K \qquad\qquad \text{Boltzmann's constant.} \qquad (2.3c)$$

While emissive power can describe the radiative heat flux from a surface, it does not describe the directionality of the flux. To consider the radiation field, it is necessary to define the total radiative intensity, I, and spectral radiative intensity, I_η, as the radiative heat flux per unit area per unit solid angle. Emissive power from a surface is found from radiative intensity by integrating over all directions away from

the surface such that

$$E(\mathbf{x}) = \int_0^{2\pi} \int_0^{\pi/2} I(\mathbf{x}, \theta, \psi) cos(\theta) \, sin(\theta) d\theta d\psi, \qquad (2.4)$$

$$I_b(\mathbf{x}) = E_b(\mathbf{x})/\pi, \qquad (2.5)$$

where θ is the polar angle from the point of emission, ψ is the azimuth, and $I_{b\eta}$ is the blackbody spectral intensity. The same expression applies for relating the spectral radiative intensity to the spectral emissive power. The solid angle, Ω, is the area of a projection onto a unit sphere of the area described by the differential polar and azimuthal angles divided by the distance squared. Equation 2.6 shows the relationship between the solid angle, polar, and azimuthal angles, followed by recasting equation 2.4 to use the solid angle.

$$d\mathbf{\Omega} = sin \, \theta \, d\theta \, d\psi, \qquad (2.6)$$

$$E(\mathbf{x}) = \int_{2\pi} I((\mathbf{x}, \hat{\mathbf{s}}) \hat{\mathbf{n}} \cdot \hat{\mathbf{s}} d\Omega, \qquad (2.7)$$

where $\hat{\mathbf{s}}$ is a vector from the surface to the area described by the solid angle, and $\hat{\mathbf{n}}$ is a vector normal from the surface. To describe the interaction of radiative energy through a medium, it is observed that the absorption is directly proportional to the distance traveled through the medium and the incoming energy[2]

$$(dI_\eta)_{absorbed} = -\kappa_\eta I_\eta dx, \qquad (2.8)$$

$$\kappa_{p\eta,i} = \kappa_\eta p_i, \qquad (2.9)$$

where κ_η is the absorption coefficient of the medium, $\kappa_{p\eta,i}$ is the pressure based absorption coefficient, and p_i is the partial pressure of species i. A region that allows most, if not all, incoming radiation to pass through it has a small absorption coefficient

and is denoted as being optically thin, or transparent. Conversely, a region that absorbs most, if not all, incoming radiation has a large absorption coefficient and is denoted as being optically thick, or opaque.

There are several assumptions to the underlying physics that are made in the radiative thermal transport equations, as well as assumptions that are based on the problem of interest. First, it is convenient to make an assumption of local thermodynamic equilibrium, where the properties of the matter are described by thermodynamics and are considered to be constant through a time step. The transport equations assume a classical description of photons as particles and ignore wave behaviors, which means that diffraction is neglected. Polarization can be taken into consideration using additional equations, but as thermally emitted radiation is randomly polarized, it is neglected here[53]. Additionally, for the temperatures, pressures, and medium considered, we can neglect physical scattering effects and assume emissions and absorption coefficients are isotropic. There is also an assumption that photon interactions take place instantaneously and the time for the resulting stimulated emission depends on the time step as opposed to the physical process. Finally, as the rate of movement of the medium is much smaller than the speed of light, the medium is assumed to be stationary. Using these assumptions, equations 2.10 and 2.11 are the radiative thermal transport equations used for this thesis, as derived by Modest[43], Pomraning[53], and numerous other sources.

$$\frac{1}{c}\frac{\partial I_\eta}{\partial t}\left(\mathbf{x},\hat{\mathbf{s}},t\right) + \hat{\mathbf{s}}\cdot\frac{\partial I_\eta}{\partial x}\left(\mathbf{x},\hat{\mathbf{s}},t\right) = \tag{2.10}$$

$$\kappa_\eta\left(\mathbf{x},T,p_i,p\right)\left(2\pi I_{b\eta}\left(T\right) - I_\eta\left(\mathbf{x},\hat{\mathbf{s}},t\right)\right) + S\left(\mathbf{x},\hat{\mathbf{s}},t\right),$$

$$q_\eta\left(\mathbf{x},t\right) = c_v\left(\mathbf{x},T\right)\frac{\partial T}{\partial t}\left(\mathbf{x},t\right) = \tag{2.11}$$

$$\int\limits_0^\infty \int\limits_{4\pi} \kappa_\eta\left(\mathbf{x},T,p_i,p\right)\left(I_\eta\left(\mathbf{x},\hat{\mathbf{s}},t\right) - I_{b\eta}\left(\eta,T\right)\right) d\Omega d\eta.$$

Above, c_v is the coefficient of specific heat at constant volume, T is the local temperature, and S is a source term. The following physical interpretation of these equations is used in the Monte Carlo Method (MCM) in section 3.1. The first term on the left side of equation 2.10 is the time rate of change of spectral radiative intensity. The second term on the left side of this equation is the loss of energy due to photons moving out of a differential spatial element. The first group on the right side of this equation represents the rate at which energy is emitted into the radiation field minus the energy absorbed into the medium. The last term on the right side of equation 2.10 represents a radiative source that can be external or internal, and defined by the problem. The change in energy of the radiation field described by equation 2.10 is coupled with equation 2.11 that describes the heat flux into the medium from the radiation field. The second equality in equation 2.11 shows the temperature dependence of the medium on the heat flux. The right side of equation 2.11 represents the rate at which energy is absorbed by the medium from the radiation field for the first term in the integral. The second term in the integral is the rate at which radiative energy is emitted by the medium into the radiation field.

Practically, continuous data for the thermodynamic properties of the medium is not known. Even with continuous data, the non-linear dependence on temperature of the transport equations, and the absorption coefficient, makes analytical solutions of the unsimplified equations using continuous data impossible. To solve equations 2.10 and 2.11, a spatial discretization of the parameters that describe the medium is used to divide the problem up into a number of spatial regions called cells. The cell geometries are defined by a number of node points that make up a spatial grid. Thermodynamic properties are assumed to be constant within a cell.

2.2 Radiative Thermal Transport Models

Analytic solutions to the radiative thermal transport equations are not possible except for specific or simplistic systems. Generating a solution to practical problems requires the use of approximations for the transport equations. Since the motivation of this thesis is to produce solutions that have minimal epistemic error, it is necessary to limit consideration to models that can easily be refined for an arbitrary accuracy on an arbitrary spatial grid. Two widely used methods that meet these requirements are the Monte Carlo and discrete ordinates methods.

2.2.1 Monte Carlo Method

Monte Carlo Methods (MCMs) do not describe a specific scheme, but rather a method that solves an equation, or set of equations, using statistical sampling. For radiative thermal transport, MCMs are typically constructed such that they sample a large number of particles that are propagated through the problem of interest in a manner approximating the physics of a photon. Parameters of interest are solved for by a summation of the particle influence on these parameters over time and/or space depending on the discretization of the problem. Since solutions are the result of the summation of many individual particle contributions, the solution has a statistical variance that can be described by the central limit theorem. This variance decreases at a rate inversely proportional to the square root of the number of particles. This means that an exact solution, limited to any approximations made, can be found using an infinite number of particles. Of course, computational resources are finite and so a solution found by a MCM has some level of uncertainty. The convergence rate of MCMs can be time consuming if a low level of uncertainty is required as every reduction in variance by a factor of 10 requires an increase in the number of particles by a factor on the order of 100[43].

The calculation of a particle path starts by emitting the particle through thermal

emission from the medium or through a boundary source. The particle position and direction are randomly determined for thermal emission, while the energy is set to a predetermined value that depends on the simulation. The wavenumber of the particle is sampled from the normalized cumulative absorption coefficient that is found based on the spectral model. Particle propagation involves sampling the probability of particle interactions with the medium as well as the boundaries. Particle paths can be terminated when they undergo an absorption event, but typically do not follow this interpretation in favor of extending the particle path by various methods in order to gain more information from each particle thus reducing the statistical variance in the solution.

In this thesis, there are several ways that particles in the radiative thermal transport MCM do not follow the exact physics of photons. A rigorous treatment of photon behavior is computationally prohibitive and the approximations made should have little impact on the solution. Particles in this thesis represent a large number of photons as most practical problems contain many more photons than are necessary to reach a small variance, or are practical in terms of computational costs. Consequently, in order to maintain the sampled distribution of energy across wavenumber space, it is necessary that a particle's wavenumber not change due to any changes in particle energy not due to interactions with the medium. Uniformly sampling emission locations within a spatial cell rather than at the absorption location can cause radiative fluxes that are too high. This error is discussed further in section 2.2.1.1. There are also several other assumptions made in the transport equations as described in section 2.1.

Since particles are considered independent of each other and the medium is unaffected by the radiation field within a time step, it is relatively easy to modify a serial MCM code to work in parallel. By allocating a number of particles to each processor, the only inter-processor communication that is required comes at the end of a time

step when the energy contributions to cells are added and can be used to determine the material properties for the next time step. Given the minimal inter-processor communication, the parallel scaling, that is the reduction in total time to solution as a function of the number of processors used, of propagating particles can be close to ideal. The exception is when it is necessary to decompose the spatial domain. In that case, it is necessary for additional communication to send particle information across domains as particles travel from one domain to another.

2.2.1.1 Teleportation Error

In a typical MCM, the location of emission for thermal particle emissions, which are the result of energy deposited into the medium in a previous time step, are sampled uniformly throughout a cell. The location of energy absorption is only considered in emission insofar as the cell in which the absorption occurred. In an opaque cell, energy can be deposited on one side of a cell and emitted at locations sampled on the other side resulting in radiation being transported faster than it should. This results in a type of spatial discretization error not present in deterministic methods and is referred to as teleportation error. Teleportation error can be mitigated by using smaller spatial cells that necessarily cause emission points to be closer to absorption points. This has the disadvantage of increasing the computational cost of the simulation without eliminating the error. Additionally, teleportation error increases with increasing temporal resolution on a fixed spatial grid. This is due to an increase in the number of spatial averages of energy over a given time interval. There is an additional mechanism that increases teleportation error with increasing temporal resolution that is a consequence of the implicit Monte Carlo method and is discussed in section 3.1.1.

2.2.2 Discrete Ordinates Method

The Discrete Ordinates Method (DOM) is a deterministic method that simplifies the radiative thermal transport equations by discretizing the direction of radiative intensity into N directions. The resulting system of equations is solved over the full unit sphere. Weights are assigned for each direction based on the numerical quadrature scheme used, and the solution is the weighted sum of the radiative intensity solution. By increasing the number of discretized directions, the DOM converges towards the exact solution. As with the MCM, the availability of computational resources forces a compromise between computation time and accuracy of solution.

The selection of numerical quadrature for discretizing the angular space is arbitrary, although this selection can significantly affect accuracy and computational efficiency. Some of the first work with the DOM for radiative thermal transport used only two directions[60, 59] with the use of more directions being introduced by Chandrasekhar[8]. The numerical quadrature could be chosen to be highly directional to represent a problem with a high degree of anisotropy, but a more general scheme is of interest here. Typically, a quadrature is invariant with rotations of ninety degrees and satisfies the first moment equation in the principal directions. The DOM solutions in section 5.2.1 use a S_8 quadrature, which evenly distributes points along eight latitudes of the unit sphere. There are numerous other quadrature methods in use with a summary of several methods and their accuracy made by Koch[32].

2.3 Radiative Properties of Gases

The absorption and emission of radiation from a gas is the result of interactions between photons and matter as described by quantum mechanics. Specifically, radiation is the transition of molecules from one molecular state to another. The change in energy resulting from this transition is carried by a photon with wavenumber $\eta = \frac{\triangle E}{h c}$.

There are three processes that result in radiative emission: bound-bound transitions where transitions occur between bound molecular states, bound-free transitions where transitions occur between a bound electron state to or from a dissociated state, and free-free transitions where transitions occur between electron or ion states. The energy for a bound-free transition is either the input energy that caused a dissociation, or the kinetic energy of the atomic parts that recombine. Since these energies are not quantized, the resulting absorption coefficient for bound-free transitions is continuous over wavenumber. Similarly, the absorption coefficient for free-free transitions is also continuous as free-free transitions result in changes in electron kinetic energy that are not quantized. In bound-bound transitions, radiation absorbed or released from a molecule is the result of a change in electronic, vibrational, and/or rotational states that have discrete levels of energy. Since radiative interactions in bound-bound transitions can only occur with those changes in energy, the resulting absorption coefficient, in the absence of broadening effects, is comprised of a collection of lines at wavenumbers corresponding to the wavenumber of a photon carrying the energy of an allowed transition. As the problem of interest is not at a high enough temperature to have significant ionization, only bound-bound transitions are considered in this thesis.

There are a number of parameters, used below, that characterize the absorption coefficient resulting from a transition. There are numerous sources for these parameters, both experimental and theoretical, in literature. This thesis makes use of the HITEMP 2010 database, which is a large collection of absorption line transition parameters for several radiative species from a variety of sources, presented in a consistent format[56]. Penner derives the equation used to calculate the spectral line intensity tabulated in the HITEMP 2010 database[57, 51]. The line intensity, $S(T_{ref})$, listed in the HITEMP 2010 database requires a correction for temperature

by

$$S(T) = S(T_{ref}) \frac{Q\left(T_{ref}\right)}{Q\left(T\right)} \frac{e^{\frac{-E_\eta\, h\, c}{k\, T}}}{e^{\frac{-E_\eta\, h\, c}{k\, T_{ref}}}} \frac{1 - e^{\frac{-\eta_o\, h\, c}{k\, T}}}{1 - e^{\frac{-\eta_o\, h\, c}{k\, T_{ref}}}} \quad cm^2/molecules, \qquad (2.12)$$

above $T_{ref} = 296K$. Here, Q is the internal partition function, E_η is the energy of the lower state for the transition, and η_o is the spectral line transition wavenumber. The units of line intensity include the number density of absorbing molecules in inverse cubic centimeters.

The collisional and natural line broadening mechanisms are considered in this thesis. The classical treatment of collisional broadening considers the abrupt change in phase of an otherwise continuous electromagnetic wave as a result of collisions between molecules. Natural line broadening results from the uncertainty of a photon's location and energy as described by the Heisenberg uncertainty principle. The lifetime of an excited state is finite so the energy of that transition cannot be known exactly, and results in the broadening of absorption lines. What is often called the Lorentz profile describes the form of both collisionally and naturally broadened lines that are typically combined into one profile [65].

$$f\left(\eta, T, p, p_i\right) = \frac{1}{\pi} \frac{\gamma\left(p, T\right)}{\gamma\left(p, T\right)^2 + \left[\eta - \left(\eta_o + \delta\left(p_{ref}\right)\, p\right)\right]^2}, \qquad (2.13)$$

where the Lorentz profile, f, varies with wavenumber, η; the transition frequency, η_o; the air broadened pressure shift taken at 1 atmosphere, $\delta\left(p_{ref}\right)$; pressure, p; and the line half width at half maximum (HWHM), γ, that is defined by

$$\gamma\left(T, p, p_i\right) = \left(\frac{T_{ref}}{T}\right)^n \left(\gamma_{air}\left(p_{ref}, T_{ref}\right)\left(p - p_i\right) + \gamma_{self}\left(p_{ref}, T_{ref}\right) p_i\right), \qquad (2.14)$$

In the above, p_i is the partial pressure of the species for which the spectrum is being calculated, γ_{air} is the air broadened HWHM, γ_{self} is the self broadened HWHM, and

n is the coefficient of temperature dependence for the line HWHM.

Doppler broadening is another common line broadening mechanism that is the result of velocity differences between the movement of the emitting molecule and the observer. The resulting profile from collisional, natural, and Doppler broadening is a Voigt profile, but for transport applications at pressures over one atmosphere and temperatures under 2500K, the Lorentz profile is sufficient[63]. Furthermore, the temperature where the Lorentz profile is accurate, increases with increasing pressure resulting in the Lorentz profile being sufficient throughout the domain described in Chapter 4.

Using equations 2.12 and 2.13, the absorption coefficient can be found by

$$\kappa_\eta \left(\eta, T, p, p_i\right) = n_i \, S\left(T\right) \, f\left(\eta, T, p, p_i\right), \quad cm^{-1} \tag{2.15}$$

where n_i is the number density of absorbing molecules per cubic centimeter. When more than one radiating species is considered, the absorption coefficient of the mixture at a given wavenumber is simply the sum of the absorption coefficients for each radiating species

$$\kappa_\eta = \sum_i n_i \, S_i \, f_i \, = \sum_i \kappa_{\eta,i}. \tag{2.16}$$

In the above, the subscript i is used to indicate species specific values.

To calculate the total radiative emission from a volume element, it is useful to define the Planck mean absorption coefficient,

$$\kappa_p = \frac{\int_0^\infty I_{b\eta} \, \kappa_\eta \, d\eta}{\int_0^\infty I_{b\eta} \, d\eta} \, = \frac{\pi}{\sigma \, T^4} \int\limits_0^\infty I_{b\eta} \, \kappa_\eta \, d\eta. \tag{2.17}$$

Similar to the absorption coefficient, the Planck mean absorption coefficient is additive when considering multiple radiating species. It is also useful to define the pressure

based absorption and Planck mean absorption coefficients which use the following definitions

$$\kappa_{\eta,p} = \frac{\kappa_\eta}{p} = \sum_i x_i \, \kappa_{\eta,pi}, \ \kappa_{i\eta,pi} = \frac{\kappa_\eta}{p_i}, \tag{2.18}$$

$$\kappa_{p,p} = \frac{\kappa_p}{p} = \sum_i x_i \, \kappa_{p,pi}, \ x_i \, \kappa_{p,pi} = \frac{\kappa_{p,i}}{p_i}, \tag{2.19}$$

where x_i is the species mole fraction. Finally, for a MCM, it is necessary to sample the normalized cumulative absorption coefficient, which is the wavenumber distribution sampled for a thermally emitted particle. The relations for the distribution for a single species and a gas mixture are shown here,

$$P_{\eta,i} = \frac{\int_0^\eta \kappa_{\eta,pi} \, I_{b\eta} \, d\eta}{\int_0^\infty \kappa_{\eta,pi} \, I_{b\eta} \, d\eta} = \frac{\pi}{\sigma \, T^4 \, \kappa_{p,pi}} \int_0^\eta \kappa_{\eta,pi} \, I_{b\eta} \, d\eta, \tag{2.20}$$

$$P_\eta = \frac{\pi}{\sigma \, T^4 \, \sum_i x_i \, \kappa_{p,pi}} \sum_i \int_0^\eta \kappa_{\eta,pi} \, I_{b\eta} \, d\eta = \frac{\sum_i x_i \, \kappa_{p,pi} \, P_{\eta,i}}{\sum_i x_i \, \kappa_{p,pi}}. \tag{2.21}$$

The complexity of the absorption coefficient makes solving the distribution for wavenumber impossible. For such sampling, the distribution requires a trial and error method to find the value of the distribution for each species for a trial wavenumber. The trial wavenumber is adjusted by a goal seeking method until a preset level of convergence is achieved.

2.3.1 Line by Line Spectral Table

The line by line (LBL) model of the absorption coefficient calculates the spectrum directly from the equations in section 2.3 which makes it the most accurate spectral model in use, but it is also the most computationally expensive. The direct calculation of the absorption coefficient at a given wavenumber involves a summation of the contribution of every relevant absorption line based on the line's profile

at the given wavenumber. The HITEMP database lists the parameters used in the calculation of line profiles for over 100 million transitions for water vapor[56]. Even after elimination of absorption lines that contribute less than 0.1% to the integrated absorption coefficient across narrow bands, as well as small bands themselves, there are still over 20 million transitions to take into account for water vapor. While this calculation is simple to parallelize, the calculation of the absorption coefficient at a given wavenumber, local thermodynamic condition, and composition is non-trivial. Additionally, the normalized cumulative absorption coefficient must be calculated in order to sample the wavenumber of thermally emitted particles. The calculation of absorption coefficient at the wavenumber of every generated particle for each of the flow regions it propagates through quickly makes the LBL method impractical for practical problems.

A solution to the computational expense of the LBL method, as described by Wang [68], is to discretize the spectrum across wavenumber and generate a spectrum for a number of thermodynamic conditions that represent the problems of interest. The result is a large table of absorption coefficients at a number of wavenumbers, temperatures, pressures, and mole fractions, that can be interpolated for intermediate values of these parameters. Another table for the normalized cumulative absorption coefficient is necessary to avoid its recalculation for each cell at each time step. For this thesis, tables are constructed for every cell in one dimensional problems to find a necessary spectral discretization and to test interpolation accuracy of discretization across temperature, pressure, and mole fraction of more general tables. The accuracy of the emissive power transported to a wall is used as the benchmark for these tests. Once a sufficient discretization is found, the table can be constructed once to find the absorption coefficient or sample the wavenumber for any cell in the problem through interpolation.

Given the large size of the look-up tables, it is desirable to minimize their memory

requirements. It is shown in section 5.3 that the uncertainties in the HITEMP 2010 parameters are significant and as such, a significant level of error in the look-up tables may be tolerable. Since the interpolation error is likely to be higher than the precision of a single precision data type, the use of double precision is unnecessary. The absorption coefficient of water vapor is negligible across several areas of the spectrum and could be eliminated within bands. However, the efficiency of this deletion is dependent on the wavenumber range removed, as a discontinuous table requires the additional storage of wavenumbers bounding those discontinuities.

2.3.2 Narrow Band Model

Given the additive nature of the absorption coefficient, it is tempting to simply use a summation across a relatively small set of wavenumber bands. However, when integrating over a wavenumber band, the absorption line overlap must be considered as the absorption is less for strongly overlapped lines than the sum of the isolated lines[65]. While the spacing of absorption lines can be modeled in many ways, all methods are bounded by two extremes. The Elasser model considers absorption lines to be spaced at equal intervals which minimizes overlap and maximizes absorption[17]. At the other extreme is the statistical model that has absorption lines spaced randomly[21, 40]. The maximum difference in calculated absorption coefficient between these models is 20%[65].

When a band model is applied to a homogeneous medium, it is not necessary to consider the correlation of absorption coefficients between cells. While the real absorption coefficient is highly irregular, it can be considered to be perfectly correlated, since all cells have the same spectral properties. However, for an inhomogeneous case, the absorption coefficient at a wavenumber can be at a line center in one cell and at the line wings in a different cell. Thus, the transmitted spectral radiative intensity of radiation emitted from one cell can be over or under estimated as that radiation trav-

els through another cell when using the absorption coefficient generated by a band model. There are a number of references that discuss approximations made for band models to correct for this correlation[63, 65, 43, 36].

If a band model is applied to the MCM, the random number relations used in sampling the path length should be modified. For radiation emitted that is sampled from a source like a blackbody with a smooth absorption coefficient, much of the radiation falls in the wings of absorption line profiles for the medium. As a result, there should be more radiation transmitted through a cell than is indicated by the absorption coefficient from a band model. Similarly, there is a higher probability that radiation that is emitted from the medium is at a wavenumber close to the center of an absorption line profile than at the line wings. This should result in less radiative energy transported through a cell than is found using only the absorption coefficient from the band model. Corrections to the random number relations for path length in a MCM are discussed by Modest[45].

2.3.3 Correlated k Model

For a small wavenumber range, the Planck function can be considered constant, but the absorption coefficient still has a highly irregular character. Over this range, the transport of radiative intensity only depends on the absorption coefficient for a homogeneous medium. The k-distribution model recognizes that a particular value of absorption coefficient, defined in this model as k, occurs many times across this wavenumber range and that these absorption coefficient values all produce the same radiative intensity field. Thomas[64], Modest[43], and others describe a new function that is the weighted sum of the number of times across the wavenumber range the value of k occurs.

$$f\left(k\right) = \frac{1}{\triangle \eta} \sum_l \left| \frac{d\eta}{dk} \right|_l.$$
(2.22)

39

Practically, it is necessary to calculate $f(k)$ over a finite number of k ranges and find values of k that occur over these ranges such that

$$f(k) = \frac{1}{\triangle \eta} \sum_l \left| \frac{\delta \eta}{\delta k} \right|_l W_l(k).$$
(2.23)

where $W_l(k)$ is a window function,

$$W_l(k) = \begin{cases} 1, k_{l,min} \leq k \leq k_{l,max} \\ 0, otherwise \end{cases}.$$
(2.24)

While $f(k)$ is still an erratic function, the cumulative integral of $f(k)$, $g(k)$, is a relatively smooth monotonic function. The inverse of $g(k)$, $k(g)$, can then be taken as the absorption coefficient reordered to increase in value as a function of a non-dimensional wavenumber g. Since the $k(g)$ function is relatively well behaved, far fewer quadrature points are needed to numerically model this function than are required to resolve fluctuations in the absorption coefficient.

If a sufficient quadrature scheme is used to represent the $k(g)$ function, the k-distribution model can approach the accuracy of the LBL model for a homogeneous medium. However, the generation of function $f(k)$ removes information of spectral correlations which are important for inhomogeneous mediums. There are a number of methods for addressing the spectral correlations for the k-distribution model. The correlated-k model assumes that all the absorption coefficients at a location in the k-distribution exhibit the same variations with changes in cell conditions. This works well for changes in pressure as all absorption line profiles are affected similarly. However, this assumption breaks down at high temperatures where previously negligible lines can be dominant and differences in the coefficient of temperature dependence of the HWHM becomes more important. Further discussion of k-distributions and correlations corrections can be found in a number of references [69, 63, 46].

2.4   Summary

This chapter describes the equations, terms, and assumptions of the radiative thermal transport equations used in this thesis. Two models commonly used to solve the transport equations, the MCM and DOM, are introduced. The physics of thermal radiation are discussed, and the equations that describe the spectral line structure of thermal radiation are explained. Finally, three models for calculating the spectral properties necessary to simulate radiative thermal transport are presented.

CHAPTER III

Radiative Thermal Transport Simulation Methods

The method used to solve the radiative thermal transport equations, in this thesis, are detailed in this chapter. Since the goal of this thesis is to calculate the radiation field with minimal epistemic uncertainty, a Monte Carlo Method (MCM) is used to simulate the radiative thermal transport. Solving the radiative thermal transport equations typically starts with a linearization of the equations over time. A well known method of linearizing these equations applied to a MCM is the Implicit Monte Carlo (IMC) method, proposed by Fleck and Cummings[29], which is used for this thesis. Spectral properties of the medium required for particle propagation are calculated at a number of thermodynamic conditions using a Line by Line (LBL) method.

3.1 Implicit Monte Carlo Method

The IMC method was developed to reduce the computational costs of simulating radiative thermal transport in opaque regions within a modeled domain, as well as the numerical stability of MCM simulations. The IMC method reduces computational costs by adding artificial scattering to the simulation that becomes dominant over absorption in opaque regions. This scattering has the effect of increasing particle path lengths, which would otherwise travel a short distance before being absorbed. These longer path lengths can provide more information about the solution per particle than

a conventional treatment. IMC simulations are also unconditionally stable if the time centering parameter, α, defined in section 3.1.1, is set at unity such that the stability condition is always satisfied[29],

$$(1 - \alpha) \beta c \triangle t \kappa_p \leq 1. \tag{3.1}$$

While the unconditional stability of IMC allows for the use of relatively large time steps, there are limits where an IMC solution can show unphysical behavior[71, 34].

Figure 3.1 shows a schematic of the flow of information through the IMC simulation. Before the IMC simulation starts, the range of temperatures, pressures, and mole fractions in the problem of interest are used to define the bounds of the spectral property look-up tables, and the radiative species considered are picked. The LBL method is used to construct tables of absorption coefficient and the normalized cumulative absorption coefficient distribution for each species using an appropriate discretization of each input range. These tables are used by the IMC simulation to describe the radiative properties of the medium, as they apply to the transport of radiation. The IMC simulation requires geometry information of the spatial grid, as well as the local value of temperature, pressure, and mole fraction of each cell. Spectral properties of a cell are interpolated from the look-up tables using the thermodynamic properties of the cell. The character of the radiative thermal emission of particles is dependent on the spectral and thermodynamic properties of the cell. Transport of these particles carries information of the radiative thermal transport into cells within the system domain. The cumulative energy transported by these particles into each cell describes the radiative thermal transport, which can be used to update the thermodynamic properties of the medium for use in subsequent time steps.
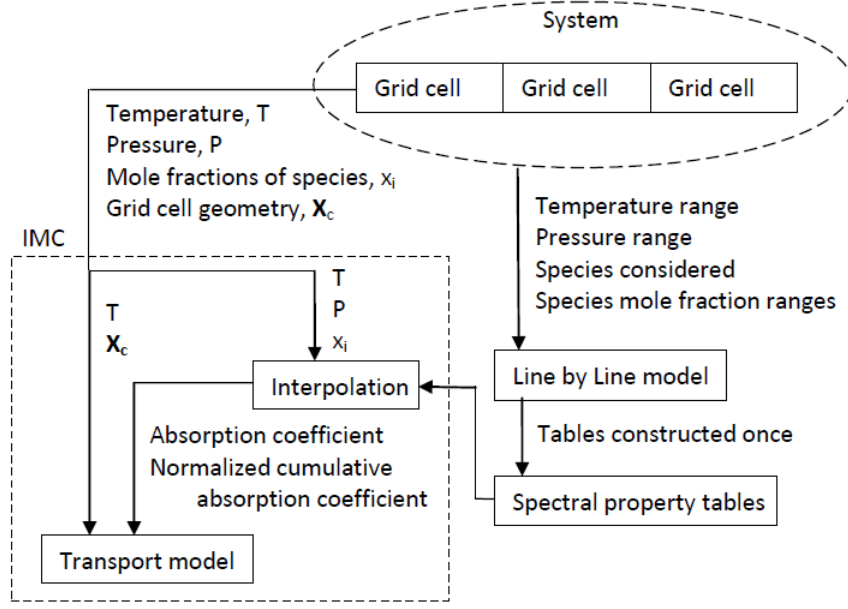
Figure 3.1: Schematic showing flow of information through an IMC simulation

3.1.1 Implicit Monte Carlo Discretization

The material energy density, u_m; equilibrium radiation energy density, u_r; and their relationship, β; are defined as,

$$\frac{\partial u_m}{\partial T}(\mathbf{x}, t) = c_v(\mathbf{x}, t), \tag{3.2}$$

$$u_r(\mathbf{x}, t) = a\, T^4(\mathbf{x}, t), \tag{3.3}$$

$$a = 7.566\, J\, m^{-3}\, K^{-4,} \qquad \text{Radiation constant} \tag{3.4}$$

$$\beta(\mathbf{x}, t) = \frac{\partial u_r}{\partial u_m} = \frac{4\, a\, T^3}{c_v(T)}. \tag{3.5}$$

Now the normalized Planck function, b, and Planck mean absorption coefficient, κ_p, are defined as

$$b_\eta(T) = \frac{E_{b\eta}(T)}{\int_0^\infty E_{b\eta}(T)\, d\eta}, \tag{3.6}$$

$$\kappa_p(\mathbf{x}, T, p_i, p) = \frac{\int_0^\infty \kappa_\eta(\mathbf{x}, T, p_i, p)\, E_{b\eta}(T)\, d\eta}{\int_0^\infty E_{b\eta}(T)\, d\eta}. \tag{3.7}$$

Using the above equations, the radiative transport equations can now be rewritten as

$$\frac{1}{c}\frac{\partial I_\eta}{\partial t}(\mathbf{x},\hat{\mathbf{s}},t) + \hat{\mathbf{s}}\cdot\frac{\partial I_\eta}{\partial x}(\mathbf{x},\hat{\mathbf{s}},t) =$$

$$\kappa_\eta(\mathbf{x},T,p_i,p)\left(\tfrac{1}{2}b_\eta(T)\,c\,u_r - I_\eta(\mathbf{x},\hat{\mathbf{s}},t)\right) + S(\mathbf{x},\hat{\mathbf{s}},t), \tag{3.8}$$

$$\frac{1}{\beta}\frac{\partial u_r}{\partial t} = \int_0^\infty \int_{4\pi} \kappa_\eta(\mathbf{x},T,p_i,p)\,I_\eta(\mathbf{x},\hat{\mathbf{s}},t)\,d\Omega d\eta - \kappa_p(\mathbf{x},T,p_i,p)\,c\,u_r, \tag{3.9}$$

$$\frac{\partial u_m}{\partial t} = \int_0^\infty \int_{4\pi} \kappa_\eta(\mathbf{x},T,p_i,p)\,I_\eta(\mathbf{x},\hat{\mathbf{s}},t)\,d\Omega d\eta - \kappa_p(\mathbf{x},T,p_i,p)\,c\,u_r. \tag{3.10}$$

Integration of equation 3.9 over time from t^n to t^{n+1} yields

$$u_r^{n+1} - u_r^n = \int_{t^n}^{t^n+1} \beta \int_0^\infty \int_{4\pi} \kappa_\eta I_\eta\,d\Omega\,d\eta\,dt - c\int_{t^n}^{t^n+1} \beta\,\kappa_p\,u_r\,dt, \tag{3.11}$$

$$\frac{u_r^{n+1} - u_r^n}{\Delta t\,\overline{\beta}} = \int_0^\infty \int_{4\pi} \overline{\kappa}_\eta I_\eta^\lambda\,d\Omega\,d\eta - c\overline{\kappa}_p\left[\alpha\,u_r^{n+1} + (1-\alpha)\,u_r^n\right], \tag{3.12}$$

where t^n is the time at the beginning of time step n, and t^{n+1} the time at the end of that time step. The values λ, γ, and α are time centering parameters with α satisfying $1/2 \leq \alpha \leq 1$. Values with an over-bar($^-$) indicate time averaged values, but these values are approximated to be constant through the entire time step. These values could be predicted by an appropriate forward extrapolation, or by iterating over the time step using calculated average values until they converge. Defining the Fleck factor, f, and solving equation 3.12 for u_r^{n+1} shows,

$$f = \frac{1}{1 + \alpha\,\beta\,c\,\Delta t\,\overline{\kappa}_p}, \tag{3.13}$$

$$u_r^{n+1} = \left[\frac{1 - (1-\alpha)\,\beta\,c\,\Delta t\,\overline{\kappa}_p}{1 + \alpha\,\beta\,c\,\Delta t\,\overline{\kappa}_p}\right] u_r^n + \frac{\beta\,\Delta t}{1 + \alpha\,\beta\,c\,\Delta t\,\overline{\kappa}_p}\int_0^\infty \int_{4\pi} \overline{\kappa}_\eta I_\eta^\lambda\,d\Omega\,d\eta, \tag{3.14}$$

$$= (1 - (1-\alpha)\,\beta\,c\,\Delta t\,\overline{\kappa}_p)\,f\,u_r^n + f\,\beta\,\Delta t\int_0^\infty \int_{4\pi} \overline{\kappa}_\eta I_\eta^\lambda\,d\Omega\,d\eta. \tag{3.15}$$

The value of u_r that is centered within a time step is defined by,

$$u_r^\gamma = \alpha\, u_r^{n+1} + (1-\alpha)\, u_r^n,$$

$$= f\, u_r^n + \alpha\,\beta\,\triangle t\, f \int\limits_0^\infty \int\limits_{4\pi} \bar{\kappa}_\eta\, I_\eta^\lambda\, d\Omega\, d\eta,$$

$$= f\, u_r^n + \frac{1-f}{c\,\kappa_p} \int\limits_0^\infty \int\limits_{4\pi} \bar{\kappa}_\eta\, I_\eta^\lambda\, d\Omega\, d\eta. \tag{3.16}$$

Using the time centered value of radiation energy density, u_r^γ, and changing I_η^λ to its instantaneous value, equation 3.8 becomes,

$$\frac{1}{c}\frac{\partial I_\eta}{\partial t} + \hat{\mathbf{s}}\cdot\frac{\partial I_\eta}{\partial x} + \kappa_\eta\, I_\eta = \tfrac{1}{2}\,\kappa_\eta\, b_\eta\, c\, f\, u_r^n + \kappa_\eta\, b_\eta\,\frac{1-f}{2\,\kappa_p} \int\limits_0^\infty \int\limits_{4\pi} \kappa_\eta\, I_\eta\, d\Omega\, d\eta. \tag{3.17}$$

The absorption coefficient is interpreted as having effective scattering, $\kappa_{\eta s}$, and effective absorption, $\kappa_{\eta a}$, components as,

$$\kappa_{\eta a} = f\,\kappa_\eta, \tag{3.18}$$

$$\kappa_{\eta s} = (1-f)\,\kappa_\eta. \tag{3.19}$$

Finally, substituting these definitions into equation 3.17 yields a linear transport equation that is used to determine the spectral intensity at t^{n+1} given the value at t^n,

$$\frac{1}{c}\frac{\partial I_\eta}{\partial t} + \hat{\mathbf{s}}\cdot\frac{\partial I_\eta}{\partial x} + (\kappa_{\eta a} + \kappa_{\eta s})\, I_\eta = \tfrac{1}{2}\, b_\eta\, c\, \kappa_{\eta a}\, u_r^n + \frac{\kappa_\eta\, b_\eta}{2\,\kappa_p} \int\limits_0^\infty \int\limits_{4\pi} \kappa_{\eta s}\, I_\eta\, d\Omega\, d\eta + S.$$

$$\tag{3.20}$$

In order to describe the response of the medium to the radiation field, a similar

methodology is applied to equation 3.10, starting with a temporal integration.

$$\frac{u_m^{n+1} - u_m^n}{\triangle t} = \int\limits_0^\infty \int\limits_{4\pi} \overline{\kappa}_\eta I_\eta^\lambda d\Omega \, d\eta - c \, \overline{\kappa}_p u_r^\gamma. \tag{3.21}$$

Substituting u_m values for u_r in equation 3.16, substituting the instantaneous value for I_η^λ and constant values for averaged quantities, and finally solving for u_m^{n+1}, gives

$$\frac{u_m^{n+1} - u_m^n}{\triangle t} = \int\limits_0^\infty \int\limits_{4\pi} \overline{\kappa}_\eta I_\eta^\lambda d\Omega \, d\eta - c \, \overline{\kappa}_p \left(f \, u_r^n + \frac{1-f}{c \, \kappa_p} \int\limits_0^\infty \int\limits_{4\pi} \overline{\kappa}_\eta I_\eta^\lambda \, d\Omega \, d\eta \right), \tag{3.22}$$

$$u_m^{n+1} = u_m^n - c \, \kappa_p \, f \, \triangle t \, u_r^n + \triangle t \int\limits_0^\infty \int\limits_{4\pi} \kappa_\eta \, I_\eta \, d\Omega \, d\eta. \tag{3.23}$$

For a perfect gas, the material energy density can be assumed as $u_m = c_v T$ [67], which produces

$$T^{n+1} = T^n - \frac{1}{c_v} \left(c \, \kappa_p \, f \, \triangle t \, u_r^n - \triangle t \int\limits_0^\infty \int\limits_{4\pi} \kappa_\eta \, I_\eta \, d\Omega \, d\eta \right). \tag{3.24}$$

To summarize, modeling the isotropic radiative thermal transport through a perfect gas with no physical scattering requires the solution of the following equations,

$$\frac{1}{c} \frac{\partial I_\eta}{\partial t} + \mathbf{\hat{s}} \cdot \frac{\partial I_\eta}{\partial x} + (\kappa_{\eta a} + \kappa_{\eta s}) \, I_\eta =$$

$$\hspace{3cm} \sfrac{1}{2} \, b_\eta \, c \, \kappa_{\eta a} \, u_r^n + \frac{\kappa_\eta \, b_\eta}{2 \, \kappa_p} \int\limits_0^\infty \int\limits_{4\pi} \kappa_{\eta s} \, I_\eta \, d\Omega \, d\eta + S, \tag{3.25a}$$

$$\kappa_{\eta a} = f \, \kappa_\eta, \tag{3.25b}$$

$$\kappa_{\eta s} = (1 - f) \, \kappa_\eta, \tag{3.25c}$$

$$f = \frac{1}{1 + \alpha \, \beta \, c \, \triangle t \, \kappa_p}, \tag{3.25d}$$

$$T^{n+1} = T^n - \frac{1}{c_v} \left(c \, \kappa_p \, f \, \triangle t \, u_r^n - \triangle t \int\limits_0^\infty \int\limits_{4\pi} \kappa_\eta \, I_\eta \, d\Omega \, d\eta \right). \tag{3.25e}$$

The Fleck factor controls the relative size of the effective absorption and scattering coefficients. In opaque regions, κ_p is large, which decreases the Fleck factor, and hence increases the amount of effective scattering. With decreasing temporal resolution, the stability of the solution is maintained through an increase in information about the solution, due to a higher probability of scattering events. However, at sufficiently low spatial resolution the solution can exhibit unphysical behavior[34, 71].

3.1.2 Monte Carlo Interpretation

The procedure involved in the MCM solution of the transport equations 3.25a is presented here. The initial properties of particles generated are governed by the radiative energy source from which they are emitted. Particle sources include thermal radiation from the medium, particles not terminated in previous time steps, and external sources. To determine the total energy emitted from a cell, Q_m, during a time step as a result of the medium, the first term on the right hand side of equation 3.25a must be integrated over direction, wavenumber, space, and the time step.

$$Q_m = \frac{c}{2} \int\limits_{t^m}^{t^{n+1}} \int\limits_{\mathbf{X}} \int\limits_0^\infty \int\limits_{4\pi} b_\eta \, \kappa_{\eta a} \, u_r^n \, d\Omega \, d\eta \, d\mathbf{x} \, dt \tag{3.26}$$

$$= c \, \triangle t \int\limits_{\mathbf{X}} f \, \kappa \, u_r^n \, d\mathbf{x}. \tag{3.27}$$

A common external radiative source in radiative transport problems is a blackbody. The total energy emitted from a blackbody is the blackbody emissive power integrated over wavenumber, the surface area of the blackbody, and the time step.

$$Q_b = \int_{t^m}^{t^{n+1}} \int_A \int_0^\infty E_{b\eta}\, dA \tag{3.28}$$

$$= \frac{a\, c}{4} \int_A T_s^4\, dA, \tag{3.29}$$

where T_s is the surface temperature of the blackbody. Another source of particles in a time dependent problem are census particles, which are particles that have not been absorbed in the previous time step. Census particles can be combined or split in order to reduce variance, but in this thesis all census particles continue their path at the start of the next time step.

The distribution of emitted particles among energy sources can be selected in different ways. Particles can be distributed in a stochastic manner, with the probability of emission from an emission source being the fraction of energy emitted by that source compared to the total emitted energy of the problem. Typically, for this case, the initial energy for all particles is defined by the user at the start of the solution. Alternatively, at the beginning of a time step, the number of particles to be emitted by a source can be determined based on the fraction of total energy emitted by the source compared to the total emitted energy. For this method, initial particle energy is the energy emitted from the source divided by the number of particles allocated to that source. The user input in this case is the number of particles to be used for the simulation. For this thesis, the second method is used with the modification that there is a minimum number of particles for sources, so even low flux sources generate particles during a time step. This modification does result in a decrease in computational efficiency, as it adds to the number of particles that need to be propagated.

Additionally, the contribution of particles emitted from low flux sources to the overall radiative flux are lower than other particles; however, it ensures that the energy flux from every cell contributes to the solution.

The initial position of a source particle is randomly sampled within the spatial envelope of the source from where it is emitted. For the case of a blackbody source, the initial position of the particle lies on a random point on the blackbody surface. Similarly for a thermally emitted particle in a cell, the initial position is a random point within the cell volume. Methods of distributing initial locations of thermally emitted particles are discussed in section 3.1.3. The initial position of a census particle is simply the position of that particle at the end of the previous time step. There are different mathematical methods for sampling the isotropic directional distribution. The method shown in equations 3.30a shows the lowest computational cost for 3D directional sampling in Cartesian coordinates out of several isotropic sampling methods that were tested.

$$r_1^2 + r_2^2 \leq 1, \tag{3.30a}$$

$$\Omega_i = 2\, r_1 \sqrt{1 - r_1^2 - r_2^2}, \tag{3.30b}$$

$$\Omega_j = 2\, r_2 \sqrt{1 - r_1^2 - r_2^2}, \tag{3.30c}$$

$$\Omega_k = 1 - 2\left(r_1^2 + r_2^2\right), \tag{3.30d}$$

where r_1 and r_2 are random numbers distributed uniformly on $[-1, 1]$, and Ω_i, Ω_j, Ω_k are the normalized vector components of the particle's direction. The sampling of the particle's wavenumber is discussed in section 3.2.

With the particle's initial position, direction, energy, and wavenumber specified, the particle can now be tracked through the medium. As the particle moves through a cell, it can undergo an interaction event with the medium, reach the end of the time step, or reach the edge of the cell boundary. To determine which possibility is

sampled, the distance to each potential event is calculated and the minimum distance is chosen. Efficient calculation of the distance to the cell boundary depends on the coordinate system, problem dimensionality, and the grid structure used. The distance the particle travels until the end of the time step is calculated as,

$$d_{cen} = c \left(t^{n+1} - t \right).$$

<div align="right">(3.31)</div>

To sample the distance for an interaction with the medium, equation 2.8 is integrated over a path of length s,

$$I_\eta s \left(s \right) = I_\eta \left(0 \right) e^{-\int_0^s \kappa_\eta \, ds},$$

<div align="right">(3.32)</div>

$$\frac{I_\eta s \left(s \right) - I_\eta \left(0 \right)}{I_\eta \left(0 \right)} = e^{-\int_0^s \kappa_\eta \, ds}.$$

<div align="right">(3.33)</div>

Equation 3.33 is the fraction of energy that reaches point s, and is set equal to a uniformly distributed random number, r on $(0, 1]$. The resulting equation is inverted to find

$$d_{coll} = \frac{-\ln \left(r \right)}{\kappa_\eta}.$$

<div align="right">(3.34)</div>

Since the distance to collision is sampled from an exponential distribution, each successive sampling is independent of the last sampling, as exponential distributions are the only continuous random distributions that are memoryless[55]. This means that the probability of particle interaction is uncorrelated with previous interaction probabilities. However, this does not negate the need to consider spectral correlations for banded spectral models.

If the distance to the cell boundary is selected, then the particle is moved to the boundary of the appropriate cell and the distance calculations are made again using the new cell's properties. The exception to this is when the particle is to

move outside the problem domain, in which case the particle can be modified or terminated as appropriate for the local boundary condition. As noted earlier, if the particle reaches the end of the time step, its properties are stored in a census particle to be propagated in the next time step. For each collision event, the particle is either absorbed or scattered with probabilities f and $(1 - f)$, respectively. If an absorption event is sampled then the particle history is terminated and its energy is deposited into its current cell. Scattering events result in the re-sampling of the particle direction and wavenumber. Particle energy does not need to be deposited during a scattering event, but some fraction can be deposited in order to reduce variance in the solution. This thesis uses a weighted absorption variance reduction technique that eliminates any absorption or scattering energy deposition and continuously deposits a fraction of the particle's energy into cells as particles move through them proportional to the probability of particle absorption in that cell,

$$\triangle Q = Q_o \left(1 - e^{-f \kappa_\eta s}\right),\tag{3.35}$$

where Q_o is the initial energy of the particle and $\triangle Q$ is the energy that is deposited as a result of the particle traveling a distance s through the cell. Once the fraction of a particle's current energy to its initial energy falls below a predefined value, the remaining energy is deposited into the current cell and the particle is terminated. This method ensures that all potential absorption locations along the geometric path taken by the particle contribute to the solution with the appropriate weight, which is determined from the effective absorption coefficient. Note that for this variance reduction technique there are no absorption events and so equation 3.34 becomes

$$d_{coll} = \frac{-\ln(r)}{(1 - f) \kappa_\eta}.\tag{3.36}$$

All transfer of energy to cells as described above is carried out by adding an

amount of energy from the particle to the current cell. This can result in significant truncation errors if a data type of insufficient precision is used for storing cell energy. In summation operations where truncation errors are suspected, this thesis employs the use of a technique described by Kahan[30]. The Kahan algorithm effectively doubles the precision of the double precision datatype used for these calculations, without relying on the platform-specific implementation of the long double datatype, and demonstrates similar computational performance.

With the radiative energy emitted within a time step distributed by the particles or carried into the next time step, the material properties need to be updated for the next time step. Cell temperatures are updated as determined by equation 3.25e restated here,

$$T^{n+1} = T^n - \frac{1}{c_v} \left(c\, \kappa_p\, f\, \triangle t\, u_r^n - \triangle t \int\limits_0^\infty \int\limits_{4\pi} \kappa_\eta\, I_\eta\, d\Omega\, d\eta \right). \qquad (3.37)$$

The value T^n is the temperature at the start of the time step which determines the internal thermal energy of the cell, and the bracketed term is the energy emitted by the cell minus the energy absorbed by the cell from the radiation field. Any cell quantities dependent on temperature are updated as well.

3.1.3   Teleportation Correction

In addition to improving computational efficiency and stability, the effective scattering introduced by the IMC method also reduces teleportation error. While particles can be emitted from an incorrect location, each scattering event is similar to an immediate re-emission from an absorption location. A decrease in the Fleck factor due to a smaller time step will reduce the probability of scattering events, which is the second mechanism that increases teleportation error with decreasing time step mentioned in section 2.2.1.1.

Other methods have been developed for reducing or eliminating teleportation error. Source tilting samples emission locations from a linear fit of the T^4 values from adjacent cells[18]. By taking the local temperature gradient into account, the distribution of emitted particles teleportation error is reduced, but not eliminated. The use of a functional expansion tally, which retains spatial information using specified basis functions, has also been shown to reduce teleportation error[10]. Ahrens and Larsen take another approach, which involves eliminating approximations made in the IMC method and tracking particles after absorption with re-emission taking place after a sampled delay time[1]. This method eliminates teleportation error, but is currently formulated for a medium with static properties and has additional computational costs for tracking not only actively propagating particles, but absorbed particles as well.

A method inspired by the Ahrens and Larsen approach is presented here, which modifies the IMC implementation to emit particles from sampled absorption points from a previous time step. The use of the weighted absorption variance reduction technique means that a particle deposits energy along its path rather than at a discrete point. Particles are typically terminated at points where they carry only a small fraction of their initial energy, so the termination point is not necessarily coincident with areas of large energy deposition. In order to generate a distribution of points that are representative of the distribution of deposited energy, emission points are sampled based on the fraction of energy deposited into the medium along a particle path. The probability that a point will be sampled from any particle path is equal to the fraction of the particle's initial energy lost along that path and is given in equation 3.35. Absorption points are sampled along selected paths by,

$$\mathbf{X} = \mathbf{X_o} + \mathbf{\Omega}\frac{-\ln\left(1 - r\left(1 - e^{-f\,\kappa_\eta\,s}\right)\right)}{f\,\kappa_\eta}, \qquad (3.38)$$

where $\mathbf{X}$ is the sampled absorption point, $\mathbf{X_o}$ is the initial point of the path, and r is the uniform random number, bounded by [0,1], used in selecting the path. Sampled absorption points are stored and then randomly selected to be used as emission locations in the next time step. Since the sampling of absorption points is based on the probability of absorption, the number of sampled absorption points will roughly equal the number of terminated particles in the last time step. In subsequent time steps, emission locations are randomly sampled from the stored absorption points, and the used point is deleted from storage such that each point is only used once. If the absorption points are exhausted, then the method utilizes the source tilting method for these additional emission locations. Since there are no stored absorption locations at the start of the first time step, the source tilting method is used for every thermal emission at the start of the simulation.

Since this method requires only the storage of location information, the increase in memory utilization will be proportional to the number of particles in the simulation multiplied by the memory required to store a position. This increase in memory utilization can be reduced by only sampling absorption locations in cells adjacent to large absorption coefficient gradients where teleportation errors tend to be larger. Sampling absorption locations requires minimal additional computational effort if a fast random number generator is used, and this method is relatively simple to include in an existing IMC code.

3.2 Line by Line Spectral Table Implementation

As stated in section 2.3.1, the calculation of absorption coefficient utilizes the parameters found in the HITEMP 2010 database in the equations shown in section

2.3 and restated here,

$$S(T) = S(T_{ref}) \frac{Q\left(T_{ref}\right)}{Q\left(T\right)} \frac{e^{\frac{-E_\eta\,h\,c}{k\,T}}}{e^{\frac{-E_\eta\,h\,c}{k\,T_{ref}}}} \frac{1 - e^{\frac{-\eta_o\,h\,c}{k\,T}}}{1 - e^{\frac{-\eta_o\,h\,c}{k\,T_{ref}}}} \quad cm^2/\text{molecules} \tag{3.39a}$$

$$f\left(\eta, T, p, p_i\right) = \frac{1}{\pi} \frac{\gamma\left(p, T\right)}{\gamma\left(p, T\right)^2 + \left[\eta - \left(\eta_o + \delta\left(p_{ref}\right)\,p\right)\right]^2} \tag{3.39b}$$

$$\gamma\left(T, p, p_i\right) = \left(\frac{T_{ref}}{T}\right)^n \left(\gamma_{air}\left(p_{ref}, T_{ref}\right)\,\left(p - p_i\right) + \gamma_{self}\left(p_{ref}, T_{ref}\right)\,p_i\right) \tag{3.39c}$$

$$\kappa_\eta = \sum_i n_i\,S_i\,f_i = \sum_i \kappa_{\eta,i}. \tag{3.39d}$$

The values for $S\left(T_{ref}\right)$, E_η, γ_{air}, γ_{self}, η_o, n, and $\delta\left(p_{ref}\right)$ are read from the HITEMP 2010 database for each transition. $Q\left(T\right)$ is calculated from a third degree polynomial with coefficients specified in the database for various temperatures. The spectrum is discretized into $0.01\,cm^{-1}$ intervals with a range of $0 - 8000cm^{-1}$ which accounts for 99.7% of emitted radiation for the problem of interest. Following the method described by Wang[68], the wavenumber resolution is considered to be adequate as the absorption coefficient shows less than 1% error across absorbing bands. The absorption coefficient for each wavenumber can be found by a summation of the contribution from every transition. Since the profile for each transition is typically negligible a few cm^{-1} from the transition wavenumber, it is more efficient to only consider the range

$$\triangle\eta = \eta_o - \gamma\,tan\left(\pi\left(acc - 0.5\right)\right), \tag{3.40}$$

where acc is the fraction of the line profile to be taken into account, which is set at 0.999 for this thesis. A table representing the normalized cumulative absorption coefficients is calculated from a numerical integration of the absorption coefficient table. This process is repeated with a number of temperatures, pressures, and mole fractions, to represent the spectral properties of the problem.

A one dimensional problem, using properties extracted from the three dimensional problem of interest, is used to test the accuracy of the absorption coefficient tables. The reference solution for one of these problems is generated by using spectral property tables which are generated for each cell condition. The table is considered to be acceptable when the error of the spectral radiative heat transport across major bands is below 1% for several sample problems. A table with 2 mole fractions, 2 pressures, and 26 temperatures meets this criterion for water and is used to produce the solutions presented in this thesis.

The low number of pressure and mole fraction points is expected as these parameters only impact the line width, and have a similar influence on all absorption lines. Some species, such as carbon dioxide, show negligible self broadening effects and can be represented by a single mole fraction[68]. The temperature dependencies of line width and strength can vary significantly across absorption lines resulting in absorption coefficients with dissimilar and irregular temperature dependencies.

3.3   Implicit Monte Carlo and Line by Line Computer Codes

The computer codes for the IMC and LBL models are written in the C++ programing language, and use the Message Passing Interface (MPI) to enable the codes to run in parallel across multiple processor cores. The LBL code is run independent of the IMC code, and computes the absorption coefficient and normalized cumulative absorption coefficient tables. The output tables are typically in a binary format, as binary files can be loaded into system memory faster than ASCII formatted files. Since the source files from the HITEMP 2010 data base, LBL computation, and output file format are static, the LBL code does not need to be changed for different simulations, and is written using a single source file. The IMC code uses the spectral property tables describing the spectral properties of the medium, and the spatial grid describing the thermodynamic properties of the medium as inputs. Object oriented

programing and templating are used to write the IMC code, which enables the core transport code to be utilized with different spatial dimensions and opacity models. For example, the geometry code has different implementations for one and three dimensional geometries. Both implementations have a common structure for outside objects to access data or functions. Furthermore, the use of templates allows the objects representing the geometry to be passed to other objects in the program. In this framework, the implementation of geometry, spectral properties, and supporting mathematical functions can be modified independently without changing other areas of the code.

3.3.1   Implicit Monte Carlo Code and Line by Line Code Verification

The IMC code was verified against the example problem published in the Fleck and Cummings paper[29]. It is a one dimensional problem of a 4cm thick initially cold slab at t=0seconds, heated by a 1keV blackbody at x=0cm. The simulation domain is divided into 10 cells, uses time steps of $2x10^{-11}$seconds, and one million particles. This problem specifies the following relations for absorption coefficient and coefficient of specific heat:

$$\sigma = \frac{2700}{\nu^3}\left(1 - e^{-\nu/T}\right),\tag{3.41}$$

$$c_v = 0.5917\,a\,T^3.\tag{3.42}$$

Figures 3.2 and 3.3 show the temperatures of the slab at three different times. The material near the blackbody source heats quickly as radiation is absorbed in those cells. The absorption coefficient is high enough in those cells to prevent significant radiative transport to cells more distant from the source. The absorption coefficient decreases with increasing temperature, which allows additional radiation from the source to propagate into the slab along with thermally emitted radiation from hot

cells. The results using the IMC code in Figure 3.3 agree with the published Fleck and Cummings results in Figure 3.2, verifying the code is using the IMC method correctly.
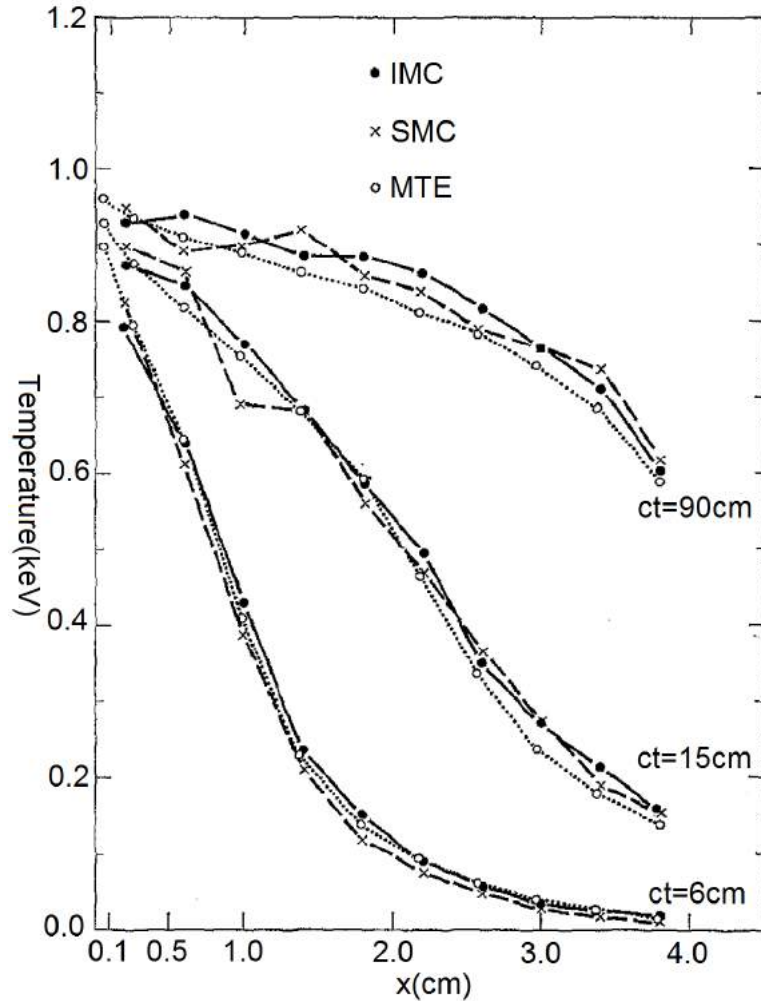

Figure 3.2: Fleck and Cummings published results[29]

Figure 3.4 shows the emission of water vapor at the listed conditions for several different spectral databases compared to an experimental measurement. The HITEMP 2010 database is largely based on the BT2 database which is shown to compare well with experimentally obtained values[56]. Figure 3.5 shows the results of the LBL code utilizing the HITEMP 2010 database. The values agree well with the BT2 results, with two exceptions near $1.35 \mu m$. These errors are caused by the entries for two ab-
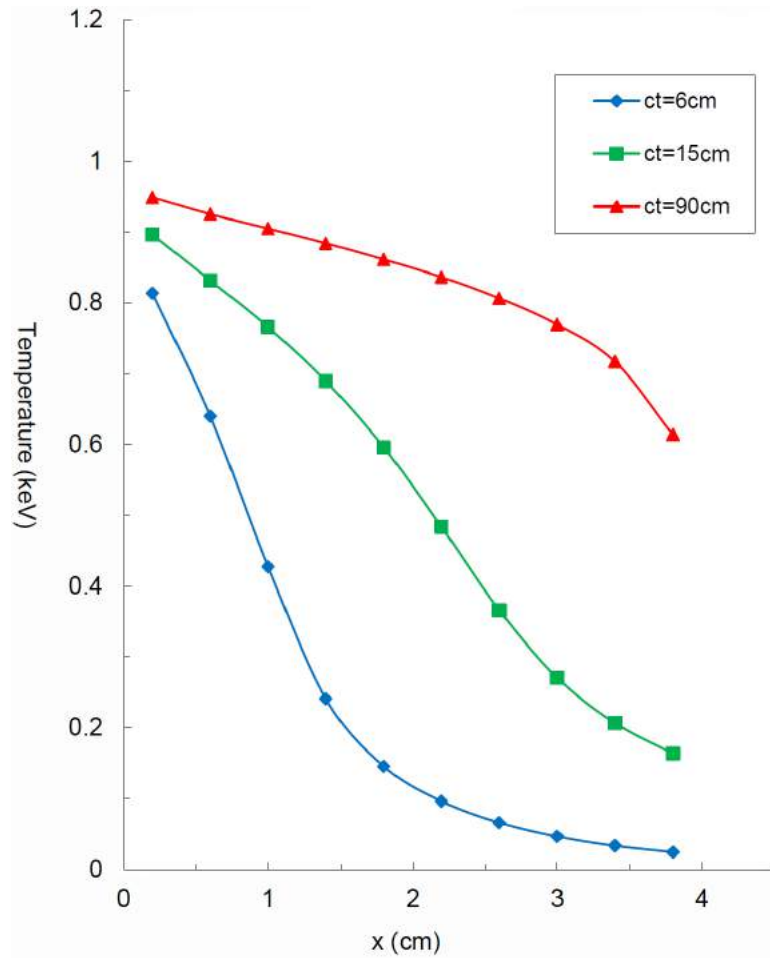
Figure 3.3: IMC verification results

sorption lines utilizing incorrect data within the HITEMP 2010 database. With the exception of Figure 3.5, the results presented in this thesis utilize a corrected copy of the HITEMP 2010 database using corrected entries provided by Dr. Rothman for the erroneous absorption line entries. The corrected database agrees well with the BT2 results shown in Figure 3.4, verifying the code is correctly conducting LBL calculations using the HITEMP 2010 database.

3.4 Summary

The IMC method, a stochastic method of solving the radiative thermal transport equations, is described in this section. The IMC simulation requires knowledge of
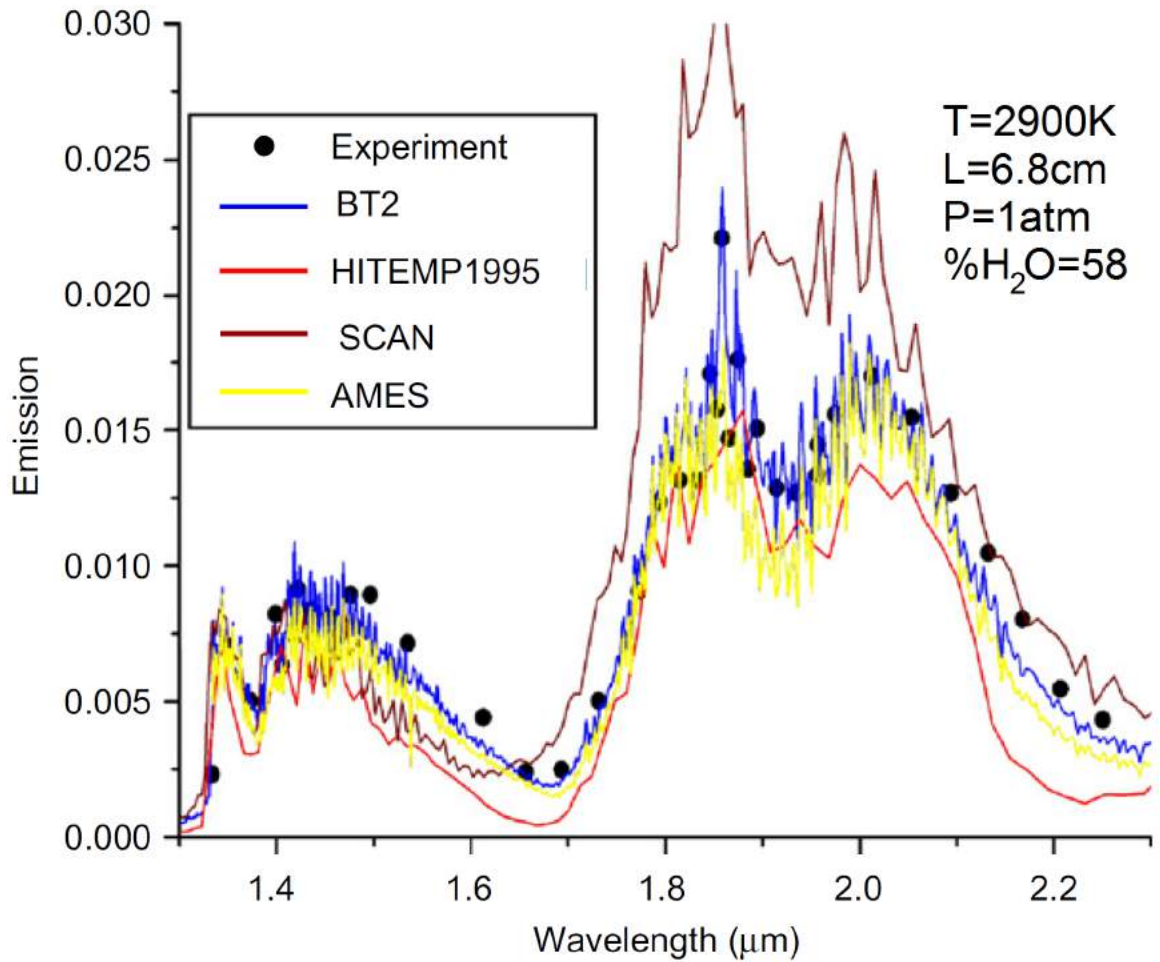
Figure 3.4: Rothman published HITEMP 2010 comparison of different spectral databases[56]

the spectral properties of the medium, which are supplied by look-up tables. These look-up tables are created using the LBL method described in this section. The LBL method calculates the absorption coefficient using absorption line properties supplied by the HITEMP 2010 database. The computer codes implementing the IMC and LBL methods are discussed as well as the interaction of these codes.
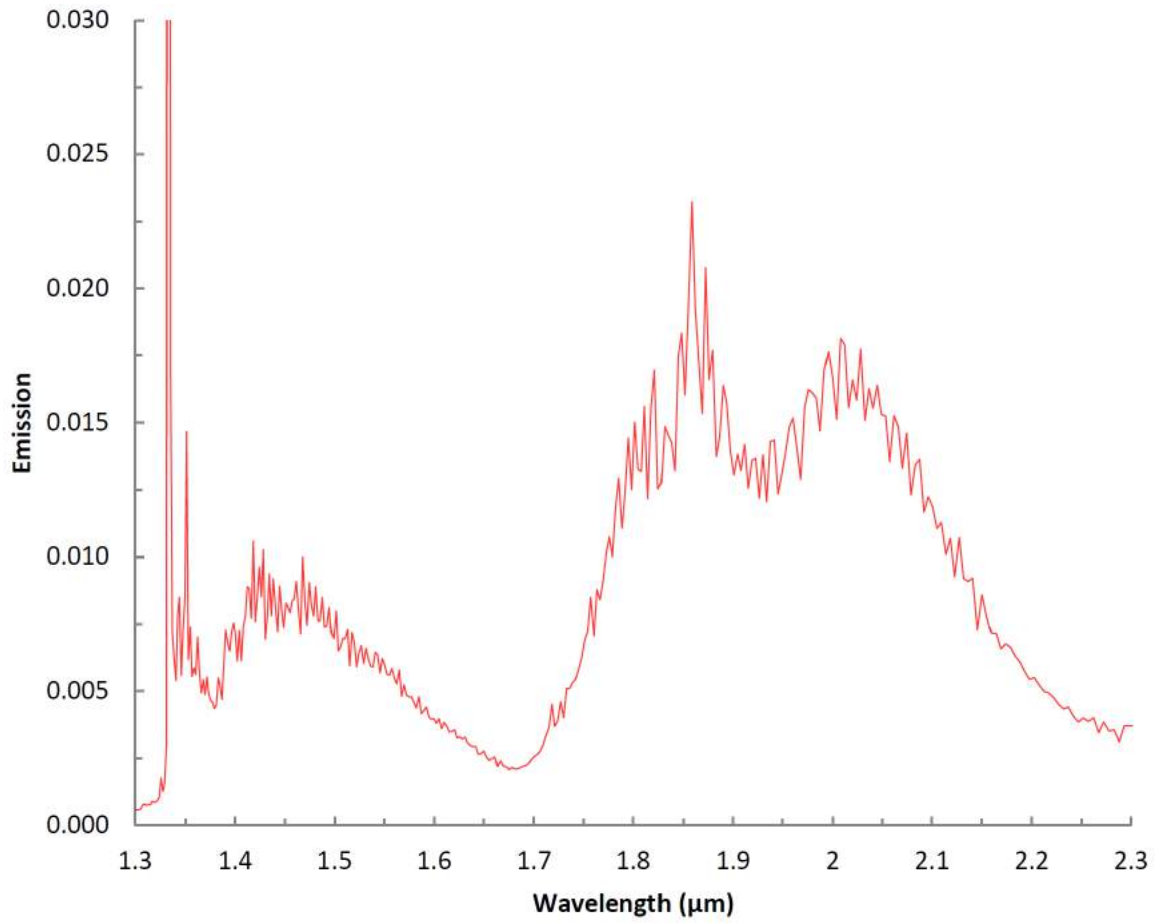
Figure 3.5: LBL verification results using uncorrected HITEMP 2010 database

CHAPTER IV

The Hypersonic International Flight Research and Experimentation Program

The HIFiRE program is a joint effort between the United States Air Force Research Laboratory (AFRL) and the Australian Defense Science and Technology Organization (DSTO) to develop hypersonic technologies and investigate the underlying physics[31]. "The objectives of the HIFiRE Program are to increase understanding in fundamental hypersonic phenomena and enable research and exploration in flight regimes expensive and difficult to model with existing codes and test in existing ground test facilities"[28]. The approach is a combination of Computational Fluid Dynamics (CFD), ground simulations and experiments, and flight tests. There are three hydrocarbon fueled scramjet flight test vehicles that are a part of the HIFiRE program[3]. The availability of experimental data and computational analysis of these vehicles is why the HIFiRE program is of interest to the PSAAP for uncertainty quantification and validation, in particular the HIFiRE-2 vehicle. In this thesis, CFD solutions of the flow through the HIFiRE-2 scramjet provide the thermodynamic properties of the medium that are used in the radiative thermal transport simulations.

4.1 Description of the HIFiRE-2 Scramjet

The HIFiRE-2 vehicle is primarily designed to investigate transition from subsonic to supersonic combustion using a hydrocarbon fuel, and was successfully launched in May 2012. The vehicle is propelled to the experiment's desired altitude and velocity by a three stage sounding rocket with the trajectory shown in figure 4.1. The third stage continues to accelerate the vehicle from Mach 5.5 to 8.8 through the experimental portion of the flight. Once the third stage burns out, the vehicle is in freefall until impact with the ground[28].
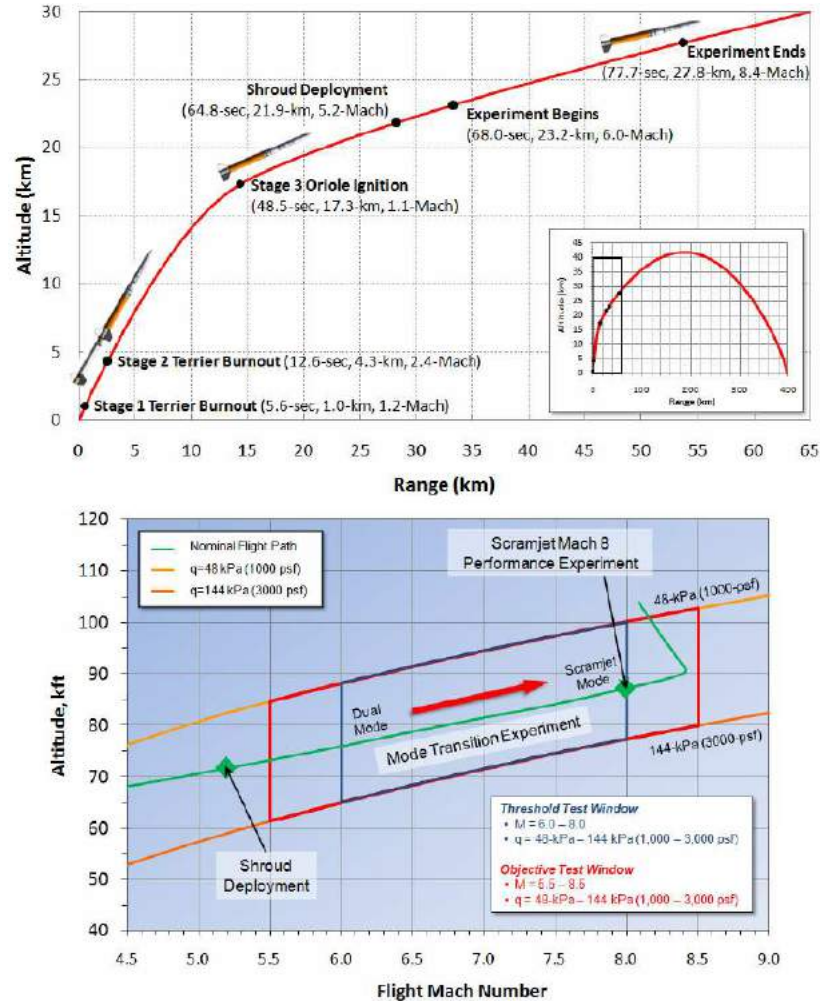
Figure 4.1: HIFiRE-2 Flight Trajectory[28]

Figure 4.2 shows a cutaway of the HIFiRE-2 vehicle[26]. During the boost phase,

64

the flight vehicle is protected by a shroud, which separates before the experimental phase begins. Air enters the inlet at supersonic speeds, and is compressed by a combination of strong shocks reflecting off internal walls and decreasing cross sectional area. The compressed air flows through the isolator region and fuel is primarily injected through four ports each for both the top and bottom walls, at a 15° angle, shortly before the cavity flame-holder. Complete combustion of the air-fuel mixture is desirable for optimal efficiency of the scramjet; however, the supersonic speed of the flow leaves little time for combustion to take place. The cavity flameholder is designed to recirculate a portion of the flow, improving combustion stability and increasing the range of operating conditions of the HIFiRE-2 scramjet with low efficiency losses[39]. A secondary set of four fuel injection ports each for both the top and bottom walls are located behind the flameholder perpendicular to the flow. Temperatures are higher at the secondary fuel injection ports, due to combustion of primary fuel, which leads to faster combustion of secondary fuel. Finally, the burning mixture expands through the nozzle and exits the vehicle. After the inlet section, the scramjet has a constant width of 101.6mm, with the two dimensional profile shown in figure 4.3, and the locations of labeled stations in table 4.1. In both figures 4.2 and 4.3, flow is from left to right.
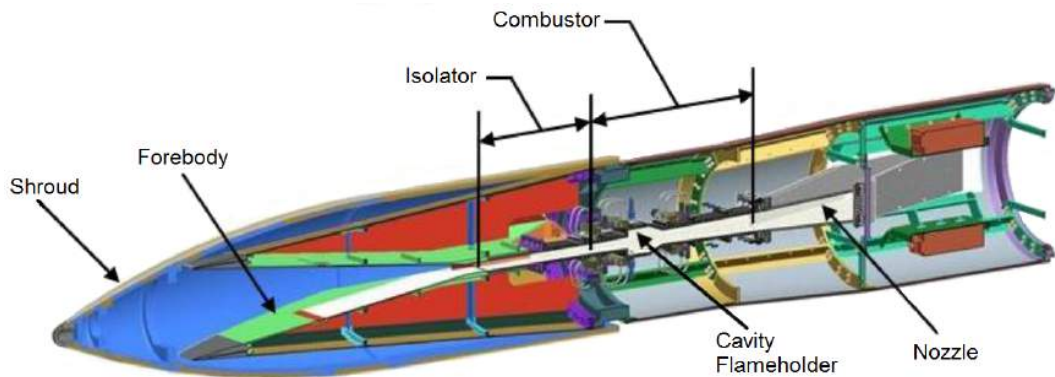

Figure 4.2: Cutaway of HIFiRE-2 flight vehicle[28]

Hydrogen has a desirable fast reaction rate with air; however, due to concerns
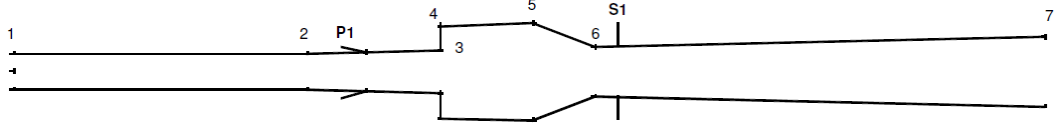
Figure 4.3: HIFiRE-2 flowpath profile[24]

Station	x(mm)	y(mm)
1	0.0	12.7
2	203.2	12.7
P1 (Primary fuel ports)	243.7	13.6
3	294.5	14.8
4	294.2	31.9
5	359.4	33.4
6	401.2	17.2
S1 (Secondary fuel ports)	419.1	17.6
7	742.9	24.2

Table 4.1: HIFiRE-2 geometry data[24]

over logistics support and volumetric efficiency, AFRL is interested in development
of hydrocarbon fueled scramjet engines. An operational system will likely use JP-7
for fuel, which is a hydrocarbon fuel with high thermal stability. The fuel is used
to cool the engine walls, a process that partially decomposes the fuel. The HIFiRE-
2 scramjet does not utilize fuel cooling, as the experiment is too short to generate
enough heat. Since the partially decomposed products of JP-7 have faster reaction
rates than JP-7, a surrogate mixture is used to represent the combustion process. A
volumetric mixture of 64% ethylene and 36% methane shows comparable combustion
to partially decomposed JP-7 in experimental tests, and is used in the HIFiRE-2 flight
vehicle[28].

Ground tests are carried out at the Arc-Heated Scramjet Test Facility (AHSTF)
located at the NASA Langley Research Center, with the scramjet test article directly
connected to the facility, as shown in Figure 4.4. The walls of the scramjet are 2 inch
thick copper with a 0.25 inch thick zirconia thermal barrier coating. Experiments are
conducted using a fixed nozzle geometry, which limits experiments to a fixed Mach

66

number. Upstream pressure is adjusted to reach a desired stagnation pressure at the nozzle exit. An electric arc is used to heat a portion of input air that is mixed with unheated air. Control of the ratio of heated to unheated air as well as heating rate, is used to reach a desired stagnation enthalpy for the experiment. After flowing through the scramjet combustion chamber, gases are collected in large vacuum chambers to maintain back pressure at the scramjet exhaust throughout the experiment. A typical test sequence, shown in figure 4.5, requires approximately 12 seconds to reach the desired flow conditions. Next, an optional time is used to tare the instrumentation before the experiment. A second optional instrumentation tare takes place after the experiment. The arc heater and air supply are shut down after all required data are collected. Up to four tests can be conducted per day[26, 25].
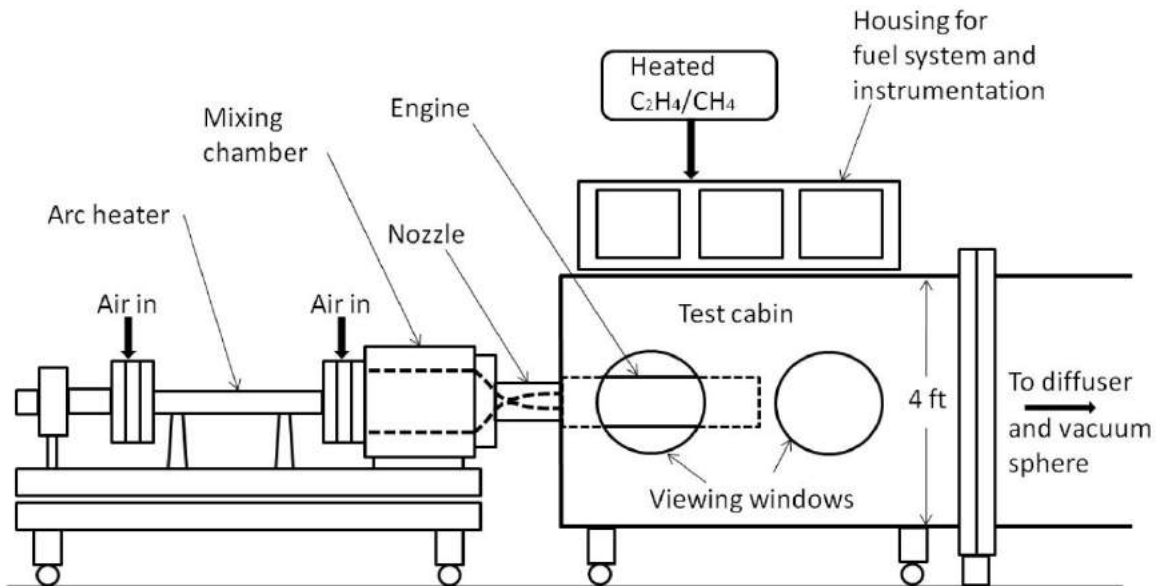

Figure 4.4: NASA Langley's AHSTF diagram

In addition to being unable to reproduce Mach number variation through the HIFiRE-2 flight, Hass describes several other differences between these ground experiments and the flight experiment[26]. A desire to test a full scale combustion chamber, with the size limitations of the facility, leads to the exclusion of the vehicle forebody. The forebody on the flight vehicle causes reflected shockwaves and increases bound-
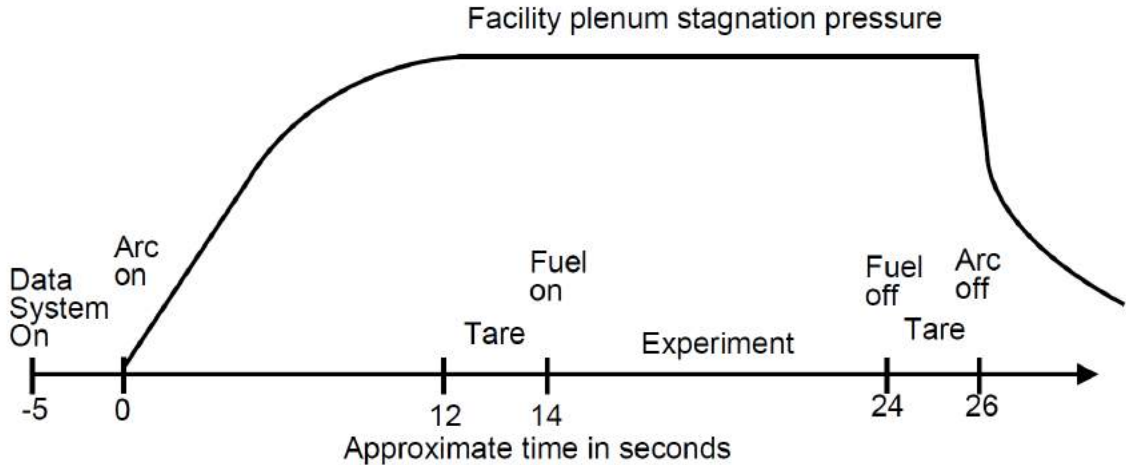
67

Figure 4.5: Example AHSTF experiment timeline

ary layer thickness. Wall temperatures for the ground experiment will be different from the flight vehicle, which can also affect boundary layers and heat transfer. Additionally, electric arc heating in the ground experiments generates nitric oxide not encountered by the flight vehicle, which can influence combustion.

4.1.1 Flowfield Solution Method

The flowfield solutions used in this thesis are supplied by the AFRL, and generated using CFD++, a CFD tool developed by Metacomp Technologies. CFD++ is a general purpose tool capable of utilizing a number of finite volume solution methods. The solutions utilized in this thesis are generated by a Reynolds Averaged Navier-Stokes (RANS) calculation and model turbulence with a two equation cubic $k - \varepsilon$ model. Chemical reactions are modeled with 22 species using reduced reaction mechanisms validated from detailed reaction mechanisms[37]. Bynum lists additional details of the solution methodology in his publication reporting on a HIFiRE-2 CFD solution[5].

For this thesis, a simulation of a HIFiRE-2 ground experiment that replicates a steady state Mach 6.5 flight condition is used. Figure 4.6 shows the domain of the CFD solution, which includes the facility nozzle. The system domain is symmetric

68

along the center-line of the engine, so only a quarter of the system domain is needed to simulate the system with reflecting boundary conditions along lines of symmetry. This thesis uses the shaded quarter of the system domain shown in figure 4.6 for radiative thermal transport simulations. Reflecting boundary conditions are used at $z = 0$ and $y = 0$. Inlet conditions and turbulence modeling parameters for the CFD simulation are calibrated using experimental data gathered at the NASA Langley AHSTF[25, 26, 5]. The additional fuel injection ports shown in figure 4.6 are used to test other fuel injection configurations, but are not used in the flight vehicle and are not considered in the solution used for this thesis. The CFD solution utilized in this thesis utilizes 1.4 million cells and took 10 days to converge on 96 processors[5].

4.1.2   Flowfield Solution

Figure 4.7 shows contours of water vapor mass fraction at several constant z planes. Table 4.2 lists the constant z values used in figures showing z plane contours. Water vapor is produced by combustion of the fuel-air mixture flowing through the scramjet. Water vapor is found up-stream of the primary fuel injection ports due to a recirculation region near the wall upstream of the flameholder cavity. High concentration regions of water vapor due to primary fuel injection disperse inside the cavity flameholder, and additional water vapor is produced by combustion of fuel injected at the secondary fuel ports once mixed with air. Figure 4.8 traces several paths taken by the flow, and shows flow features that include this recirculation region. The distribution of other radiative species, such as carbon dioxide, carbon monoxide, and the hydroxyl radical; show similar characteristics to water vapor.

Constant z plane locations (mm)						
0.00	8.78	17.1	25.4	33.6	41.9	50.2

Table 4.2: Locations of constant z planes used in figures

Emitted thermal radiation is proportional to the number density of radiatively
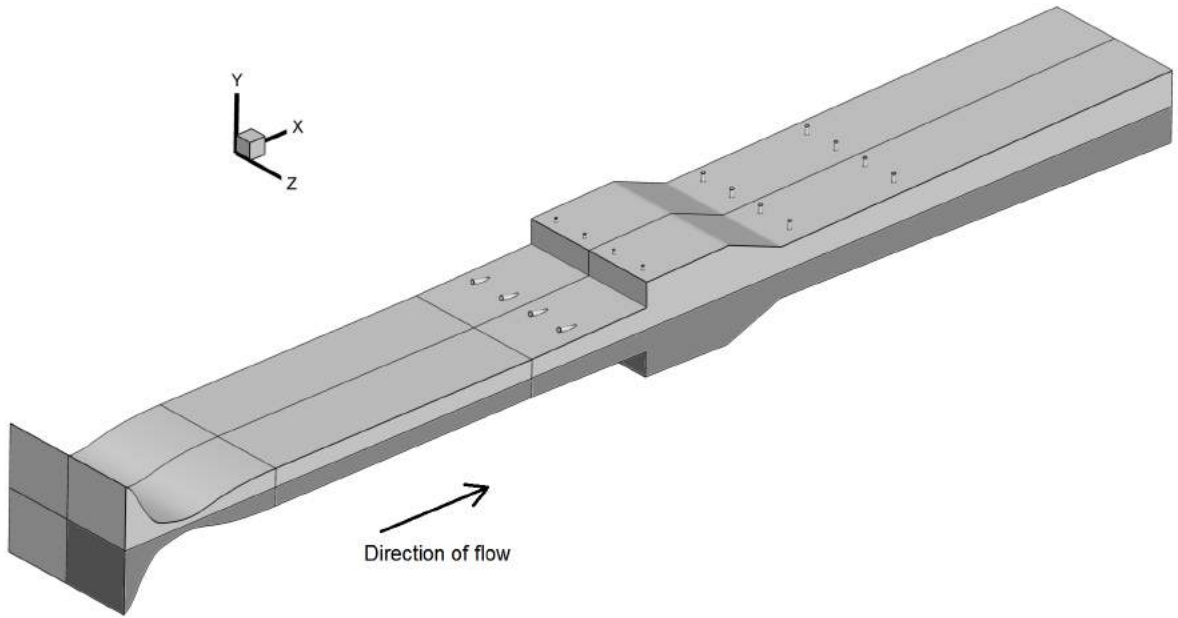
Figure 4.6: Domain of HIFiRE-2 CFD simulation

active species. Since thermal radiation will be negligible in areas with small concentrations of radiative species, the radiative simulation domain below x=235mm can be neglected, resulting in the grid shown in figure 4.9. This grid is used by Crow for Discrete Ordinates Method (DOM) simulations of the HIFiRE-2 scramjet, and is used in this thesis to allow for direct comparison of solutions produced by DOM and IMC[13]. Thermodynamic values from the CFD solution are interpolated onto this grid, and used as inputs for radiative thermal transport simulations.

Figure 4.10 shows temperature of the medium across constant z and x planes. Table 4.3 lists the constant x values used in figures showing z plane contours. The
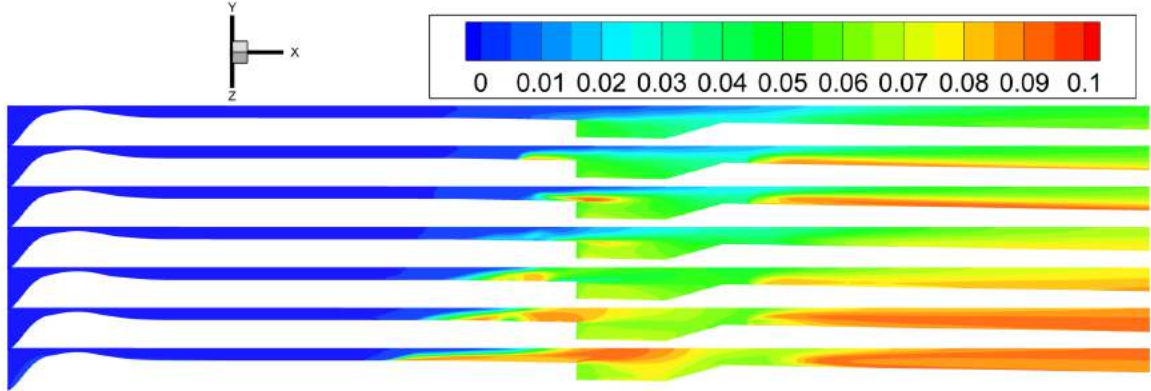
70

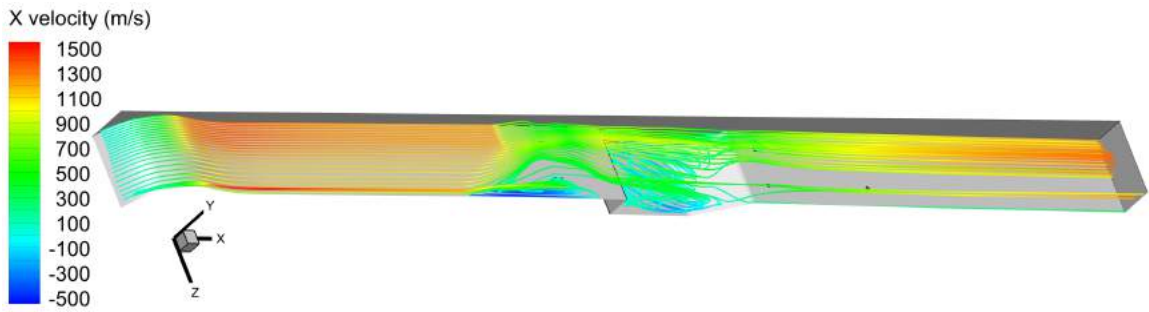Figure 4.7: Contour plots of H_2O mass fraction at six constant z planes

Figure 4.8: Stream traces showing recirculation

fuel is injected at a temperature of 300K, which cools the surrounding medium nearby fuel injection ports. As the fuel travels downstream, it mixes and reacts with air, which heats the medium. The higher temperatures in the flameholder cavity towards the center of the combustion chamber, are a result of longer combustion times due to the recirculation region in the flameholder cavity.

Constant x plane locations (mm)							
234.8	266.6	298.4	330.1	361.9	393.7	425.4	457.2
489.0	520.8	552.5	584.3	616.1	647.8	679.6	742.9

Table 4.3: Locations of constant x planes used in figures

Figure 4.11 shows pressure contours across several constant z and x planes. Shock waves in the isolator cause local areas of high pressure. Added gaseous material, heat, and the area contraction contribute to an increase in pressure at the end of the flameholder cavity. Expansion through the nozzle causes a reduction in pressure as flow
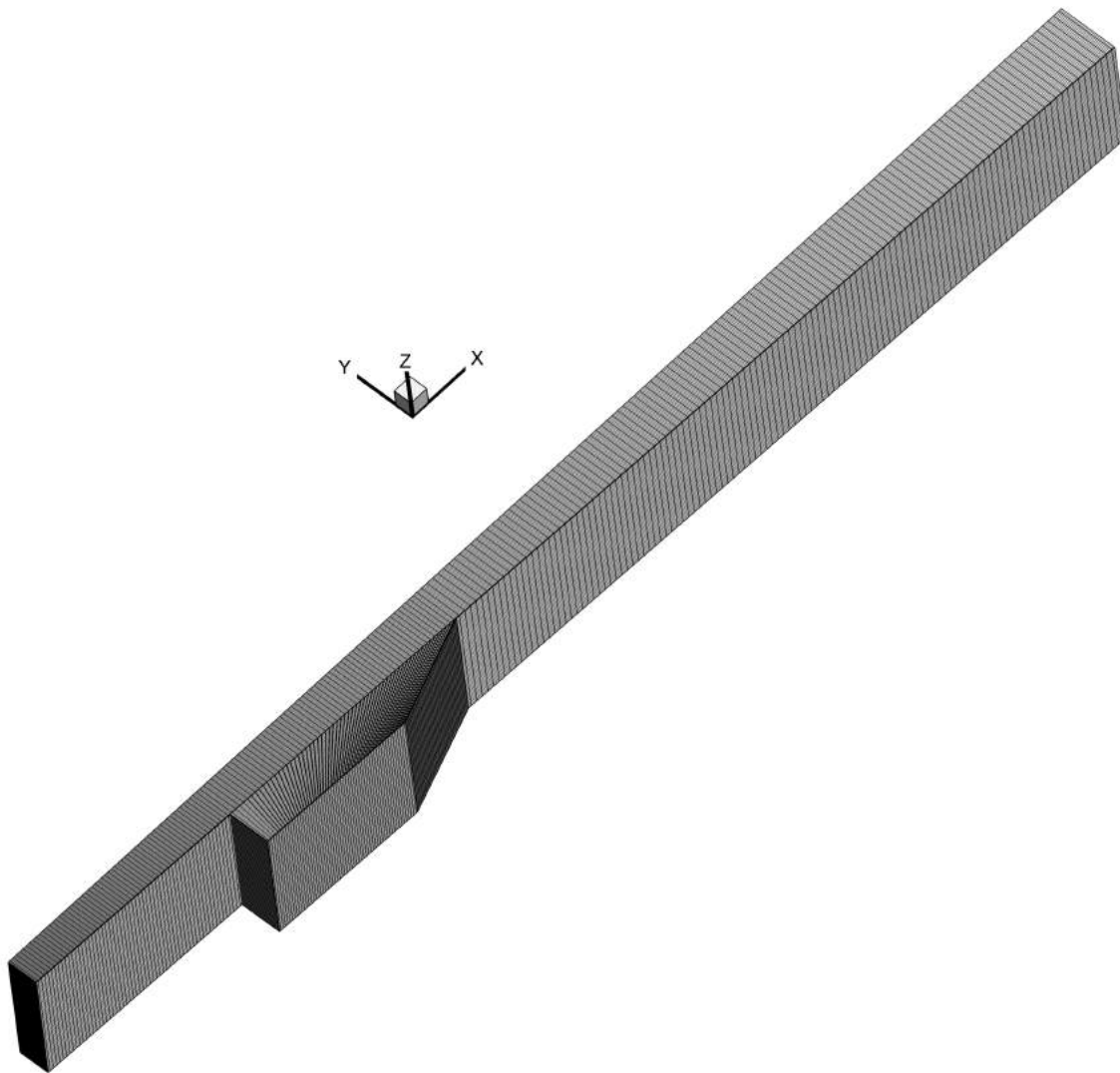
Figure 4.9: Radiative thermal transport simulation spatial grid

accelerates. Figure 4.12 compares pressure measurements from ground experiments to CFD results for the Mach 6.5 condition[5]. The CFD results show good agreement with experimental measurements, particularly in the cavity flameholder and nozzle.

Figure 4.13 shows contours of the mass fraction for the four most significant radiative species in this solution. These species are generated by the combustion of the air-fuel mixture.
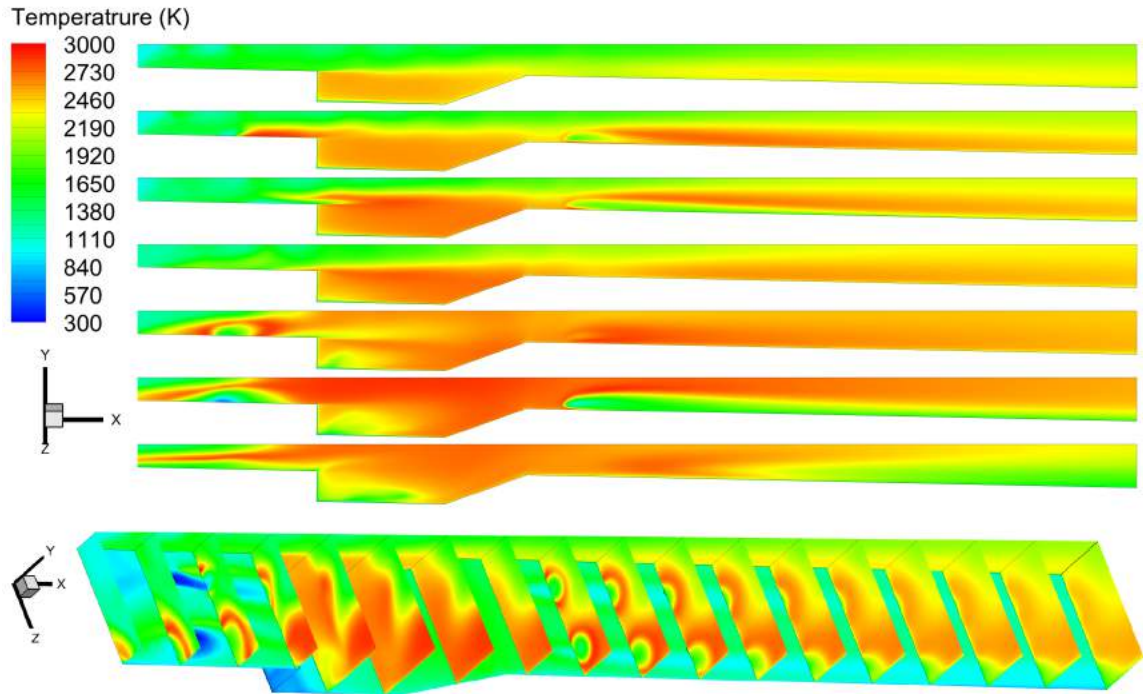
Figure 4.10: Contour plots of temperature

4.2 Summary

The HIFiRE-2 flight vehicle is a hypersonic scramjet propulsion test designed to look at the transition from subsonic to supersonic combustion. The flow features and geometry of the scramjet combustion chamber used in ground testing are identified. A RANS CFD simulation of the flowfield is presented, detailing the distribution of pressure, temperature, and species mass fractions of radiatively active species. These variables are used as inputs for the radiative thermal transport simulation in this thesis.

Figure 4.11: Contour plots of pressure

Figure 4.12: Comparison of pressure from CFD and experiment[5]

Figure 4.13: Mass fractions contours for H_2O, CO_2, OH, and CO

CHAPTER V

Radiative Thermal Transport Solutions of the HIFiRE Scramjet Combustor
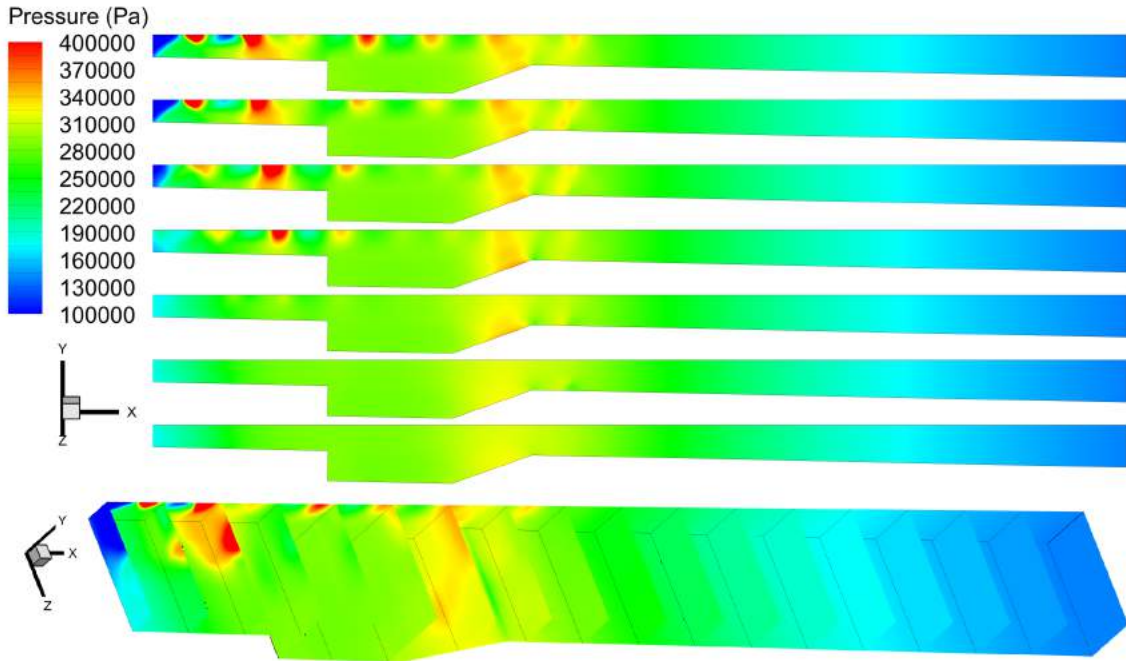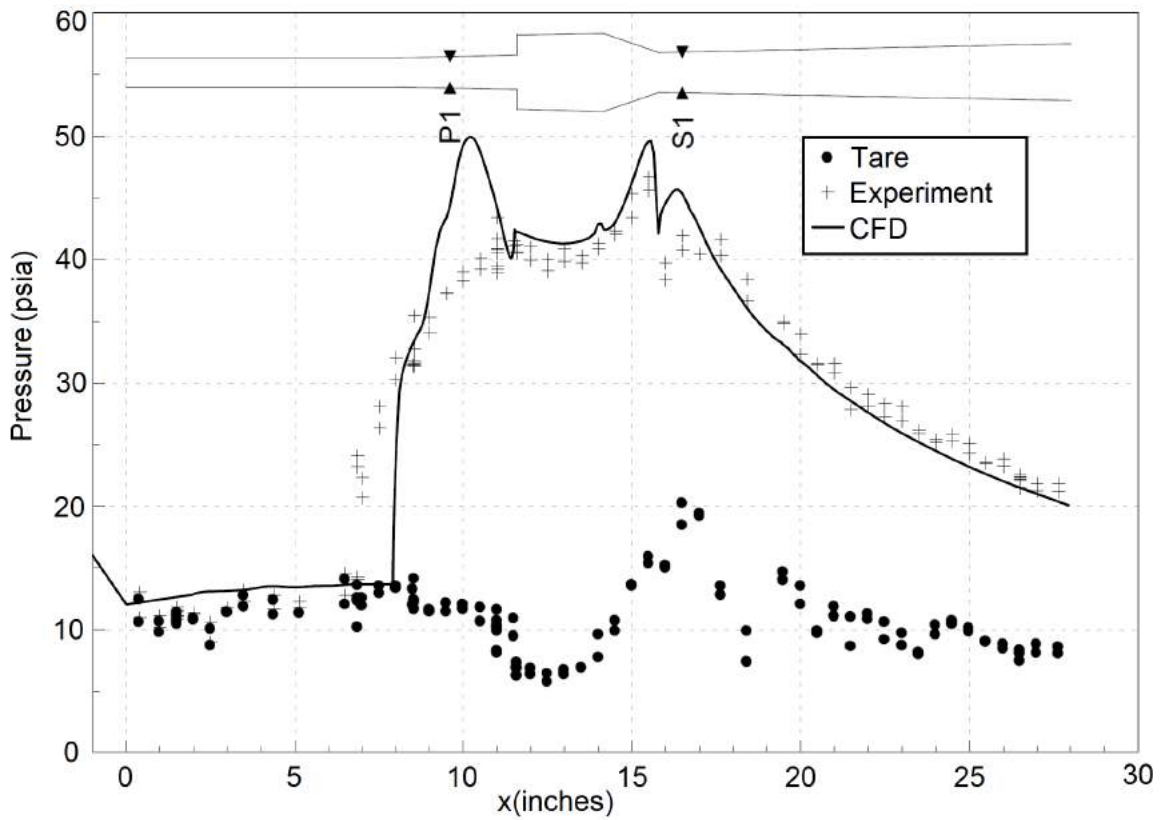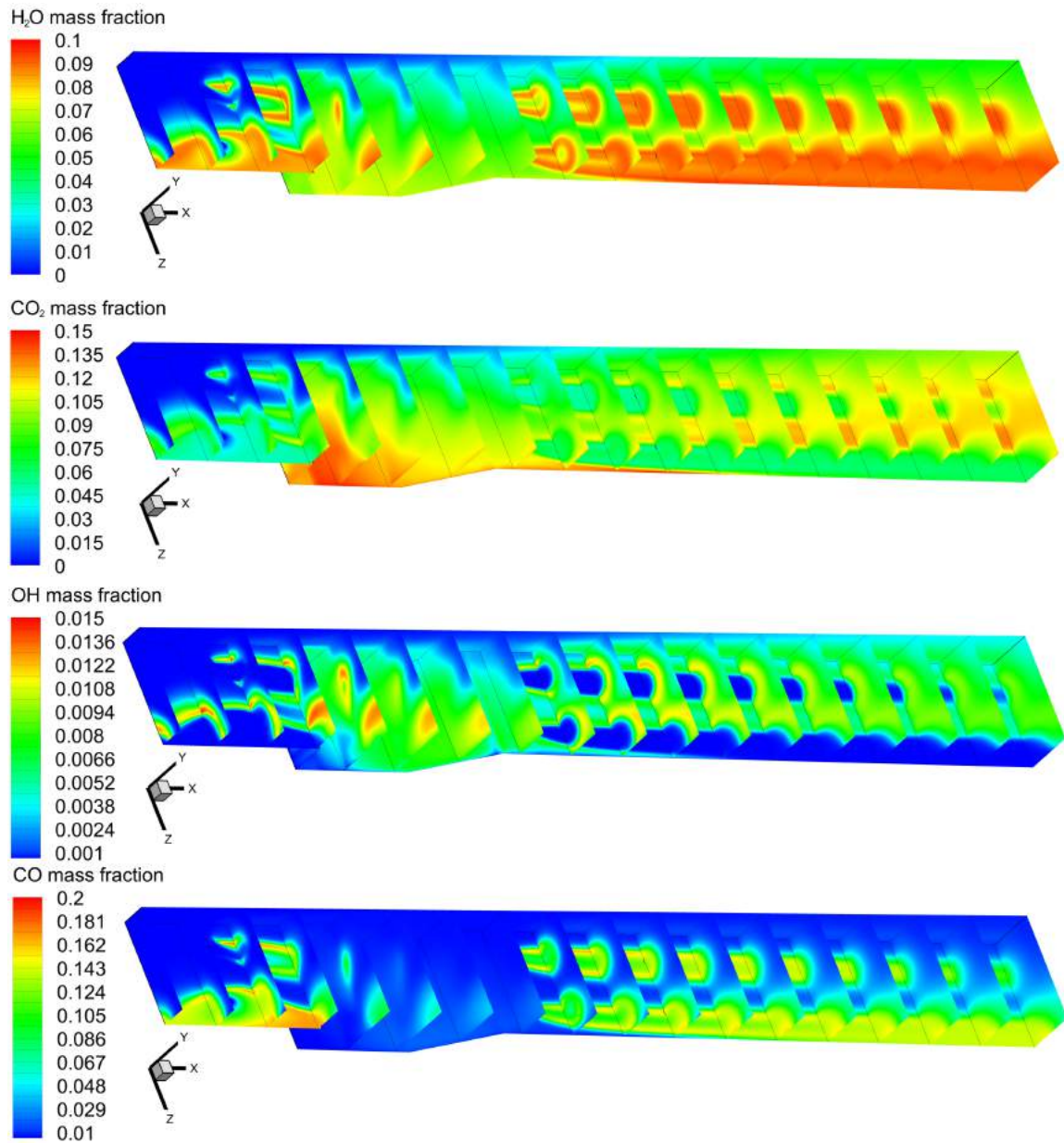
This chapter presents an Implicit Monte Carlo (IMC) solution to the radiative thermal transport based on a Computational Fluid Dynamics (CFD) solution to the flowfield of a HIFiRE-2 ground test simulating Mach 6.5 flight conditions. A table of spectral properties produced by the Line by Line (LBL) method is used by the IMC code to describe the radiative properties of the medium. An assessment of the epistemic uncertainty of the Discrete Ordinates Method (DOM) is made using one dimensional problems with thermodynamic properties taken from the scramjet combustor environment. The IMC method is applied to the three dimensional spatial grid of the HIFiRE-2 scramjet combustor specified in the previous chapter, and the solution is compared to results from the DOM. Finally, one dimensional solutions are used to conduct a sensitivity analysis of the radiative heat flux to the domain boundary to the uncertainty of the absorption line parameters in the HITEMP 2010 database. The results of this analysis are used to estimate the epistemic uncertainty of radiative heat flux in the three dimensional problem due to the HITEMP 2010 uncertainties.
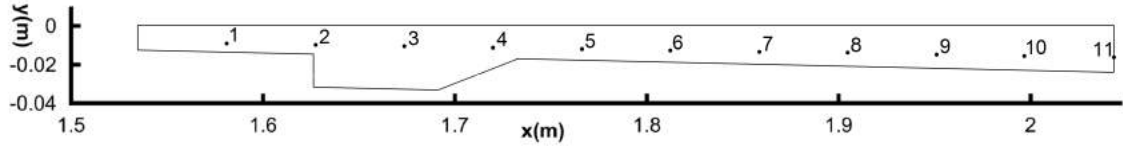
Figure 5.1: One Dimensional problem locations

Point	x coordinate(mm)	y coordinate(mm)
1	281.0	-9.169
2	327.2	-9.867
3	373.4	-10.57
4	419.6	-11.26
5	465.8	-11.96
6	511.9	-12.66
7	558.1	-13.36
8	604.3	-14.06
9	650.5	-14.76
10	696.7	-15.46
11	742.9	-16.15

Table 5.1: Coordinates of one dimensional problems

5.1 HIFiRE One Dimensional Radiation Solutions

An initial assessment of the epistemic uncertainty of the DOM spectral radiative heat flux is made using one dimensional plane parallel simulations. IMC simulations track 10 million particles to populate the spatial and spectral domains. Thermodynamic values are extracted from the three dimensional flowfield solution along lines parallel to the z unit vector. Figure 5.1 shows the locations of these lines, which are placed at regular intervals along the system geometry at one third the height of the primary flow channel. No comparison is made at the upstream boundary at the left side of Figure 5.1, due to low radiative emission in this region resulting from low temperatures and water vapor concentration. There are 60 node points along each line at regular intervals interpolated from the spatial grid shown in Figure 4.9. Table 5.1 lists the coordinates of the one dimensional problems.

Figures 5.2-5.4 show the temperature, pressure, and water vapor mass fractions

plotted against the z coordinate for each of the points shown in Figure 5.1. These quantities directly affect the radiative heat flux. Emitted radiation has a T^4 dependence, leading to the dominance of high temperature regions for emitted radiation. The combined effect of the pressure and mass fraction determine the quantity of radiative material in a cell. The character of profiles show significant differences as the flow passes through two sets of fuel injection ports and the cavity flameholder to the nozzle. Point 1 is relatively cold near the wall due to the recirculation of fuel that also increases the pressure. Points 2 and 3 show two distinct temperature and water mole fraction peaks due to the combustion of the fuel air mixture aft of the primary fuel injectors. There is a large pressure rise at point 4 due to the area contraction at the end of the cavity flameholder. Point 5 passes through the fuel stream as it mixes with air. The two large dips in temperature are due to the cold fuel. Much of the fuel has been heated by point 6, but the dips due to the fuel stream are visible through point 7. Points 5 through 11 show a gradual decrease in pressure as the combustion gases expand out of the nozzle. Temperature holds fairly steady, balanced by the expansion and heat addition from burning fuel.

5.1.1 Comparison with Discrete Ordinates Method

The profiles shown in Figure 5.1 are used as inputs for the IMC and DOM one dimensional simulations. In addition to being steady state, the medium is considered to be in equilibrium, which means that the medium does not change due to radiative effects. Radiation simulations model the radiative heat flux throughout the domain, but not the changes in the medium due to radiative heat flux. If the response of the flowfield to radiative thermal transport is desired, then the radiative heat flux solution can be coupled with the flowfield solution. Furthermore, the temporal dependence of radiative transport is neglected as significant changes in temperature of the medium are small, and occur on time scales much longer than radiative transport[13]. Wall
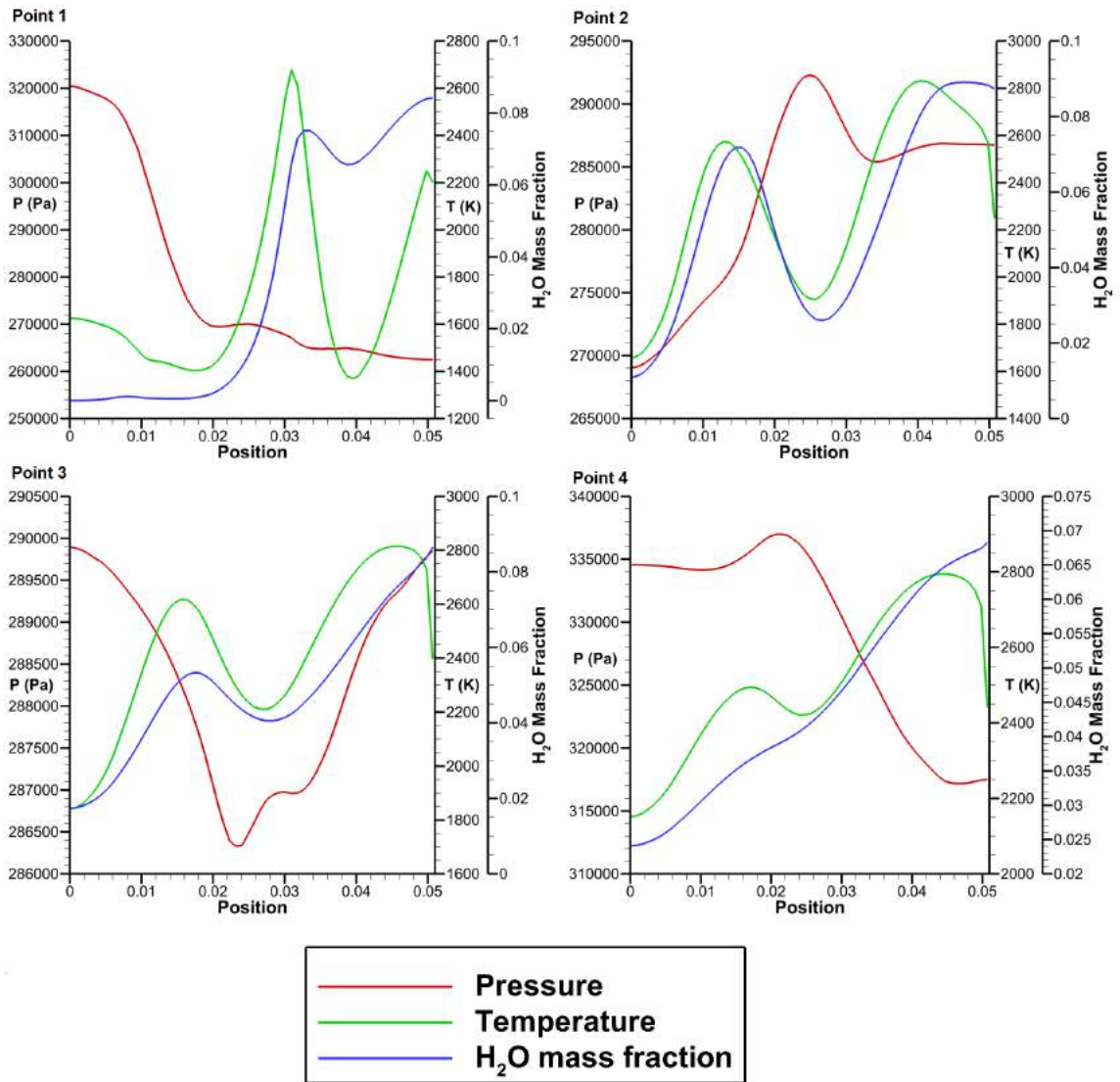
Figure 5.2: Temperature, pressure, and water vapor mass fraction profiles for points 1-4
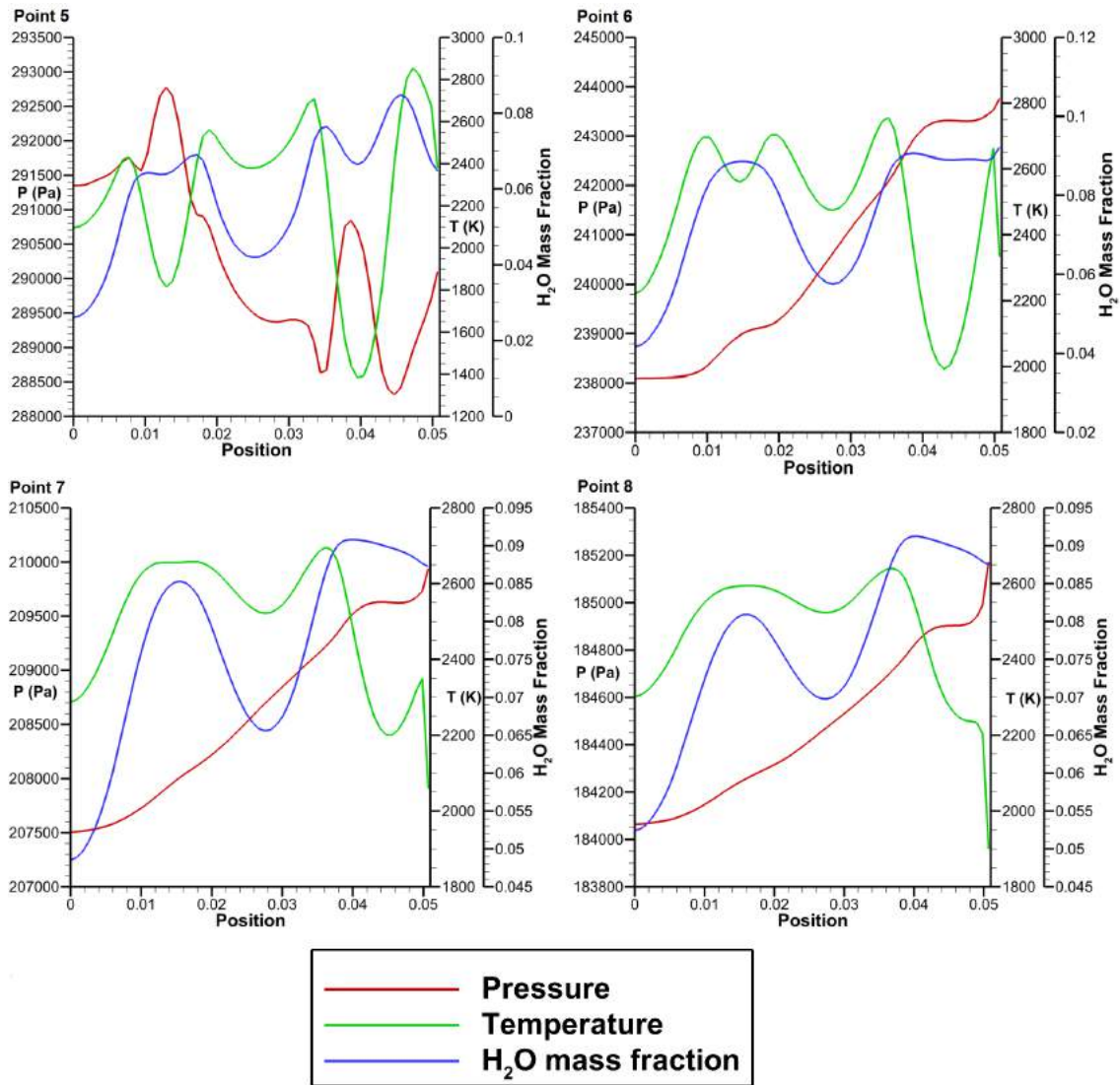
Figure 5.3: Temperature, pressure, and water vapor mass fraction profiles for points 5-8
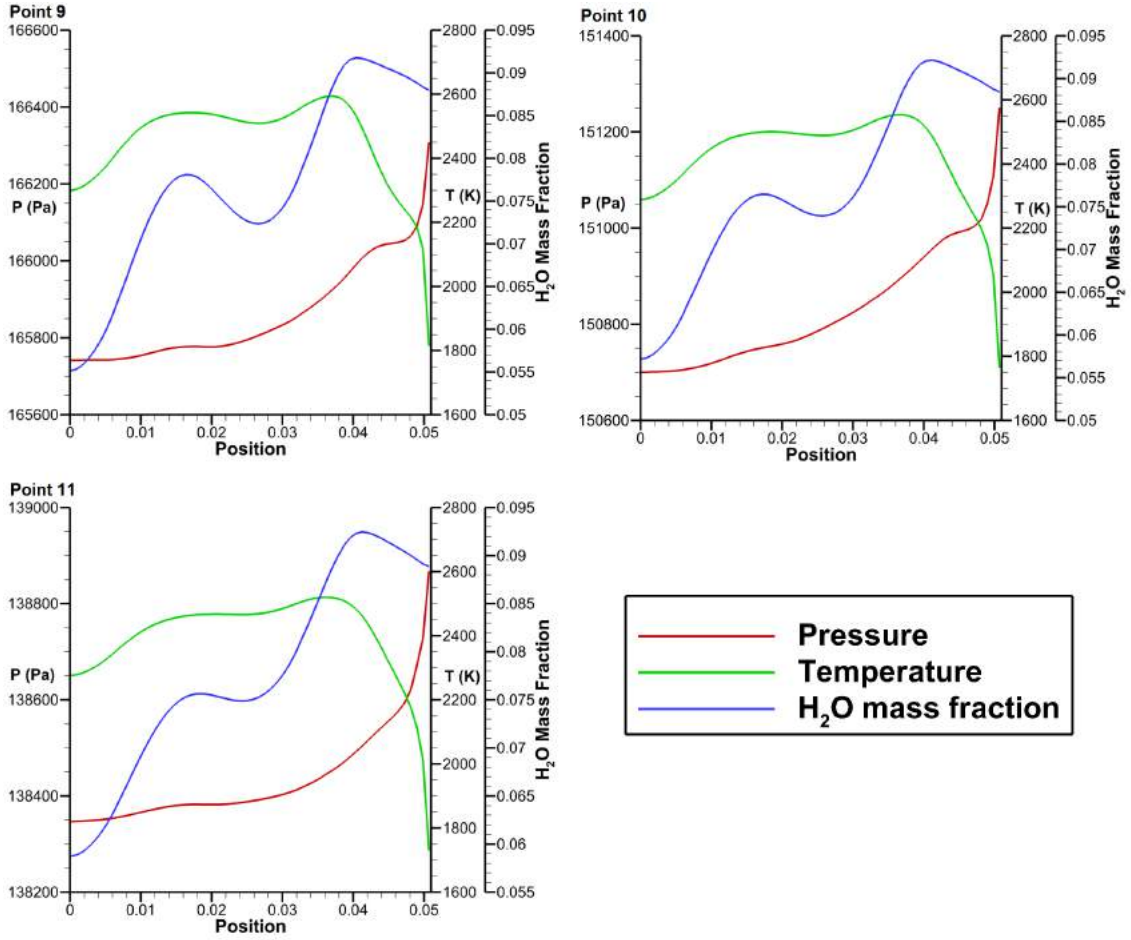
Figure 5.4: Temperature, pressure, and water vapor mass fraction profiles for points 9-11

radiative heat fluxes in simulations including these effects and using small time steps are found converge to an equilibrium state that is within one percent of simulations using a single time step large enough to ensure virtually all particles are terminated.

For HIFiRE-2, the flowfield is turbulent, which means that the flowfield properties at any given time are fluctuating, which in turn cause fluctuations in the absorption coefficient of the medium. The influence of these fluctuations on the radiation solution depends on the problem. When the medium can be considered transparent to thermal radiation on the scale of large scale turbulence structures, fluctuations other than the emission term can be neglected[41]. Duan shows that when the ratio of radiative heat flux to the turbulence time scale and the total enthalpy of the flow is small, the effects of turbulent fluctuations on the radiation solution is small, as well as influence of radiation on turbulence modeling[16]. For HIFiRE-2, the radiative heat flux is much smaller than the convective heat flux in most areas, but can be relevant in the flameholder cavity. Assuming that the turbulence-radiation interactions are small, the radiation simulation can be made independent of the CFD simulation with the radiative heat flux appearing as an energy source term in the CFD simulation.

Figures 5.5 and 5.7 show the spectrally resolved heat flux calculated by IMC and the DOM. While the magnitudes vary between the points considered, the character of the plots in Figure 5.5 are qualitatively very similar. This shows that, for the HIFiRE-2 combustion environment, the scale of absorption and emission changes little over the spectrum when considering only the radiation of water vapor. Additionally, the spectrally resolved heat fluxes from the DOM simulations show only subtle differences with IMC results in most of the plots throughout the spectral domain. The lower temperatures at Point 1 result in the lower overall magnitude of the heat flux results when compared to the other points. Table 5.2 shows the values of total radiative heat flux from the DOM and IMC simulations as well as the quantitative difference between the two solutions.
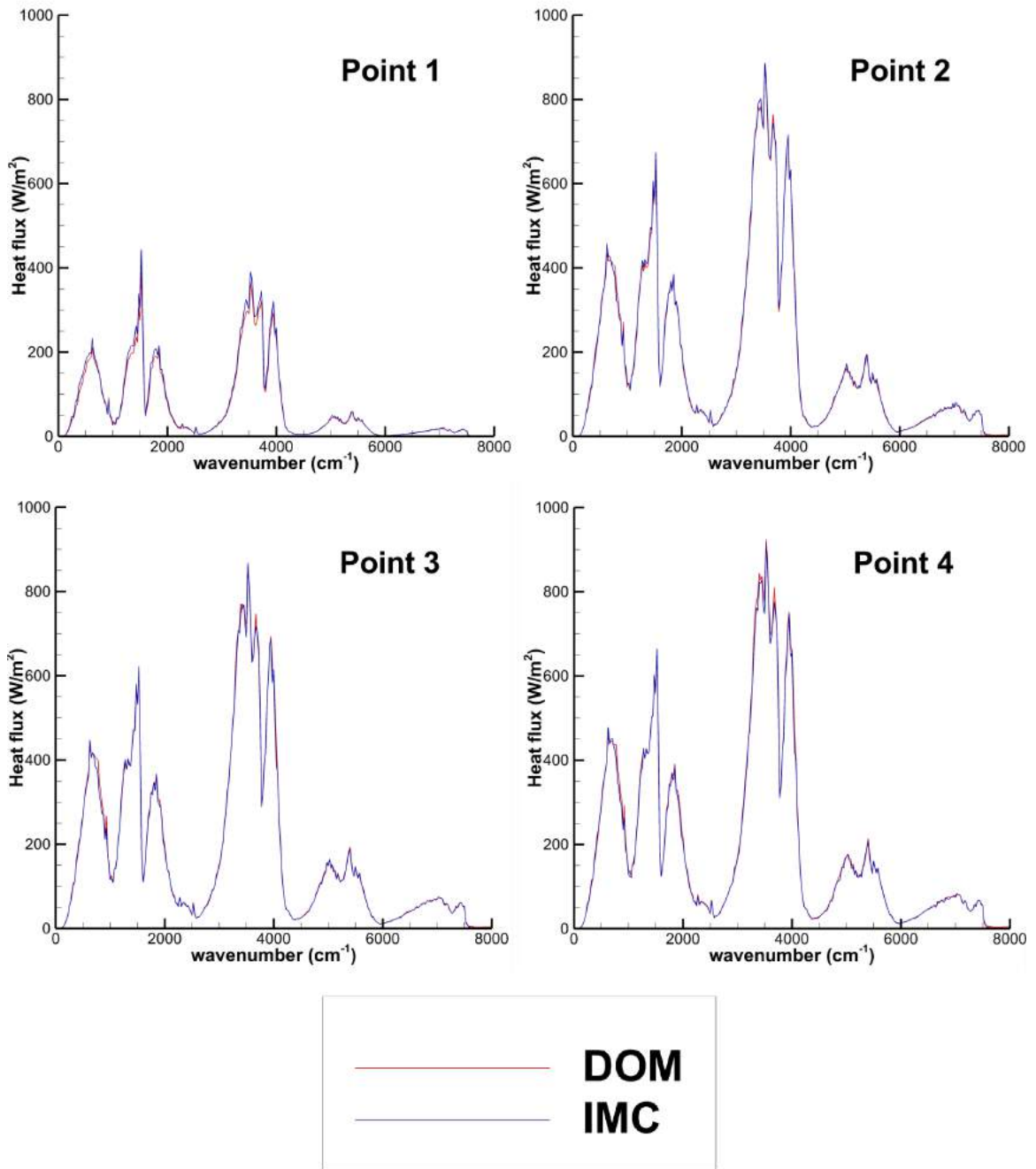
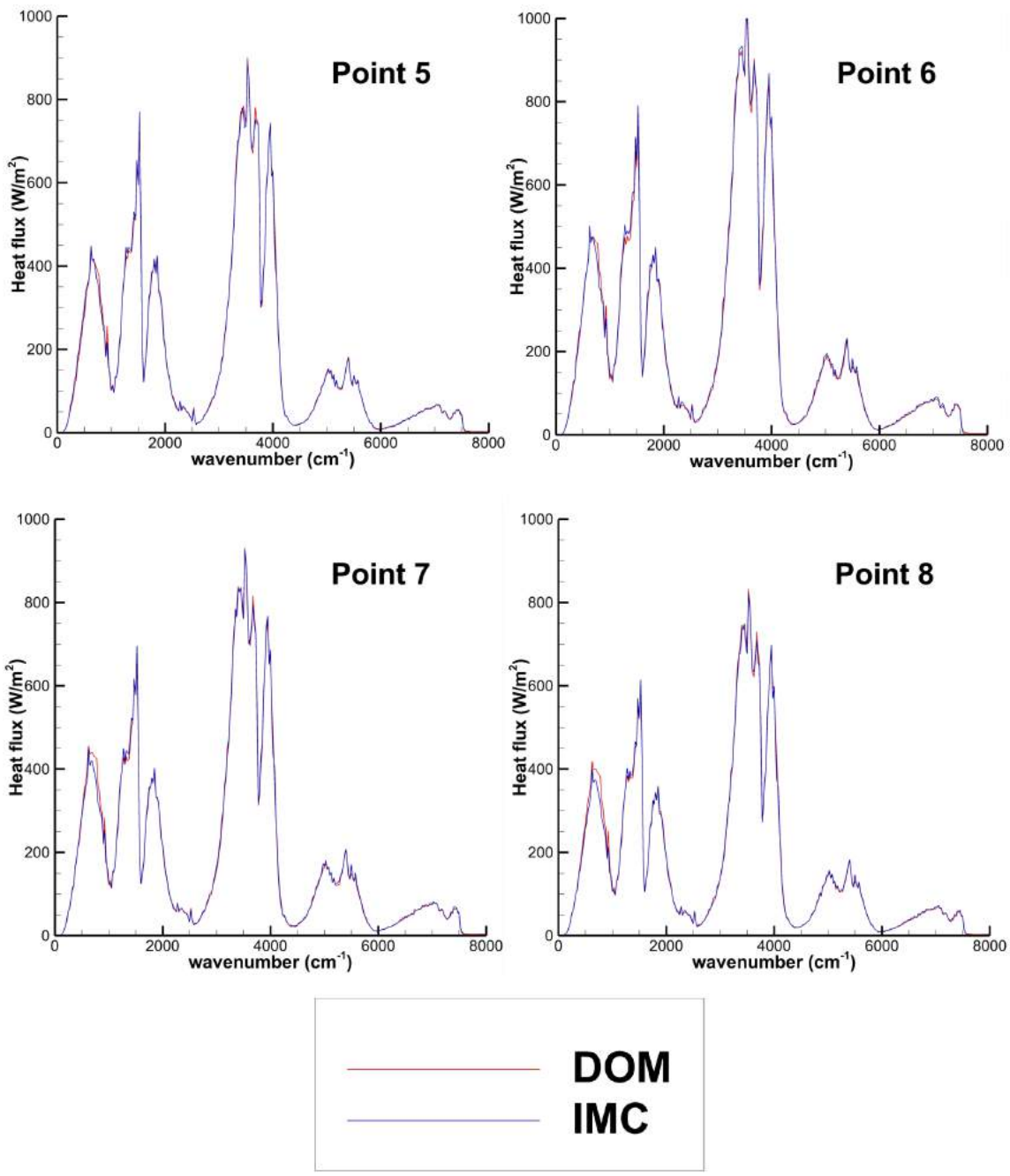Figure 5.5: Spectral radiative heat flux from IMC and DOM for points 1-4

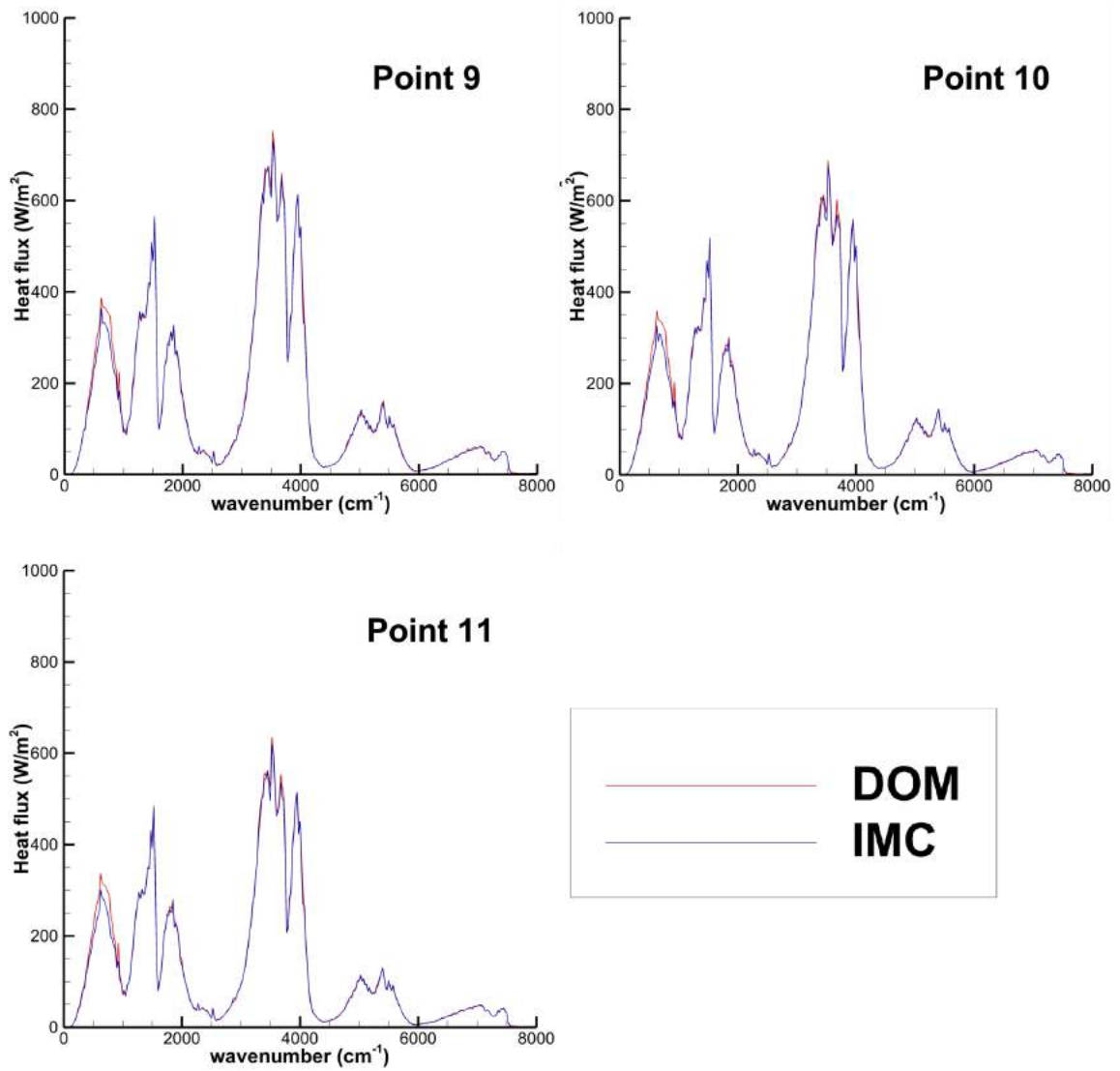Figure 5.6: Spectral radiative heat flux from IMC and DOM for points 5-8

Figure 5.7: Spectral radiative heat flux from IMC and DOM for points 9-11

	Radiative Heat flux		
Point	DOM	IMC	Relative difference (%)
1	43300	46200	6.31%
2	115000	116000	0.93%
3	113000	111000	-1.21%
4	123000	120000	-2.33%
5	113000	113000	-0.26%
6	134000	136000	1.36%
7	121000	121000	0.054%
8	108000	107000	-0.98%
9	96900	95300	-1.74%
10	87900	85800	-2.47%
11	80300	78100	-2.9%

Table 5.2: Total radiative heat flux from IMC and DOM $\left(\mathrm{W/m}^2\right)$

The quantitative epistemic error of the DOM is shown to be below seven percent for the selected points. Excluding the high error in the low radiative heat flux region, the error is below three percent for the selected points. Given that the epistemic error due to the transport methods is reduced for a one dimensional problem, the above errors can be attributed to the spectral model used in the DOM simulations. The uncertainty introduced by the parameters used by the LBL spectral model is shown in Section 5.3 to be an order of magnitude greater than the above errors. As such, the epistemic uncertainty introduced by the correlated-k spectral model used in the DOM simulations can be considered to be acceptable for modeling the absorption coefficients of water vapor for the HIFiRE-2 medium.

5.2   HIFiRE Three Dimensional Radiation Solutions

IMC solutions of radiative thermal transport of water vapor, on the three dimensional spatial grid shown in Figure 4.9, use 10 billion particles to populate the spatial and spectral domain. The medium is assumed to be in equilibrium and not affected by radiative thermal heat transfer. Boundaries at $z = 0$ and $y = 0$ are reflecting to account for domain symmetry, while all other boundaries are assumed to be com-

pletely absorbing. The spectral and angular dependence of absorption and reflectivity of the zirconia coated copper walls of the HIFiRE-2 scramjet combustion chamber are neglected in DOM and IMC simulations. Figure 5.8 shows the radiative thermal heat flux to the domain boundaries. Since radiative heat flux is proportional to water vapor concentration and pressure, as well as temperature to the fourth power, regions of high radiative heat flux follow areas that have relatively high values of these variables. The relatively cool air at the inlet produces little radiation compared to the hot combustion products contained in the cavity flameholder and nozzle. The radiative heat flux diminishes through the nozzle as the combustion products expand and cool.

Figure 5.9 shows the volumetric thermal radiative heat flux in the HIFiRE-2 scramjet, found using the IMC method. Negative values indicate regions that are emitting more energy than is absorbed, and positive values indicate cells that absorb more energy than is emitted. In this problem, nearly all cells have a negative volumetric heat flux. The relatively small size of the HIFiRE-2 scramjet results in the radiation traveling only a short distance to the walls, where it is absorbed. Since the particles only travel a short distance, the chance of absorption or scattering is small. Figure 5.9 shows that radiation is primarily emitted from the high temperature regions around the fuel injector plumes, in the cavity flameholder, and in the recirculation region at the primary fuel injector next to the boundary. More complete combustion in recirculation regions at the physical sidewall results in higher temperature regions and more thermal radiative emission. Additionally, majority of radiation is emitted from gases near the lower wall where the fuel injection ports are located and the resulting combustion products are concentrated. The cold gases near the inlet and immediately downstream of the fuel injection ports result in decreased emitted thermal radiation.

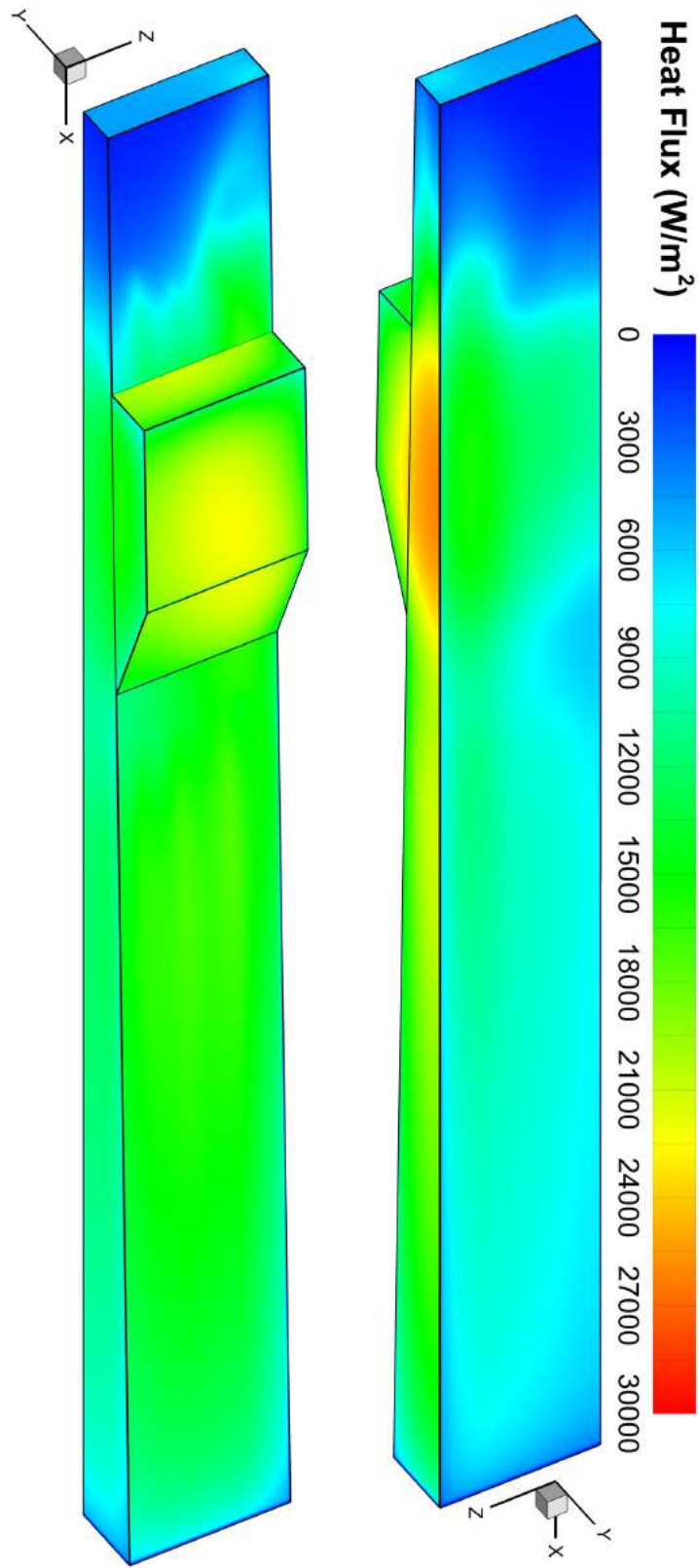Figure 5.10 shows the convective heat flux calculated by the CFD simulation.

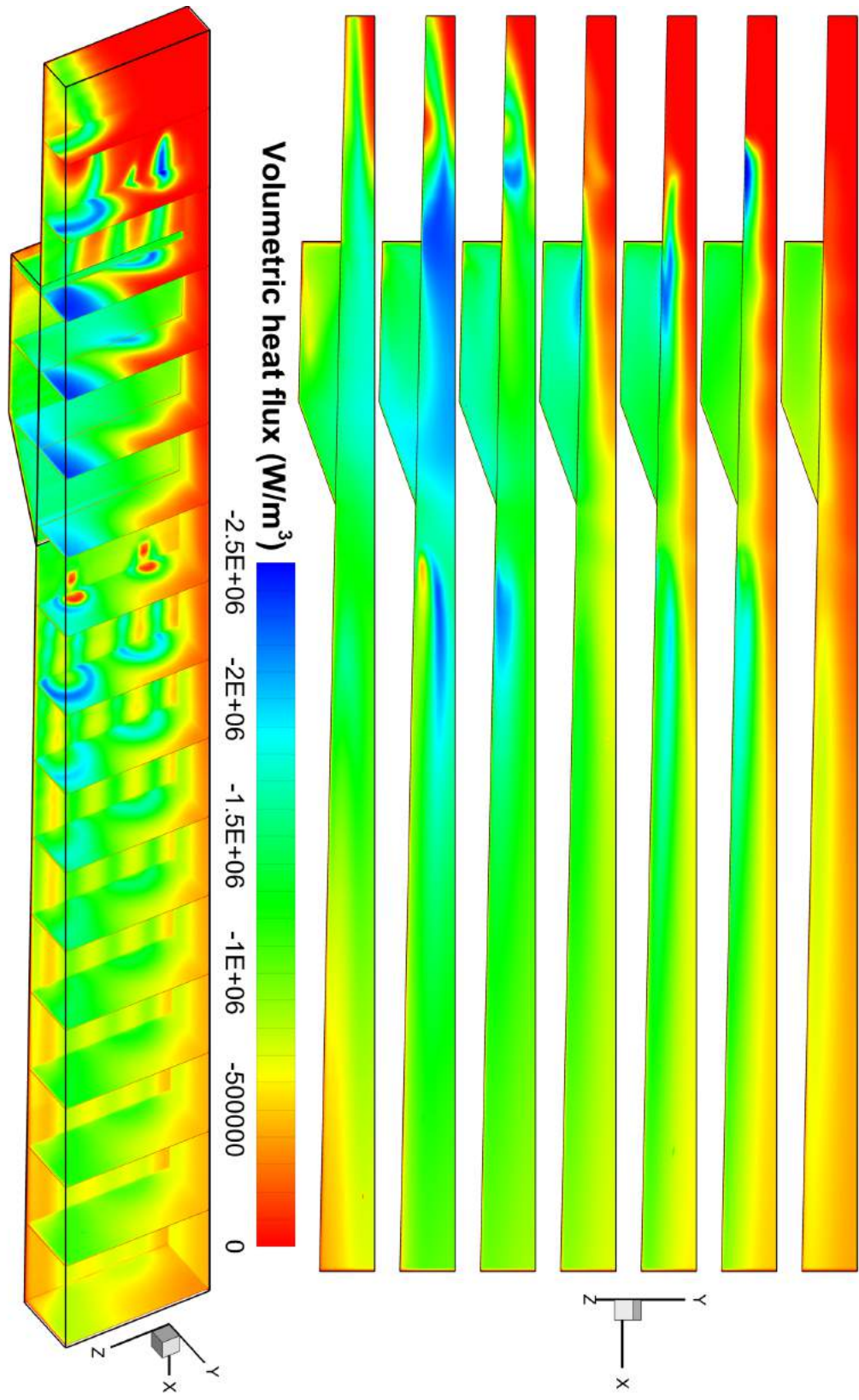Figure 5.8: IMC solution of radiative heat flux to walls

Figure 5.9: IMC solution of volumetric radiative heat flux

Injection of relatively cool fuel causes regions of relatively low heat flux near the fuel injection ports and directly downstream. This also causes an area of low heat flux in the cavity flameholder, which is due to recirculating cool fuel injected at the primary fuel injectors. Areas of high heat flux at the edges of the relatively cool fuel plumes are caused by combustion, as fuel from these plumes are starting to mix with the surrounding air. The spatial grid used by the CFD simulation has openings at the fuel injection ports, which result in a null heat flux at these ports.

Figure 5.11 shows the relative magnitude of the radiative heat flux absorbed by the walls to the convective heat flux found by the CFD simulation. While the radiative heat flux only considers contributions from water vapor, the convective heat flux includes contributions from all species. For the HIFiRE-2 scramjet, the radiative heat flux found by IMC calculations accounts for less than two percent of heat flux to the walls for the majority of the domain. Higher relative contributions of radiative thermal heat flux near the fuel injectors are due to lower convective heat flux in these regions from relatively cool fuel flowing into the system.

Figure 5.12 shows the absorbed volumetric heat flux. Comparing Figures 5.9 and 5.12 shows the difference in magnitude between radiative emission and absorption in the medium. Radiation emitted by the medium is evaluated deterministically and is dominant in Figure 5.9, while the absorbed radiative heat flux, shown in Figure 5.12, is determined in a stochastic manner. This leads to the statistical variance visible in Figure 5.12. While the radiative heat flux, shown in Figure 5.8, is also determined stochastically, there are nearly 11 times more volume elements than surface area elements for the spatial grid used in this simulation. This means that stochastic quantities in the volume are typically determined with nearly 11 times less information than stochastic quantities on the surface. Since statistical variance in the solution scales by $1/\sqrt{\#\,particles}$, the typical variance of stochastic quantities in the volume is typically over 3 times higher than on the surface.
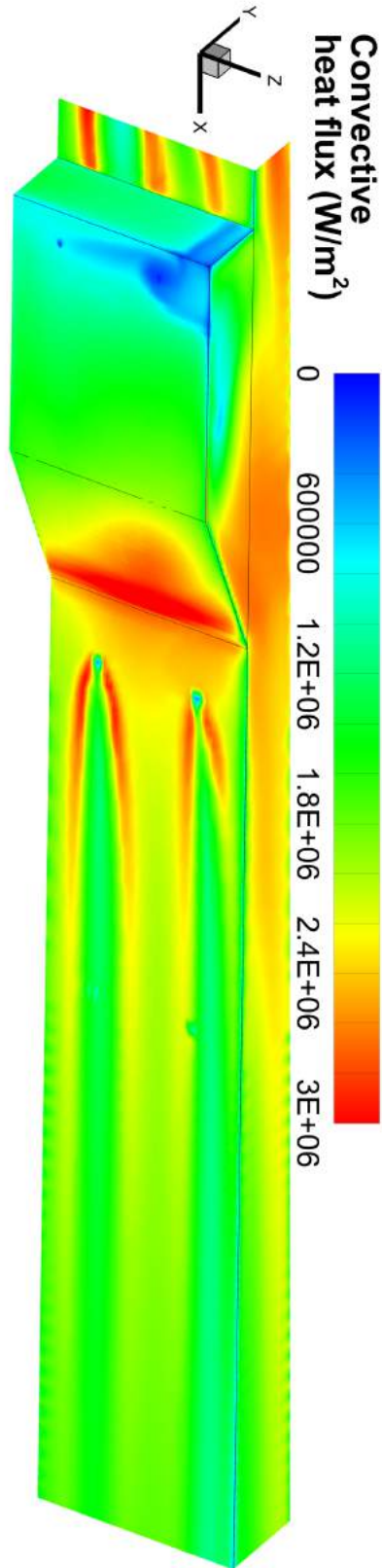
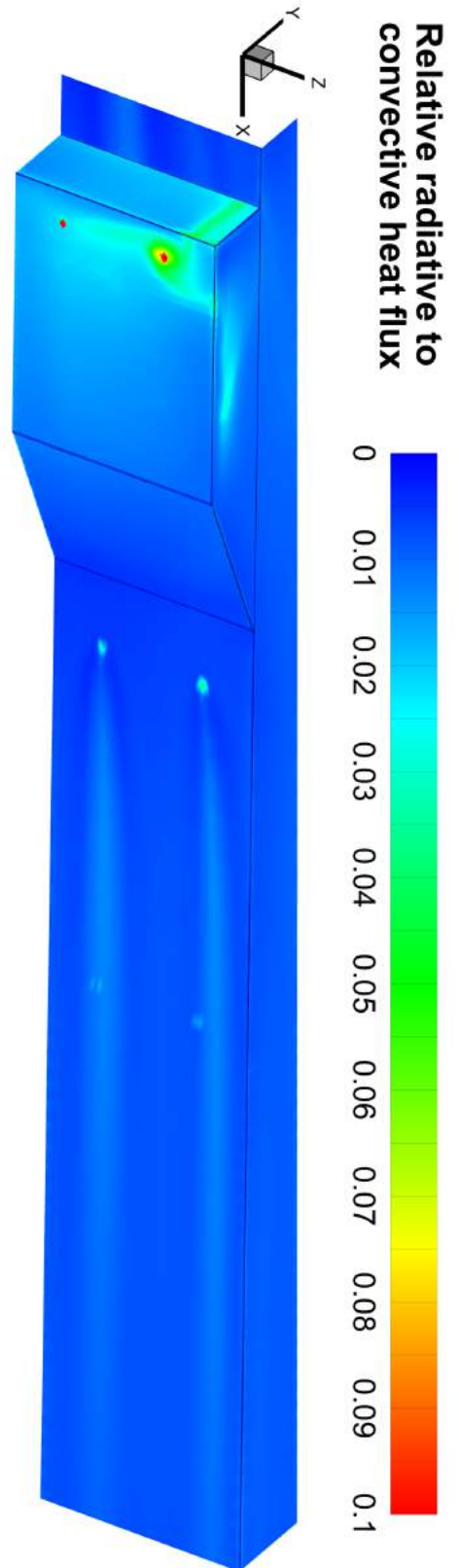Figure 5.10: CFD solution of convective heat flux

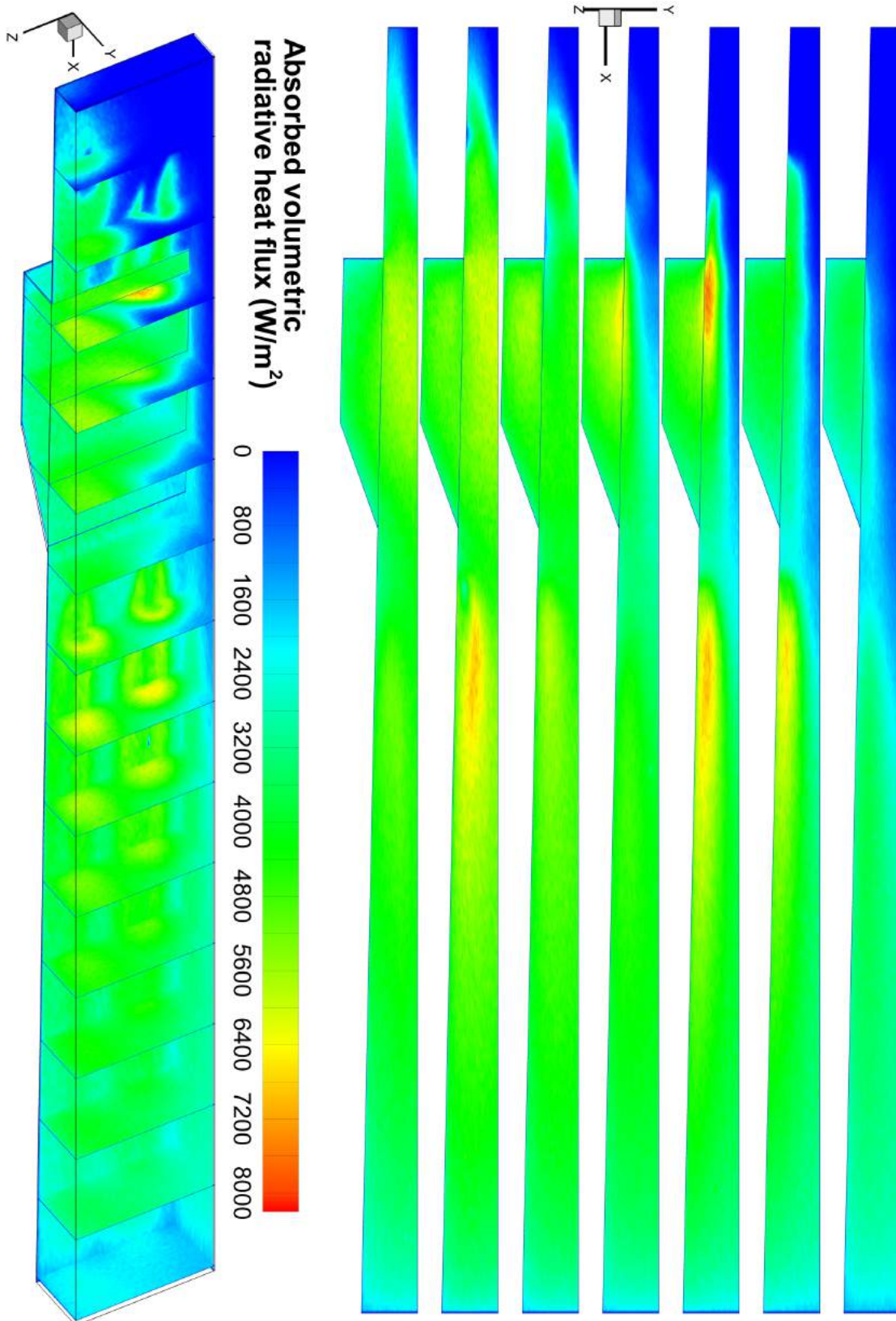Figure 5.11: Relative magnitude of radiative heat flux to convective heat flux

Figure 5.12: IMC solution of absorbed volumetric radiative heat flux

To quantify the statistical variance of the radiative heat flux, it is necessary to generate a sufficiently large sample of solutions. The statistical variance is quantified using the standard deviation of the solution for each value of radiative heat flux in the system. Given the large storage size of the solutions, the following numerically stable one pass algorithm is used so that solutions may be discarded once the contribution of each radiative heat flux solution to the cumulative solution variance is determined *Chan et al.* [7],

$$\bar{x}_n = \bar{x}_{n-1} + \frac{x_n - \bar{x}_{n-1}}{n}, \tag{5.1}$$

$$S_n = S_{n-1} + (x_n - \bar{x}_{n-1})(x_n - \bar{x}_n), \tag{5.2}$$

$$\sigma^2 = \frac{S_n}{n-1}, \tag{5.3}$$

where $\bar{x}_n$ is the mean, n is the sample number, S_n is the sum of the squares of the differences from the mean, and σ is the standard deviation. Equations 5.1 to 5.3 are updated after each solution for each radiative heat flux value. One hundred simulations are used to calculate the standard deviation values and use 100 million particles each. The resulting standard deviation is used to find the 95% confidence variation bounds of the radiative heat flux of a 100 million particle simulation. Figure 5.13 shows the relative differences of the half range for these bounds to the mean radiative heat flux values in terms of percent. Variance in the bulk of the solution is found to be less than five percent for this case when using 100 million particles. Since variance decreases at a rate of the inverse of $\sqrt{\# particles}$, the statistical variance of the 10 billion particle simulations is considered to be below 0.5% for the bulk of the solution. This level of epistemic uncertainty is taken to be sufficient for the three dimensional simulations in this thesis. The discontinuity in statistical variance at the start and end of the flameholder cavity is due to an abrupt change in grid spacing, resulting in an abrupt change in cell surface area in these regions.
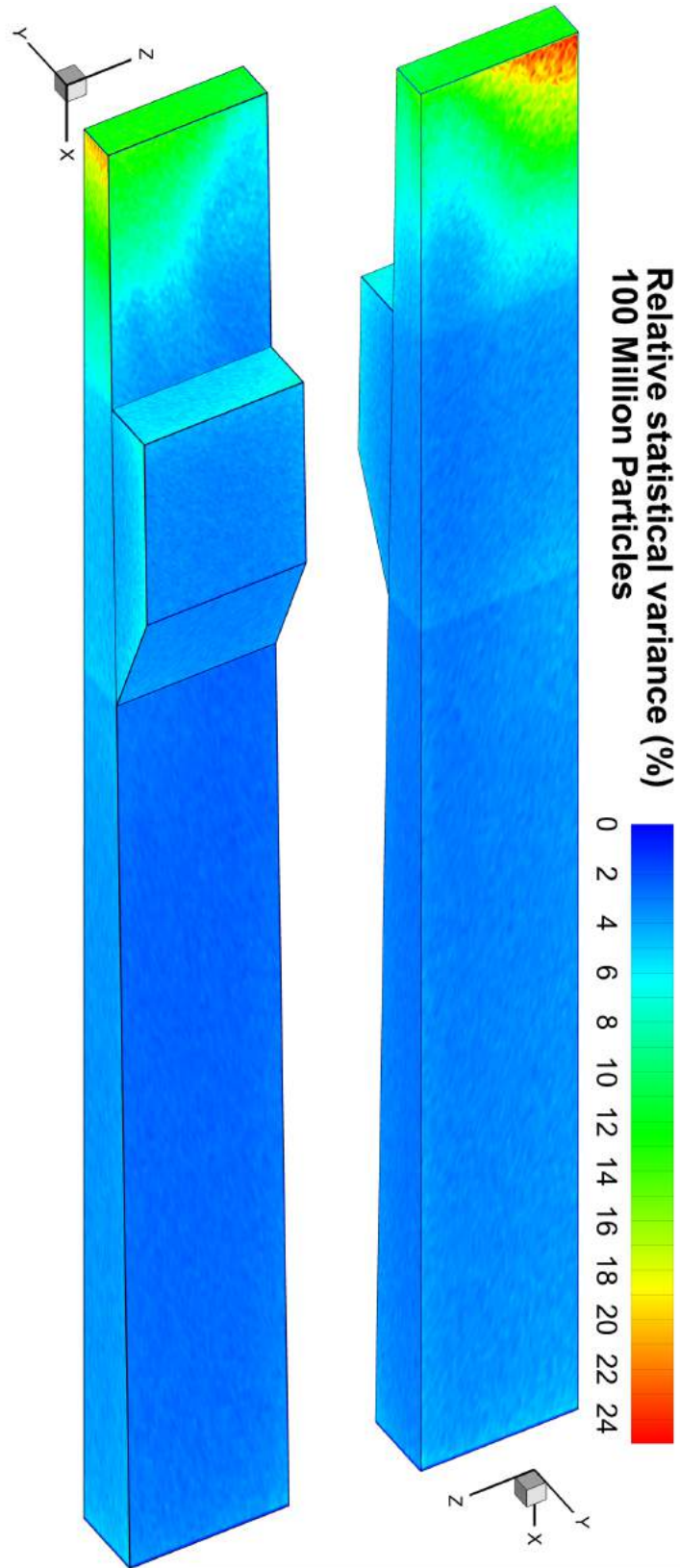
Figure 5.13: Percent of relative statistical variance of 100 million particle simulations

Figure 5.14 shows the number of particles absorbed, or reflected, by the boundaries. As expected, areas influenced by a few particles in Figure 5.14, correspond to areas of high statistical variance in Figure 5.13. Reducing statistical variance in these regions requires either increasing the total number of particles in the simulation, or statistically biasing particle propagation to distribute particles more evenly throughout the domain.

Figure 5.15 shows the scaling of the total simulation time, for a three dimensional IMC simulation using 10 million particles, as the number of processor cores utilized increases. The time to load the spectral database and spatial grid, and to write solution data is observed to be approximately 25 seconds, and is nearly independent of the number of processor cores used. In a typical one to ten billion particle simulation, the time for setup and file operations is negligible compared to the total computation time; however, for these 10 million particle simulations, the loading time becomes a significant portion of the total computation time as the number of processor cores increases. The calculation time scaling shown in Figure 5.15 excludes the setup and file input/output times to better reflect the scaling that would be observed in a typical simulation. The figure also shows an ideal scaling curve where the computation time is inversely proportional to the number of processor cores utilized. Scaling for the three dimensional IMC simulation diverges from the ideal scaling until 12 processor cores are utilized, and is close to ideal as more processor cores are utilized. All simulations utilize dual six core X5650 Intel processor nodes on the NYX computing cluster at the University of Michigan. The computational efficiency results shown in Figure 5.16 are calculated as,

$$\text{efficiency}\,(n) = \frac{t_1}{t_n\, n}$$

where t_x is the computation time when utilizing x processor cores, and n is the number
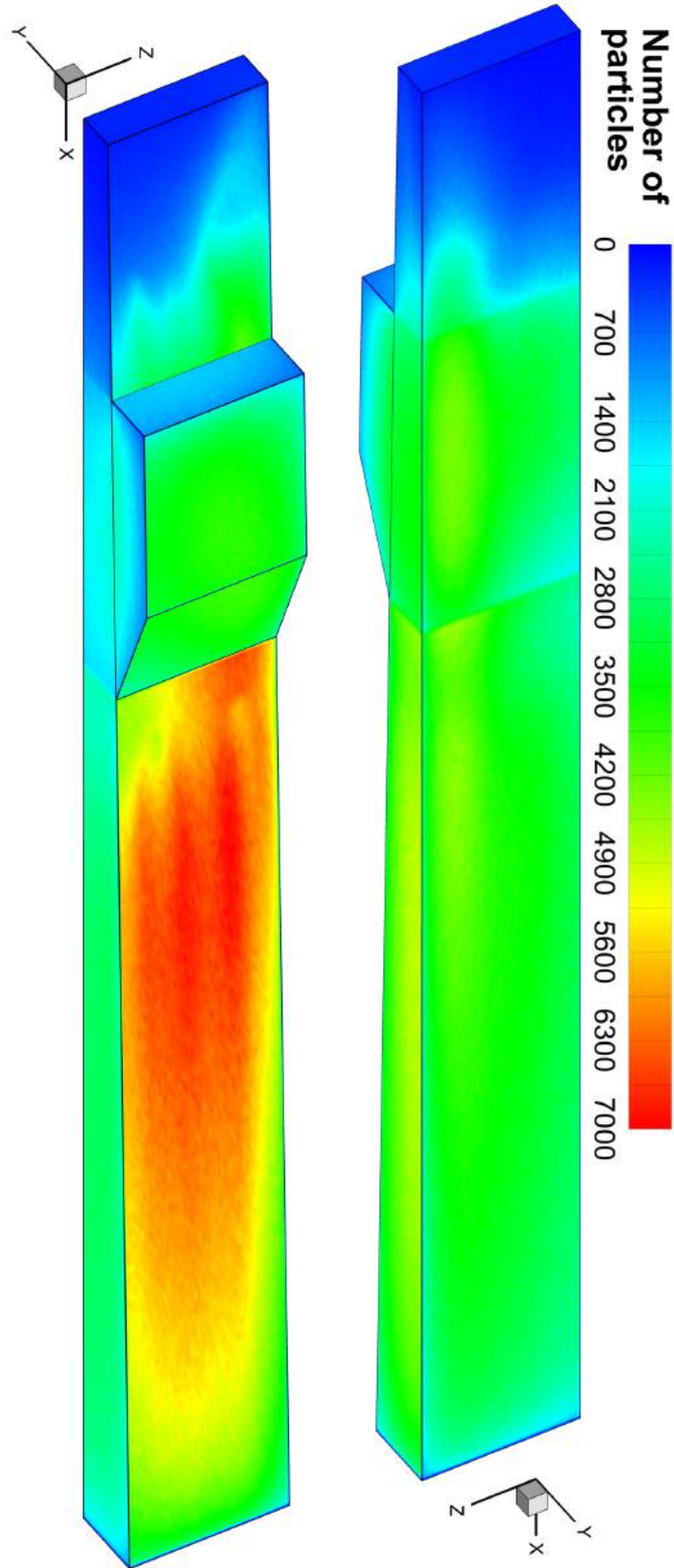
Figure 5.14: Number of boundary impacting particles in a 100 million particle simulation
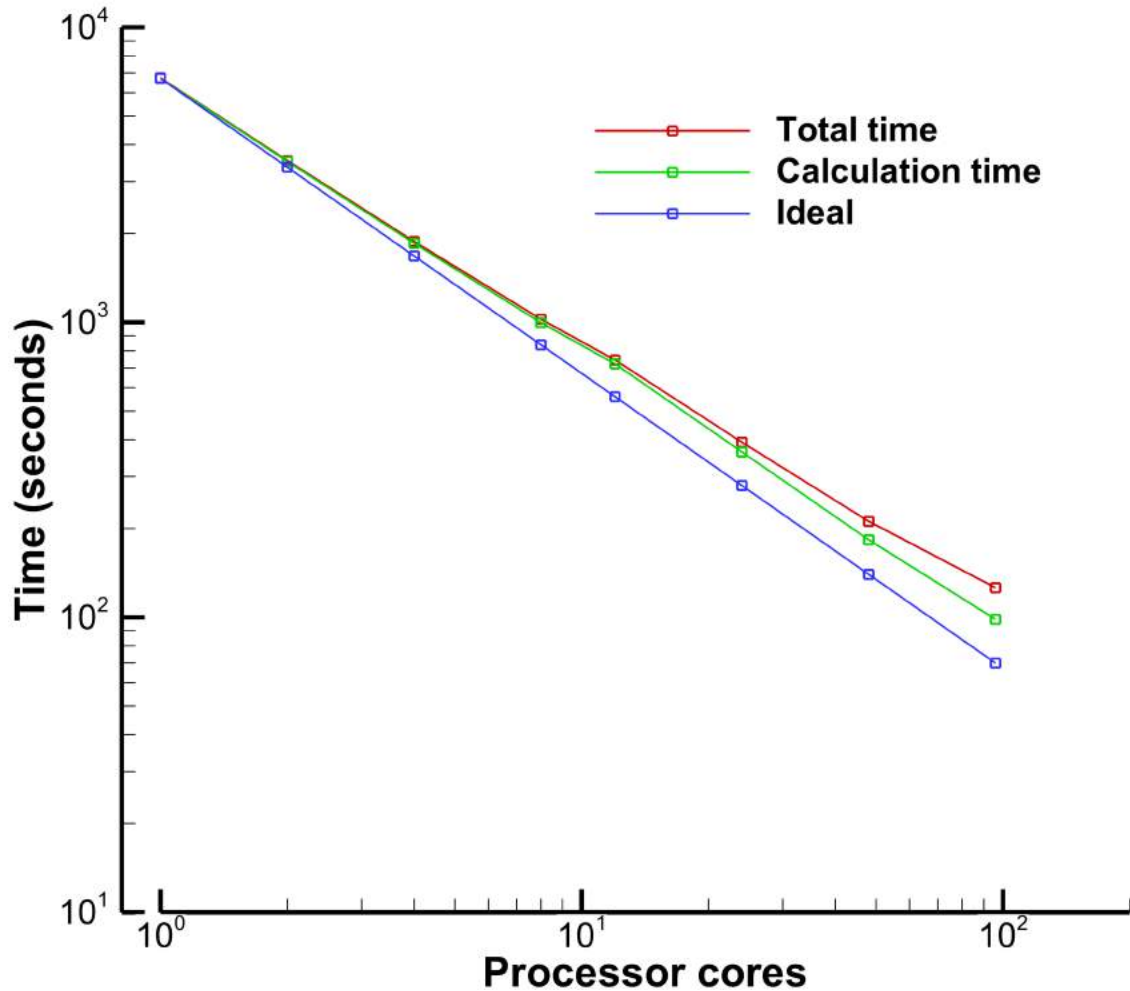
Figure 5.15: Computation time scaling on the number of processors utilized for 3D IMC simulations

of processors. It is uncertain why the computational efficiency rapidly decreases until the number of processors cores on a node is reached. Possibilities include performance limiting as the number of cores utilized in a processor increases to limit the thermal load of the processor, memory bandwidth saturation within a node, increased use of virtual memory, or increased utilization of processor cache. After the number of processor cores on a node is reached, the efficiency of the three dimensional IMC simulation is relatively constant.
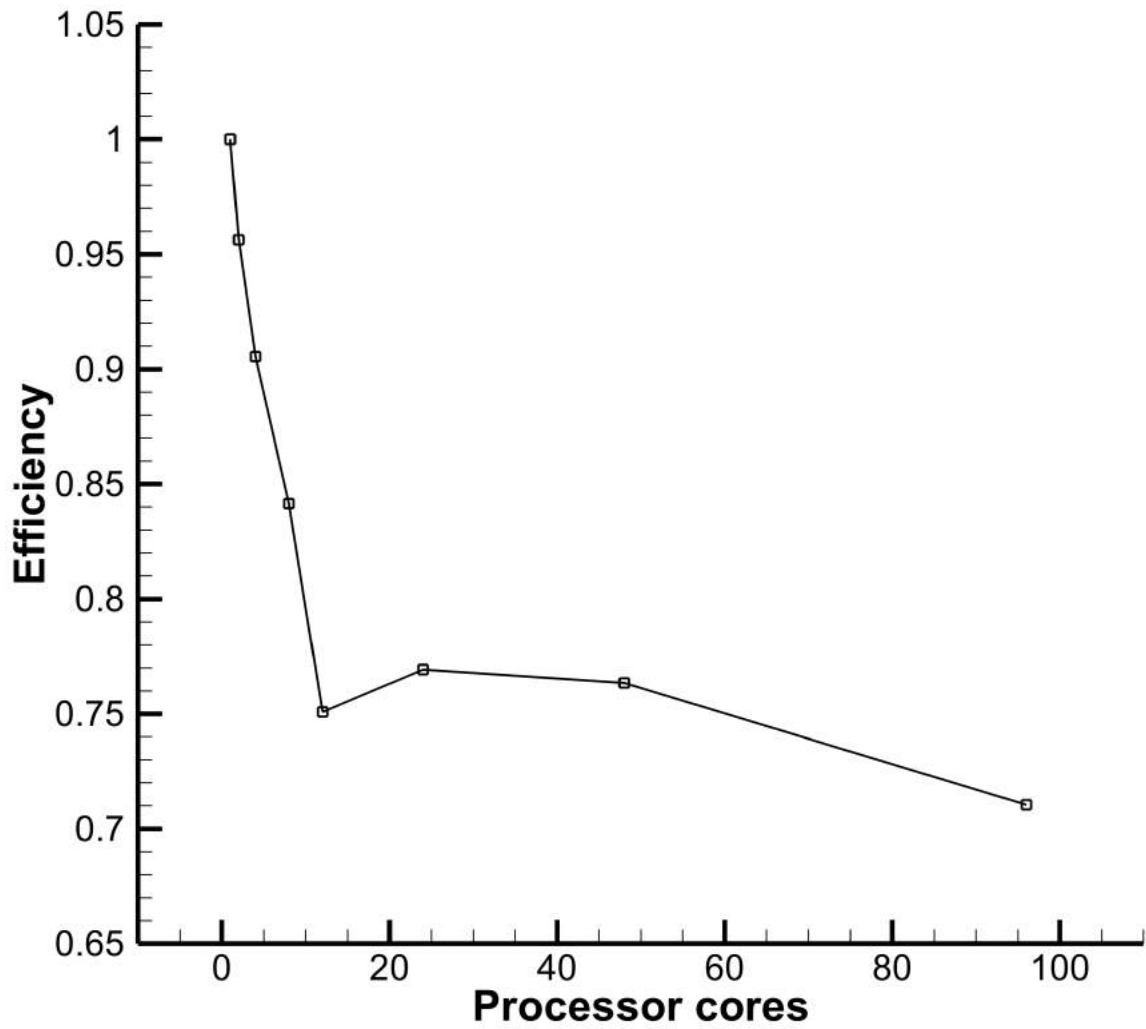
Figure 5.16: Parallel efficiency of IMC scaling for 3D solutions

5.2.1 Comparison with Discrete Ordinates Method

The DOM solution of the radiative thermal transport uses the same grid as the IMC solution. Angular space is divided into 80 ordinates using an S_8 quadrature scheme. The spectral method is a two point narrow band correlated-k spectral model, using 25cm^{-1} wide bands[13]. The spectral model used in the DOM solution relies on tables for each radiative species calculated at a single pressure and water mass fraction for six temperature points.

Figure 5.17 shows the radiative heat flux for water vapor calculated using the DOM. Qualitatively, the DOM solutions compare well to the IMC solutions shown in Figure 5.8, showing similar character and magnitudes. Figure 5.18 details the quantitative differences between the DOM and IMC solutions. Positive values indicate where the DOM calculates a higher radiative heat flux than the IMC solution, and negative values indicate where values found by the DOM are lower than the IMC solution. Figure 5.19 shows the absolute value of the relative difference between the DOM and IMC solutions.

The relatively high differences between the DOM and IMC solutions near the inlet are exaggerated due to the relatively low heat flux in that region. The DOM solution tends to under-predict heat flux in most of the high heat flux regions, with the exception of the upstream side of the cavity flameholder. The epistemic error of the DOM solutions is typically below 15% in areas with significant radiative heat flux.

5.3 Sensitivity Analysis of Radiative Heat Flux to Spectral Parameters

The magnitude of epistemic error in the DOM solutions is now put into the context of the epistemic uncertainty of the IMC solution. This section quantifies the

Figure 5.17: DOM solution of radiative heat flux

Figure 5.18: Difference in magnitude between DOM and IMC radiative heat flux solutions
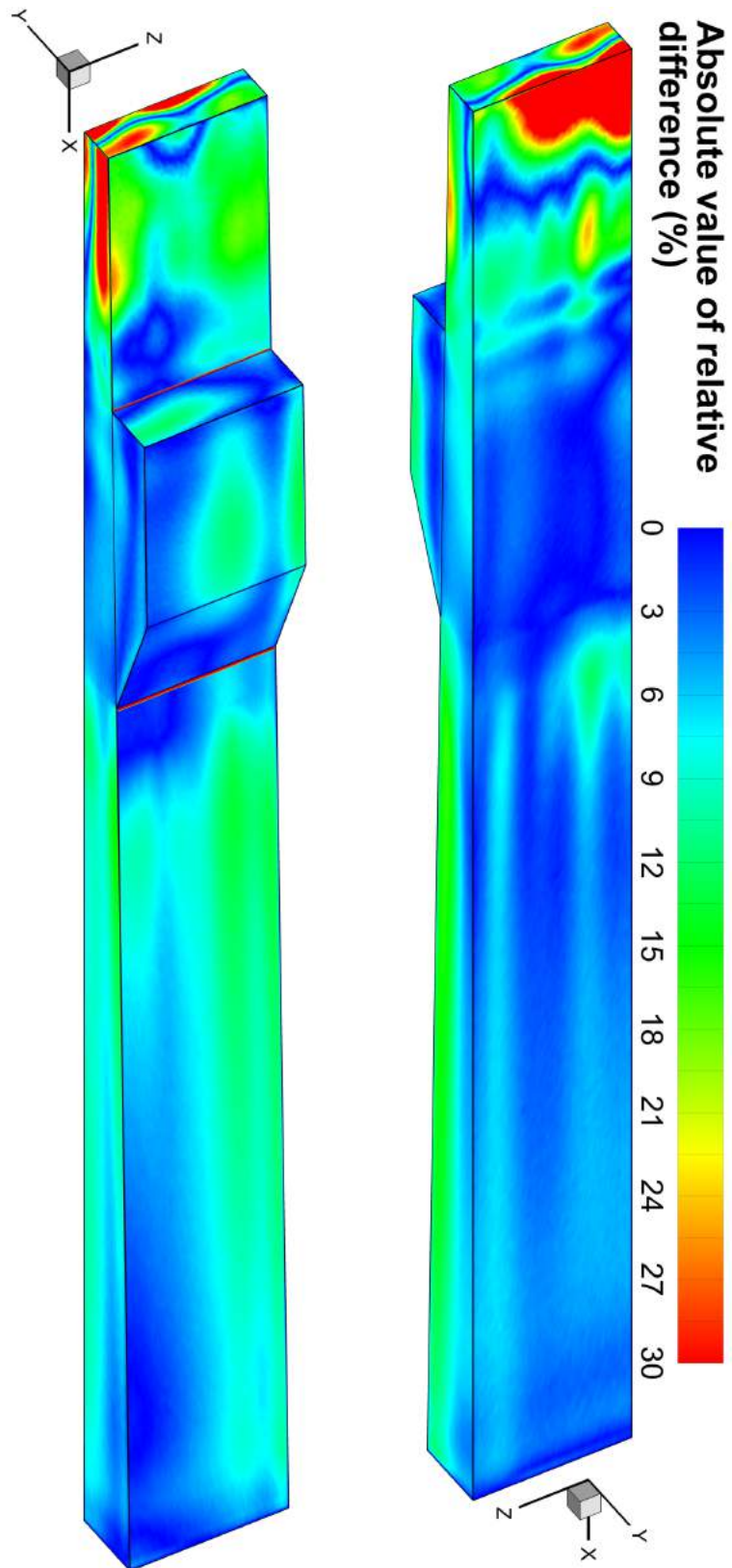
Figure 5.19: Absolute value of relative difference between the DOM and IMC radiative heat flux solutions

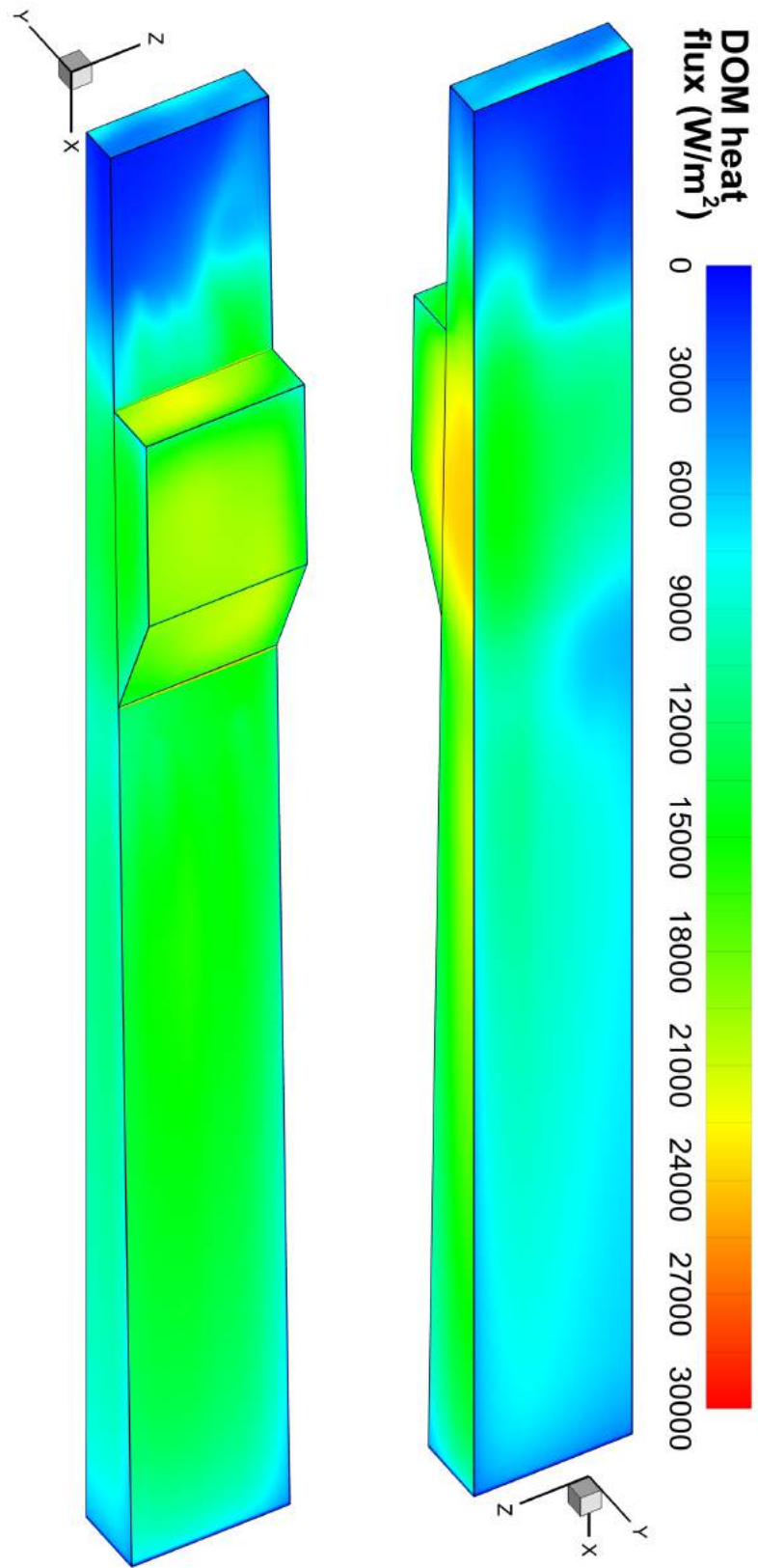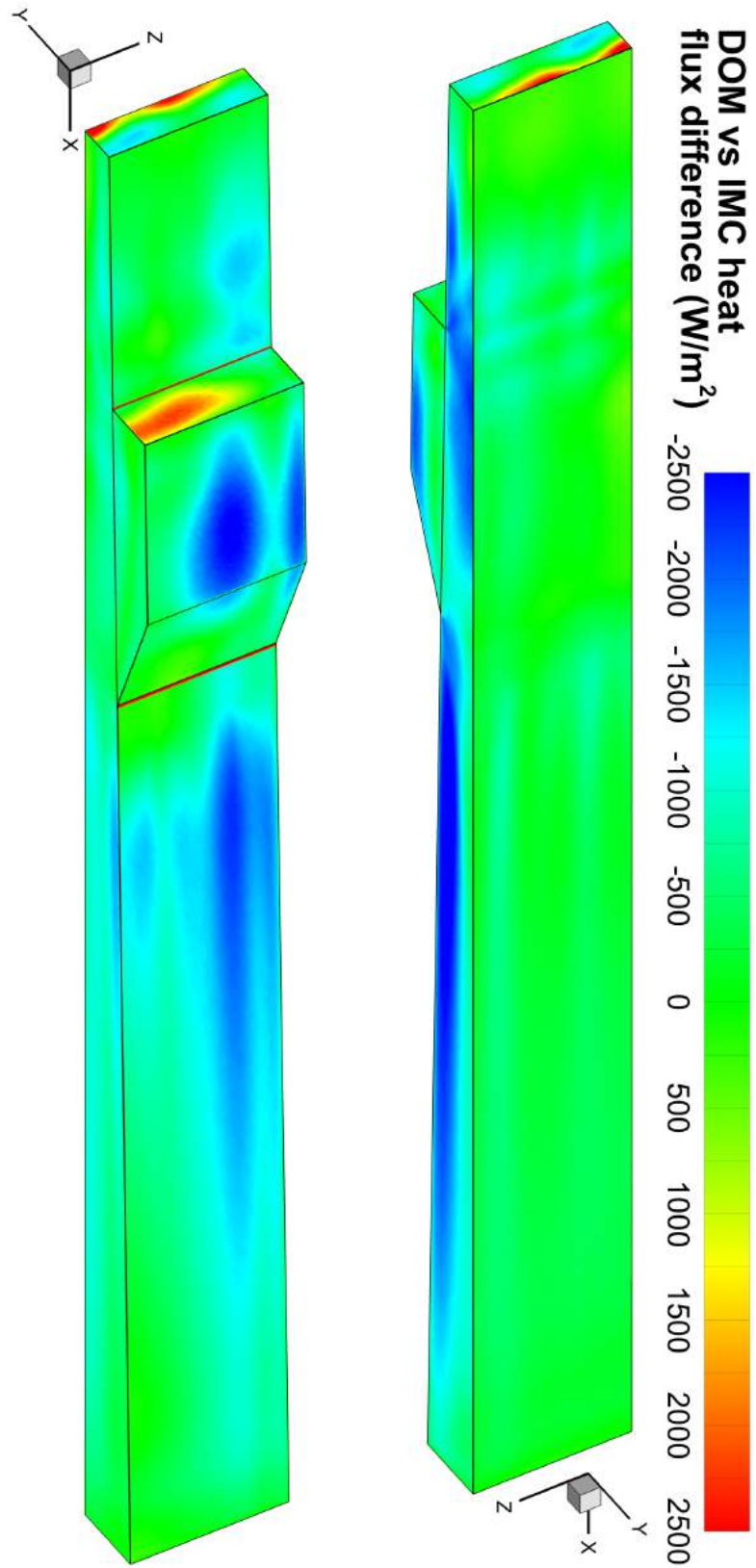epistemic uncertainty in the IMC solutions due to the uncertainty of parameters used in the calculation of the spectral properties. In the HITEMP 2010 database, there are uncertainties available for the parameters $S\left(T_{ref}\right)$, γ_{air}, γ_{self}, η_o, n, and $\delta\left(p_{ref}\right)$, which are used in Line by Line (LBL) calculations to calculate absorption coefficients. Since the absorption coefficient calculated for a specified wavenumber is dependent on contributions from several absorption lines, there is a possibility of correlations between uncertainties from separate lines. In other words, the influence of absorption line parameters from a single absorption line on the radiative heat flux can be influenced by uncertainties in other overlapping absorption lines. Therefore, it is insufficient to characterize the sensitivity of radiative heat flux to absorption line parameters based on a single absorption line. However, there are millions of absorption lines each with uncertain parameters. Generating a sufficient sample of a domain with millions of variables is impractical for even simple radiative thermal transport problems. To quantify the sensitivity of radiative heat flux to absorption line parameters, radiative heat flux is calculated for groups of 5 closely spaced lines. There are no specified probability distribution functions of parameter uncertainties in the HITEMP 2010 database, so parameters are assumed to vary uniformly within specified uncertainty bounds.

Fully sampling even this reduced domain of 30 variables using three values for each variable would require an impractical 3^{30} simulations. Instead, absorption line parameters are sampled using Latin Hypercube Sampling (LHS) with 1000 sample points for each line group. LHS promotes uniform sampling across the domain by discretizing each variable by the number of sample points[42]. Discretization of variables in this case is evenly spaced as the variables are assumed to have a uniform distribution. For this analysis, one point is sampled uniformly from each discrete bin for each variable. Each sample of a variable is randomly linked to one sample from the other variables, with each sample being used once. A LBL spectrum is computed

from the sampled lines for each sample of the absorption line parameters. These spectra are then used in one dimensional simulations to find the total radiative heat fluxes to the boundary, which are used as the quantity of interest for this analysis.

Not every absorption line in the HITEMP 2010 database has a known uncertainty for every parameter. To ensure that each parameter is considered for each randomly sampled group of absorption lines sampled, only entries with uncertainties for all six parameters are considered in this analysis. Once the radiative heat fluxes of the sample points are simulated and normalized, the correlation coefficients are found for parameter variations as

$$c_{xy} = \frac{E\left[(x - E(x))(y - E(y))\right]}{\sigma_x \sigma_y},$$

(5.4)

where the correlation coefficient, c_{xy}, is calculated for variables x and y; $E()$ is the expectation value function; and σ is the standard deviation. The correlation coefficient is equal to zero when the variables are linearly uncorrelated, and equal to ± 1 for perfect linear correlation.

An example of the spectral absorption coefficient of a line group is shown in Figure 5.20, where the expected values of the absorption line parameters listed in Table 5.3 are used. For this sample, lines one through four show strong overlap, while line 5 is relatively isolated.

Table 5.4 lists the correlation coefficients of the radiative heat flux to the boundary of each absorption line parameter varied for this group of lines. Based on this table, the uncertainty of the line intensity is the dominant influence on wall radiative heat flux. Since the correlation coefficient does not necessarily show non-linear correlations, it is necessary to also inspect the response to variable perturbations, or use more advanced correlation measures. Figure 5.21 shows the response of the normalized radiative heat flux to the boundary to the absorption line parameters.
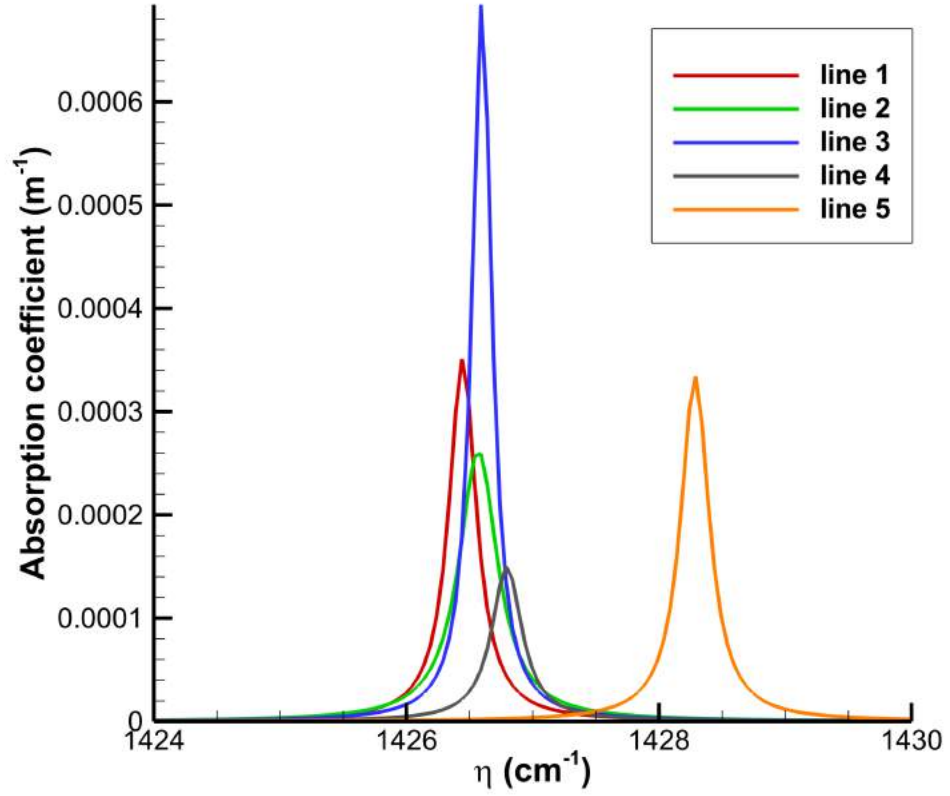
Figure 5.20: Spectral absorption coefficients of a group of absorption lines

Line	η_o $\left(\text{cm}^{-1}\right)$	$S\left(T_{ref}\right)$ $\left(\text{cm}^2/\text{molecules}\right)$	γ_{air} $\left(\text{cm}^{-1}/\text{atm}\right)$
1	1426.44±0.01	1.84E-23±2%	0.068±5%
2	1426.56±0.01	1.02E-24±10%	0.024±10%
3	1426.61±0.01	9.62E-23±2%	0.090±5%
4	1426.81±0.01	1.13E-24±10%	0.045±10%
5	1428.27±0.01	1.86E-21±2%	0.073±5%
Line	γ_{self} $\left(\text{cm}^{-1}/\text{atm}\right)$	$\delta\left(p_{ref}\right)$ $\left(\text{cm}^{-1}/\text{atm}\right)$	n
1	0.38±5%	0.0063±0.001	0.38±20%
2	0.19±10%	-0.0027±0.01	-0.25±20%
3	0.47±1%	-0.0018±0.001	0.72±20%
4	0.32±5%	-0.0068±0.01	0.24±20%
5	0.37±5%	0.0073±0.01	0.44±20%

Table 5.3: Varied absorption line parameters values and uncertainties of a group of absorption lines

Line	η_o	$S\left(T_{ref}\right)$	γ_{air}	γ_{self}	n	$\delta\left(p_{ref}\right)$
1	-0.0814	0.1347	0.0415	0.0110	0.0206	-0.0017
2	-0.0128	0.8486	0.0661	0.0447	-0.0763	-0.0188
3	-0.0576	0.1614	-0.0527	0.0076	0.0242	0.0139
4	-0.0046	0.4325	-0.0001	0.0645	0.0515	-0.0071
5	0.0282	0.1759	-0.0184	0.0049	0.0961	-0.0267

Table 5.4: Correlation coefficients of radiative wall heat flux to absorption line parameters

The line intensity parameter shows a significant linear correlation with wall radiative heat flux, in particular for line two. Figure 5.20 shows the magnitude of line two is relatively small, but the uncertainty of the line intensity parameter results in line two dominating the wall heat flux uncertainty. Based on Figure 5.21, the use of more advanced correlation measures is not necessary, as there is no significant correlation with the other line parameters. The above procedure and analysis is then applied to 40 other line groups, and each line group shows the same trends in heat flux response to variation of absorption line parameters, with strong correlations shown for the line intensity parameter.

Looking at equations 3.39a-3.39d, the line intensity is the line parameter that primarily influences the Planck mean absorption coefficient, and by extension, the magnitude of thermally emitted radiation. Section 5.2 shows that the medium is largely transparent to thermal radiation in the HIFiRE-2 scramjet. This means that only a relatively small portion of thermally emitted radiative heat flux is influenced by the absorption coefficient of the medium in this system. Given that the radiative thermal transport through the scramjet shows little absorption, it is reasonable to conclude that variation of absorption line parameters other than line intensity, have little influence on the radiative heat flux to the boundary. For systems in which absorption by the medium is high, the variation of line shapes could show more influence on thermal radiative transport.

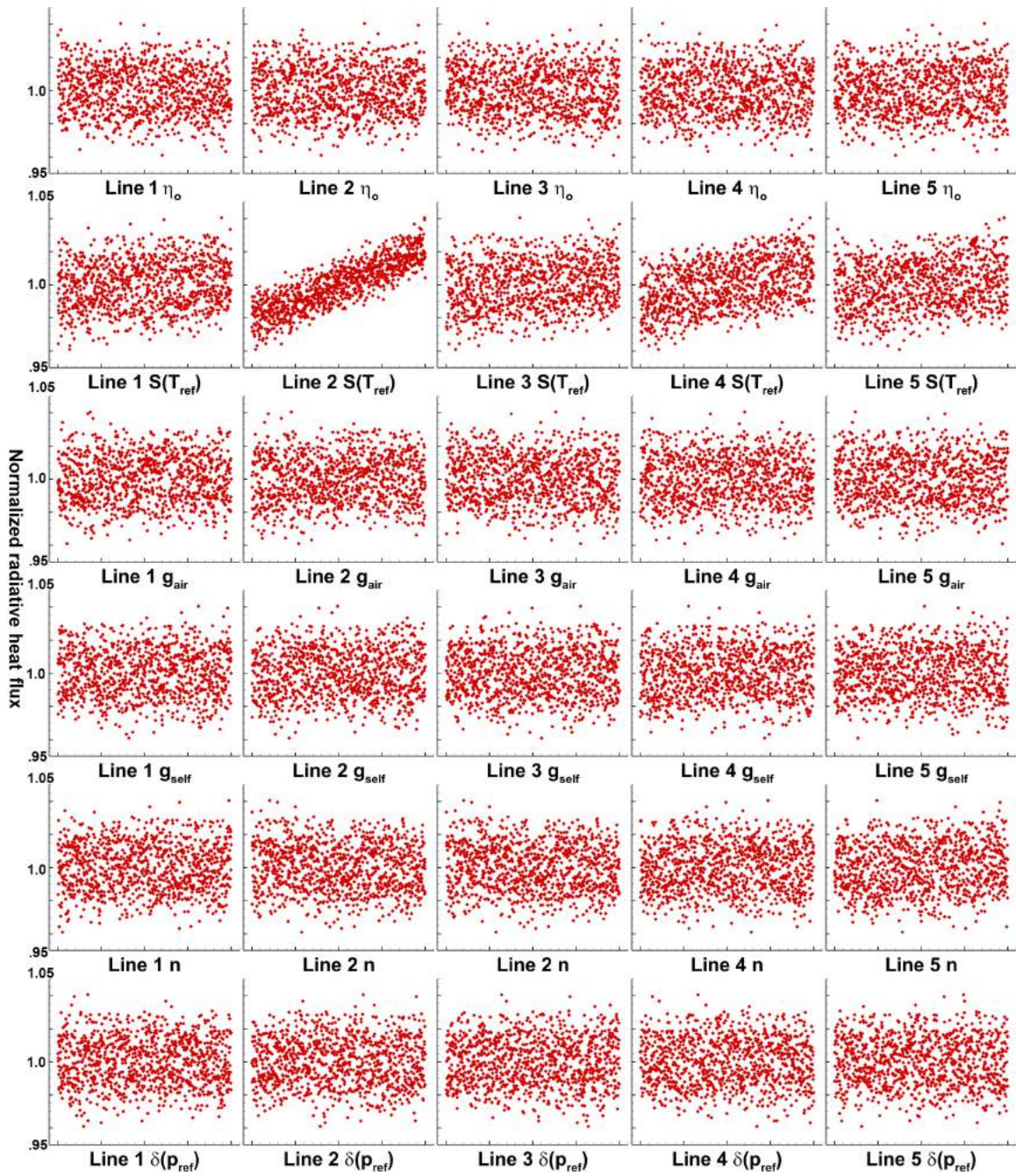Though the sensitivity analysis shows that the epistemic uncertainty of radiative

Figure 5.21: Example of normalized radiative heat flux response to parameter variation normalized from -1 to 1

heat flux, due to the uncertainty of absorption line parameters, can be quantified using only one parameter, the number of lines in the spectrum makes a sensitivity analysis of the full three dimensional HIFiRE-2 simulation impractical. To quantify the epistemic uncertainty in the three dimensional radiative thermal transport simulations, it is necessary to model the uncertainty of the radiative heat flux due to the uncertainty of the line intensities. Given the linear response of radiative heat flux to line intensity, the uncertainty of line intensity of each absorption line is weighted by the relative contribution of the line to the total spectral absorption coefficient. Applying this estimate to the one dimensional sensitivity analysis results in uncertainty estimates of the heat flux typically within three percent of two standard deviations of the sampled uncertainty.

The weighted uncertainty estimate is calculated using available uncertainties of line intensity in the HITEMP 2010 database for the 0-8000 cm^{-1} wavenumber range used in the IMC simulations in this thesis. Weights are calculated at one temperature, and stored in a table for later use in the IMC calculations. Figure 5.22 shows the resulting relative uncertainty over wavenumber, and an example of absorption coefficient. The modeled uncertainty tends to be lower in more absorbing regions, where stronger absorption line parameters are better characterized.

The modeled uncertainty is propagated through the domain by storing a separate energy for each particle that is the initial energy of that particle multiplied by the tabulated uncertainty at the wavenumber of the particle. Attenuation and deposition of this energy are treated the same as the particle's thermal radiative energy, but when deposited, this energy is stored separately in each spatial cell. At the end of the simulation, this energy is divided by the total deposited thermal radiative energy to estimate the uncertainty of the radiative heat flux of each location. Figure 5.23 shows the modeled epistemic uncertainty of the radiative heat flux due to the uncertainty of line intensity in the HITEMP 2010 database.
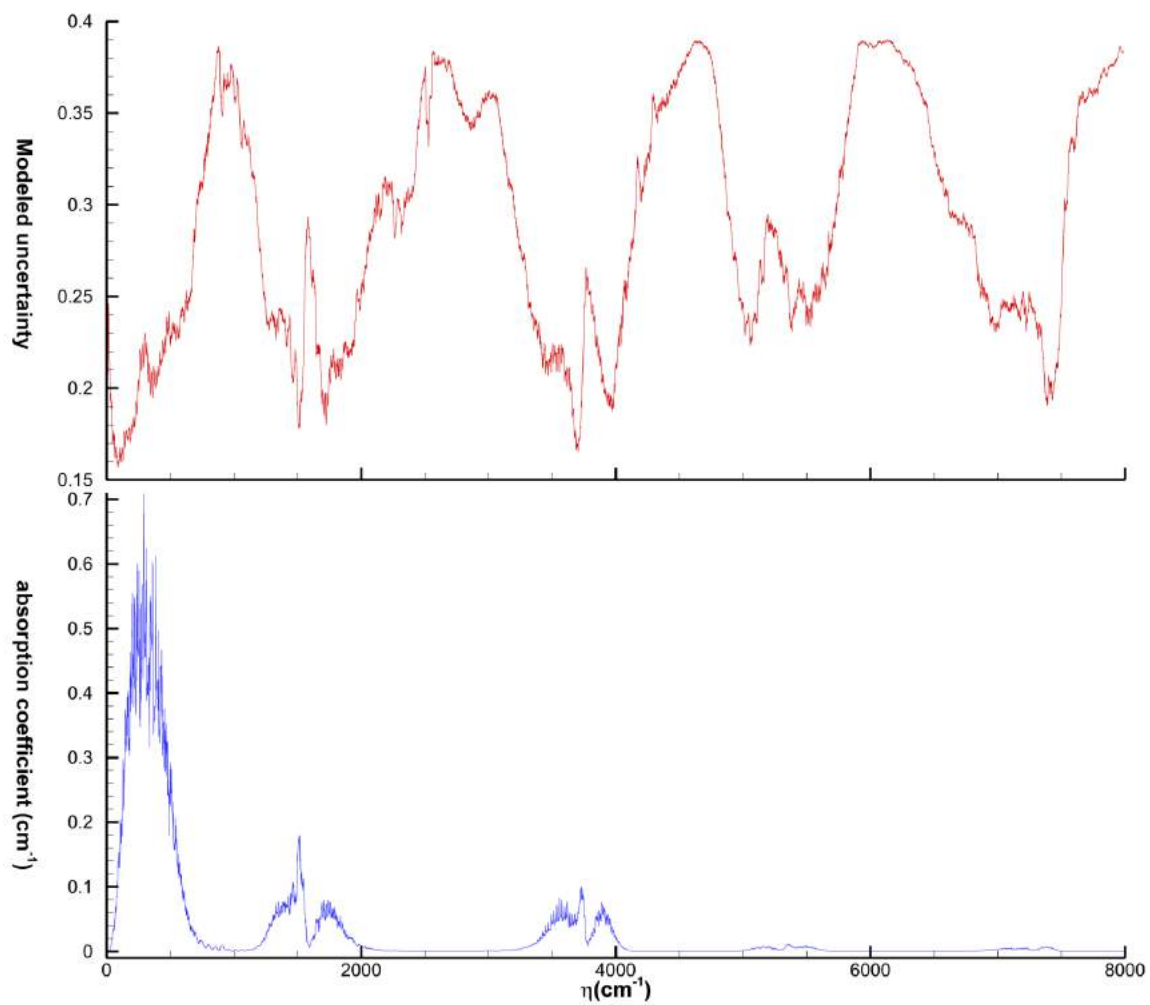
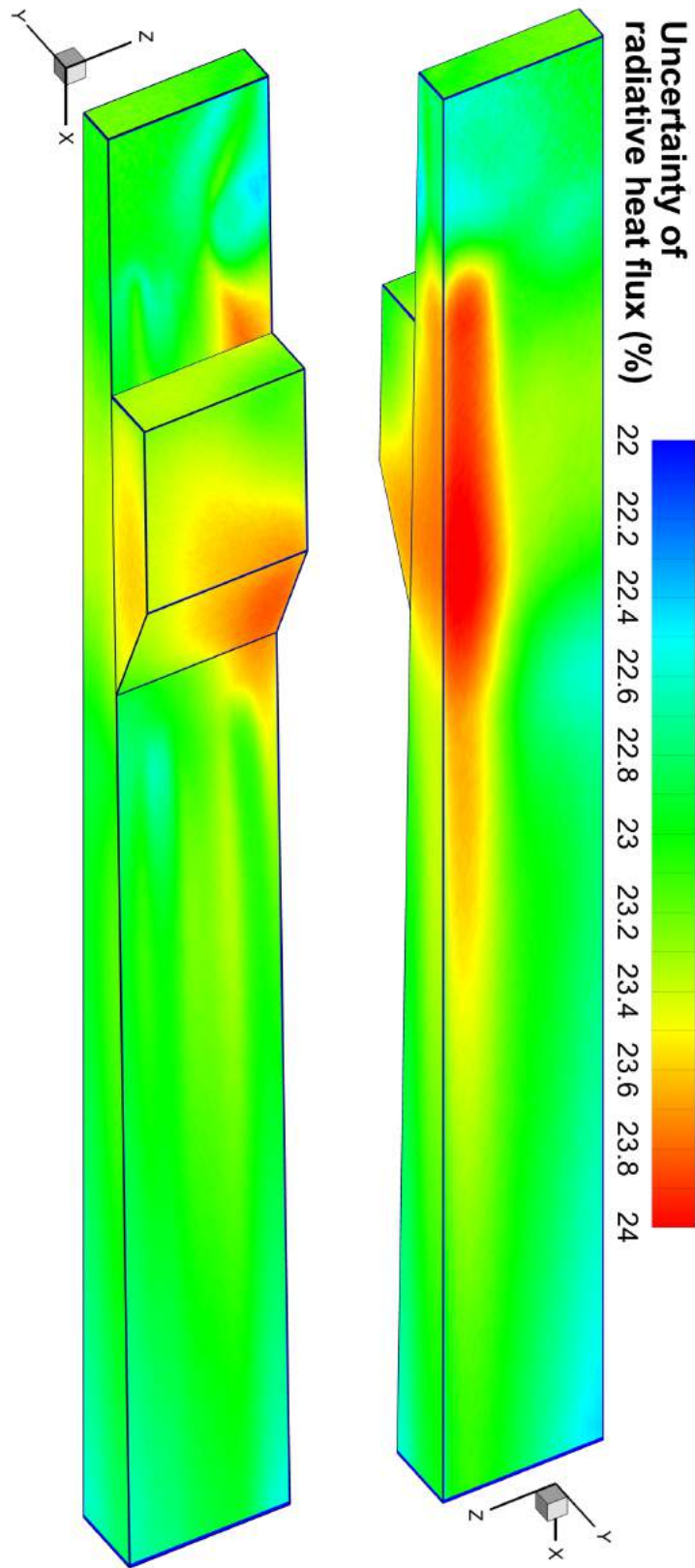Figure 5.22: Spectrally resolved relative uncertainty and absorption coefficient

Figure 5.23: Epistemic uncertainty of radiative heat flux predicted by model

The range of the modeled uncertainty is relatively narrow, indicating that the character of the spectrally resolved heat flux is fairly consistent throughout the domain. This conclusion is supported by the consistent character in the one dimensional calculations, shown in Figure 5.5, of spectrally resolved radiative heat flux. The magnitude of the heat flux relative uncertainty is consistent with the uncertainty of the absorption coefficient. The heat flux uncertainty can only be reduced by reductions of uncertainties of absorption line parameters.

5.4 Summary

Spectrally resolved radiative heat flux for results for water vapor are generated for one dimensional problems representing several points along the HIFiRE-2 scramjet combustion chamber. The contribution of radiative heat flux at the boundaries is found to be relatively small in most of the scramjet, compared to the convective heat flux. Comparison to DOM results shows epistemic errors on the order of three percent for the bulk of the combustion chamber, and over six percent in the colder region near the combustion chamber inlet. The radiative heat flux results for the three dimensional HIFiRE-2 scramjet combustor using IMC demonstrate that the statistical variance of these results are quantified as being below half a percent in the majority of the solution, and three percent near the inlet for the 10 billion particle simulation. A solution calculated from the DOM is compared to IMC results, and shows epistemic errors below 15% through the bulk of the combustion chamber with higher errors at the inlet. The sensitivity of radiative heat flux due to uncertainty of absorption line parameters in a one dimensional problem is quantified. A model based on this analysis is applied to the three dimensional simulation to model the epistemic uncertainty of the IMC results due to absorption line parameters. The epistemic uncertainty is found to be between 22 and 24 percent for a 95% confidence interval.

CHAPTER VI

Teleportation Correction

This chapter presents the results of the teleportation correction method applied to three test problems which are designed to show teleportation error. These results are compared to solutions obtained using the source tilting method to show the magnitude and behavior of the teleportation error, in these problems, when using this common method. The simulations in this chapter were conducted at the Lawrence Livermore National Laboratory using their KULL radiative hyrodynamic simulation code. The purpose of KULL is to simulate the physical processes inside inertial confinement fusion targets. KULL uses the C++ programing language, Message Passing Interface (MPI), and makes use of object oriented programming and templating to allow efficient polymorphism[54]. Teleportation error is quantified for a one dimensional problem using both the teleportation correction and source tilting methods. The teleportation correction method is applied to a two dimensional problem which demonstrates how teleportation error can result in slower energy transport in certain problems. Additionally, the accuracy of the teleportation correction method is assessed for a three dimensional problem. Finally, the computational cost of the teleportation correction method is compared to the source tilting method.

6.1 One Dimensional Teleportation Correction Results

This section uses a time dependent one dimensional problem with dimensionless units tailored to show significant teleportation error, in order to quantify the effectiveness of the teleportation correction method. The radiation constant, a; and speed of light, c are set equal to unity. For simplicity, the problem has no spectral dependence, which is known as a gray problem. This simulation defines the absorption coefficient as having a temperature dependence defined as $\kappa = 10/T^3$, and uses a value of 7.14 for the coefficient of specific heat at constant volume, c_v. There is a radiative source with a temperature of one at the problem origin that begins heating the initially cold, $T = 0.01$units, medium at time equals zero. Figure 6.1 shows the solution of material temperature at time=500units using IMC with the source tilting correction, and an Implicit Monte Carlo Diffusion (IMD) method. Gentile describes the IMD method as using a discretization of a diffusion approximation applied to the radiative thermal transport equations to calculate the probabilities used in propagating IMC particles[20]. IMD is used here since it does not exhibit teleportation error, and is used in Figure 6.1 to illustrate the error of the IMC solution. While the source tilting method is known to decrease teleportation error, in this problem source tilting does not eliminate teleportation error at a low spatial resolution. The higher spatial resolution results show good agreement between IMD and source tilting, which indicates that the 200 cell spatial discretization is sufficient to eliminate teleportation error when using the source tilting method for this problem. If the 200 cell IMD solution is averaged onto the 20 cell grid, the location of the radiative wavefront is consistent. The IMC solutions using source tilting show the radiative wavefront moving farther into the medium as spatial resolution is decreased resulting from teleportation error.

Figure 6.2 illustrates the mechanism of the teleportation error by showing the distributions of emitted particles and locations sampled by the teleportation correction method. The teleportation correction method samples points that represent loca-
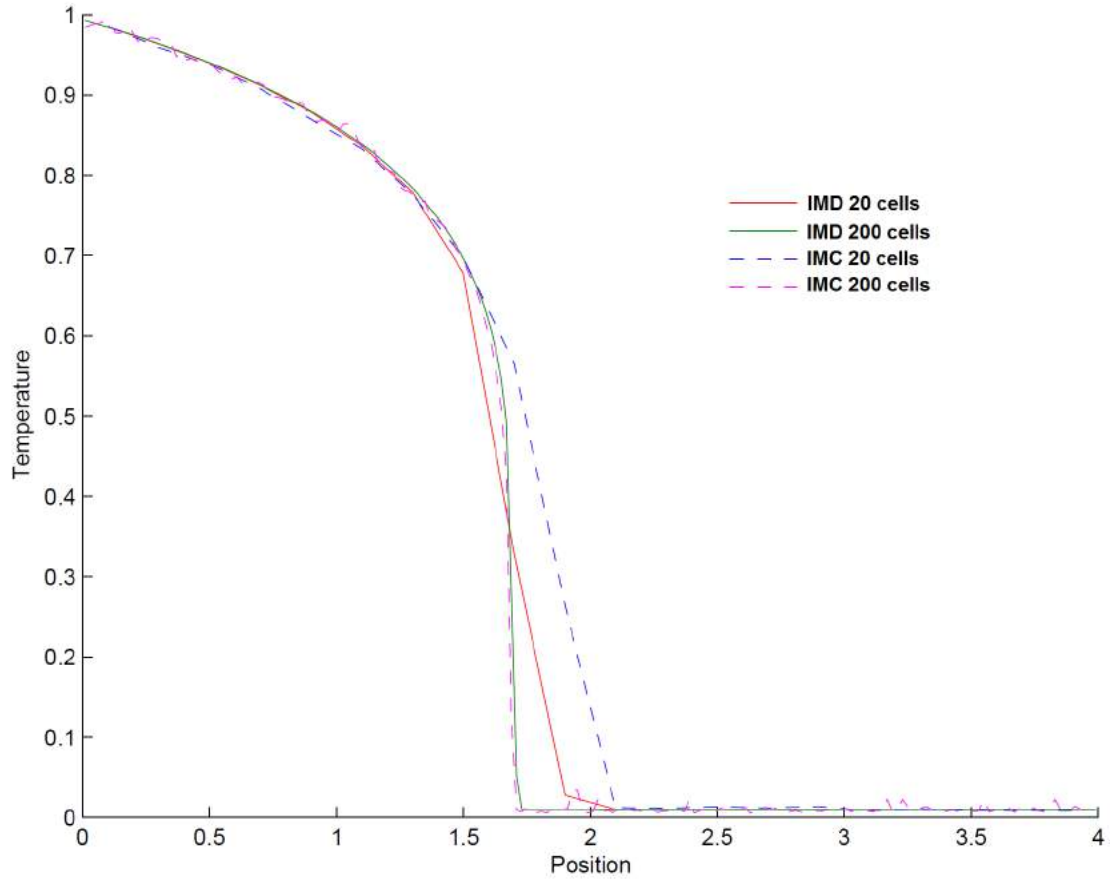
Figure 6.1: Material temperature solutions for IMC with source tilting and IMD at different spatial resolutions

tions where energy is absorbed by the medium within a spatial cell. Any difference between sampled absorption locations, and emission locations sampled through the source tilting method is indicative of the unphysical redistribution of energy within a spatial cell. This redistribution results in less emission at locations closer to the energy source instead of being emitted at locations that have absorbed little or no radiative energy from the source. Figure 6.2 also shows that the source tilting method is adequate for sampling emission locations when the cells are relatively transparent to radiation and the temperature gradient is smaller. The accuracy of the source tilting method in cells with smaller temperature gradients demonstrates how the method is able to accurately predict the radiative wavefront location when spatial resolution is increased. The figure also shows that the teleportation correction method could be

applied only to cells with large temperature gradients without sacrificing the accuracy of the solution.
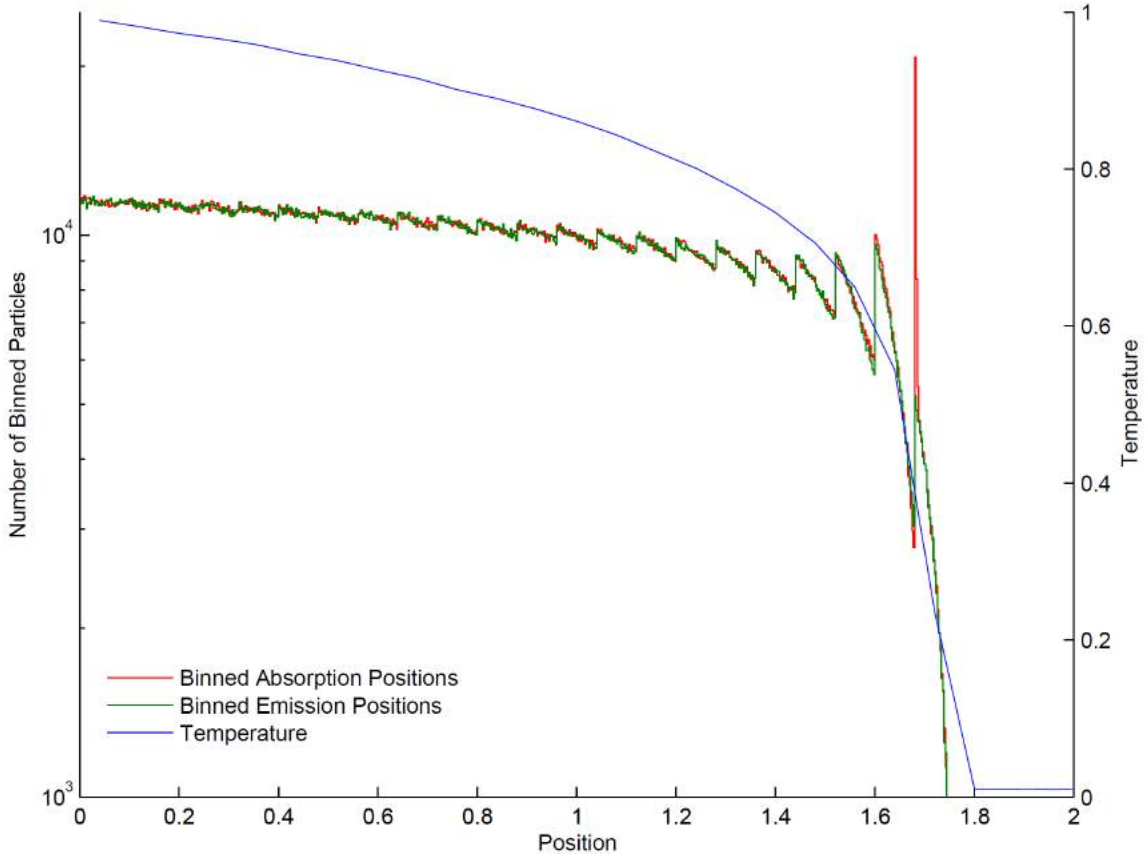
Figure 6.2: Location distribution of absorbed and emitted particles

Figures 6.3 and 6.4 show solutions for material temperature at time=500units and a time step of 1unit, at different spatial resolutions, using the teleportation correction and source tilting methods respectively. The solutions using the teleportation correction method correctly predict the radiative wavefront position, independent of the spatial resolution. While there are inherent differences in the solutions due to the different levels of discretization, as can be seen in the IMD solutions in Figure 6.1, the solutions at lower spatial resolutions overlap with averaged high resolution solutions. The agreement of the averaged solutions is shown in Figure 6.7. The speed of the wavefront, predicted using the source tilting method, increases as the spatial resolution decreases. Teleportation error in these results increases as spatial resolu-

tion is decreased, allowing radiative energy to propagate into the medium faster than it should.
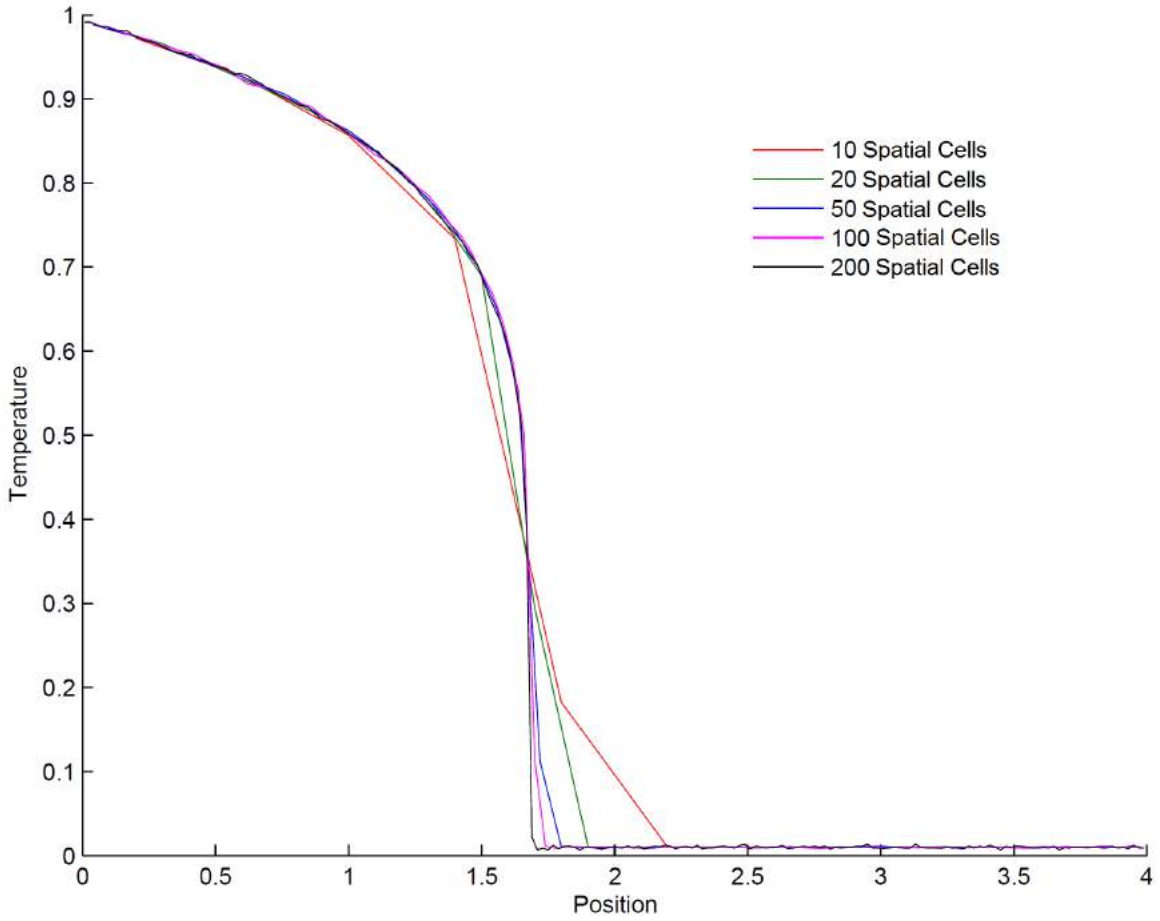
Figure 6.3: IMC solution using teleportation correction method at different spatial resolutions

Figures 6.5 and 6.6 show solutions for material temperature at time=500units and 10 spatial cells, at different temporal resolutions, using source tilting and the teleportation correction method. The influence of the temporal resolution on the teleportation error is smaller than the influence of spatial resolution for this problem. Both the source tilting and teleportation correction method show some dependence of the solution on the temporal resolution; although, the teleportation correction solutions show smaller variation than the source tilting solutions. Since solutions using the teleportation correction method still show some dependence on temporal
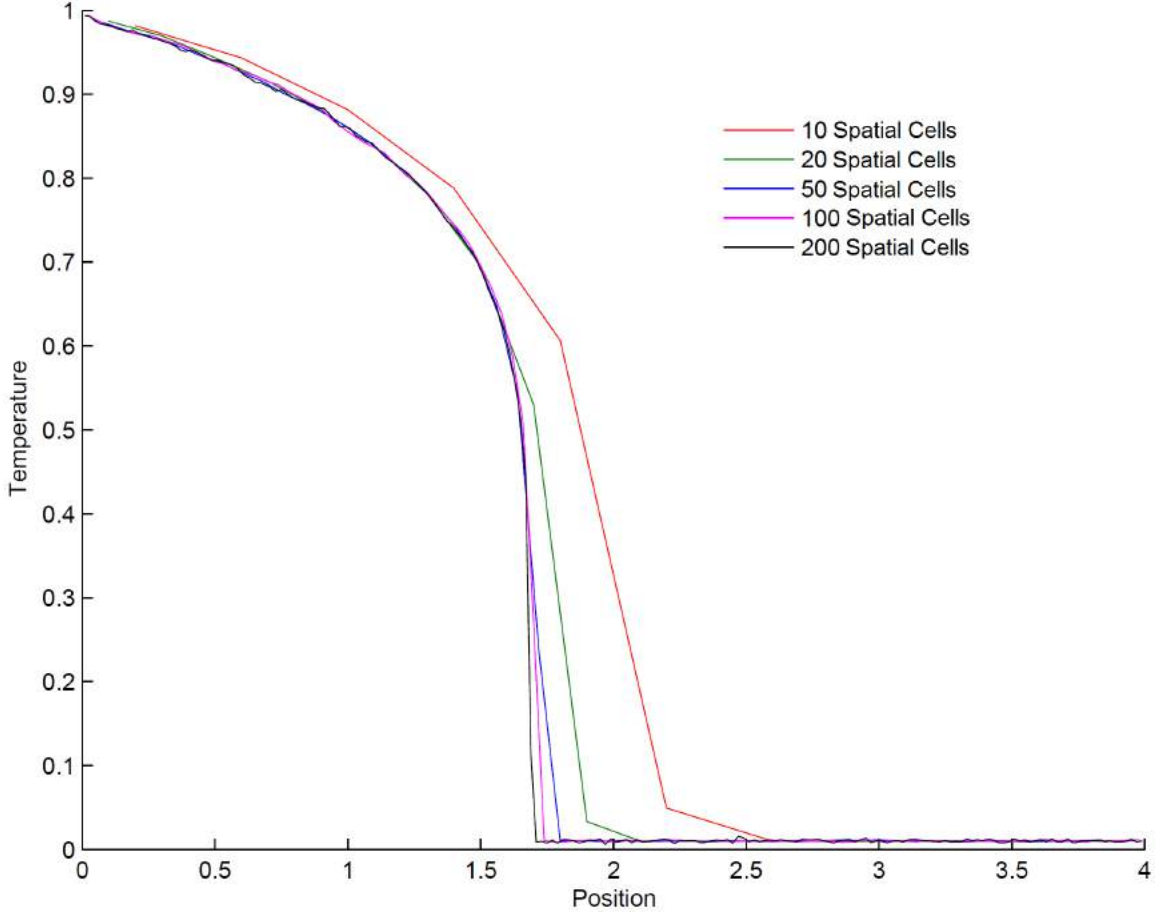
Figure 6.4: IMC solution using source tilting method at different spatial resolutions

resolution, it is likely that there is a mechanism, other than teleportation error, causing some portion of this dependence.

To quantify the teleportation error solutions at varying spatial and temporal resolutions, a reference solution is generated using IMD at the lowest spatial resolution, which is ten spatial cells for this problem. Since the spatial cells are the same size, and the coefficient of specific heat at constant volume is constant throughout the domain, the temperatures at the lowest spatial resolution are determined by an average of the temperatures found at higher spatial resolutions. Using the same spatial resolution to determine the solution error ensures comparisons between different spatial resolutions are consistent. Figure 6.7 shows the summation of relative errors taken at each spatial cell for a range of spatial and temporal resolutions. The combination of

117
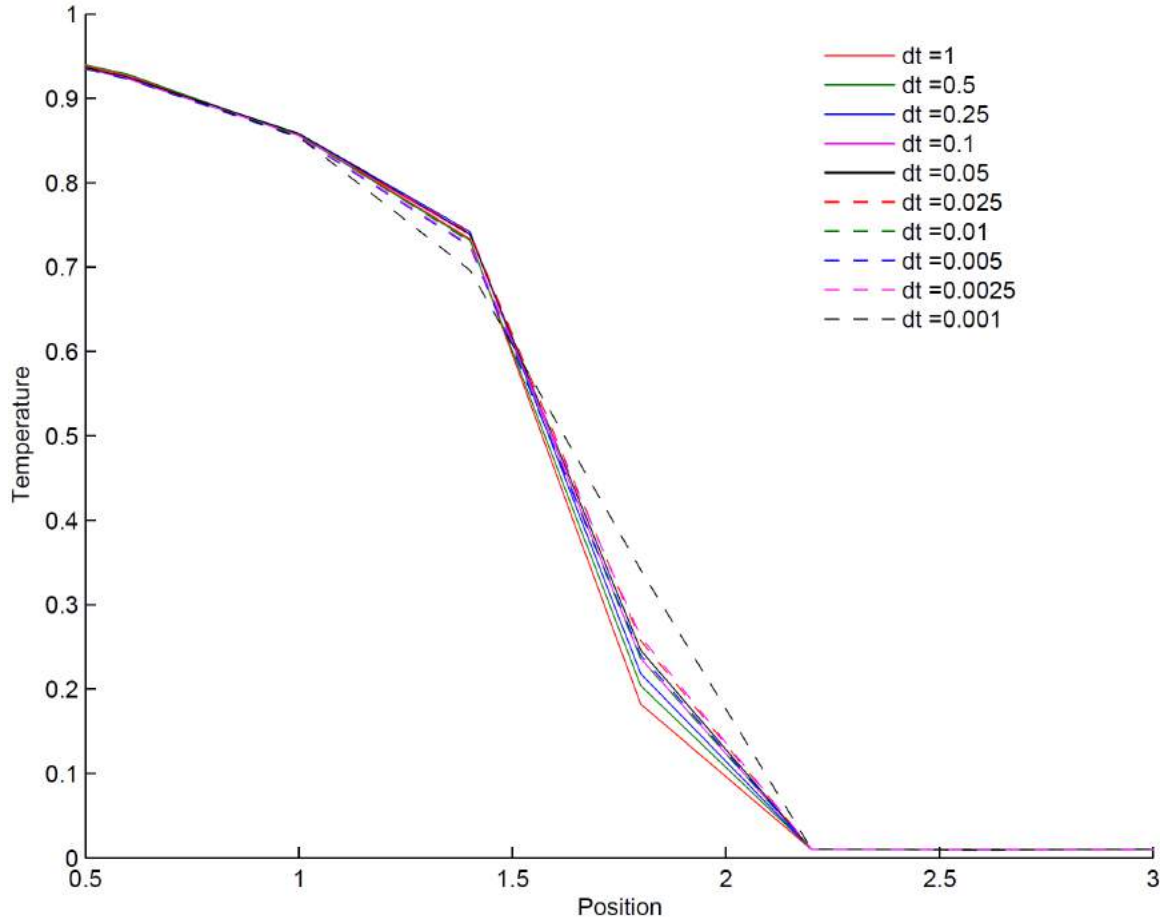
Figure 6.5: IMC solution using teleportation correction method at different temporal resolutions

high spatial resolution and low temporal resolution causes both the source tilting and teleportation correction solutions to become unstable, resulting in the large error at the corner of the figure. The teleportation correction method converges to the correct solution quickly while showing small errors for coarse spatial grids. Both methods show error as the temporal resolution is increased, but the teleportation correction method shows less dependence on temporal resolution.

6.2 Graziani Crooked Pipe Simulation Results

In this section, the teleportation correction method is applied to a two dimensional problem known as the Graziani crooked pipe test, also called the *tophat problem*[20,

118
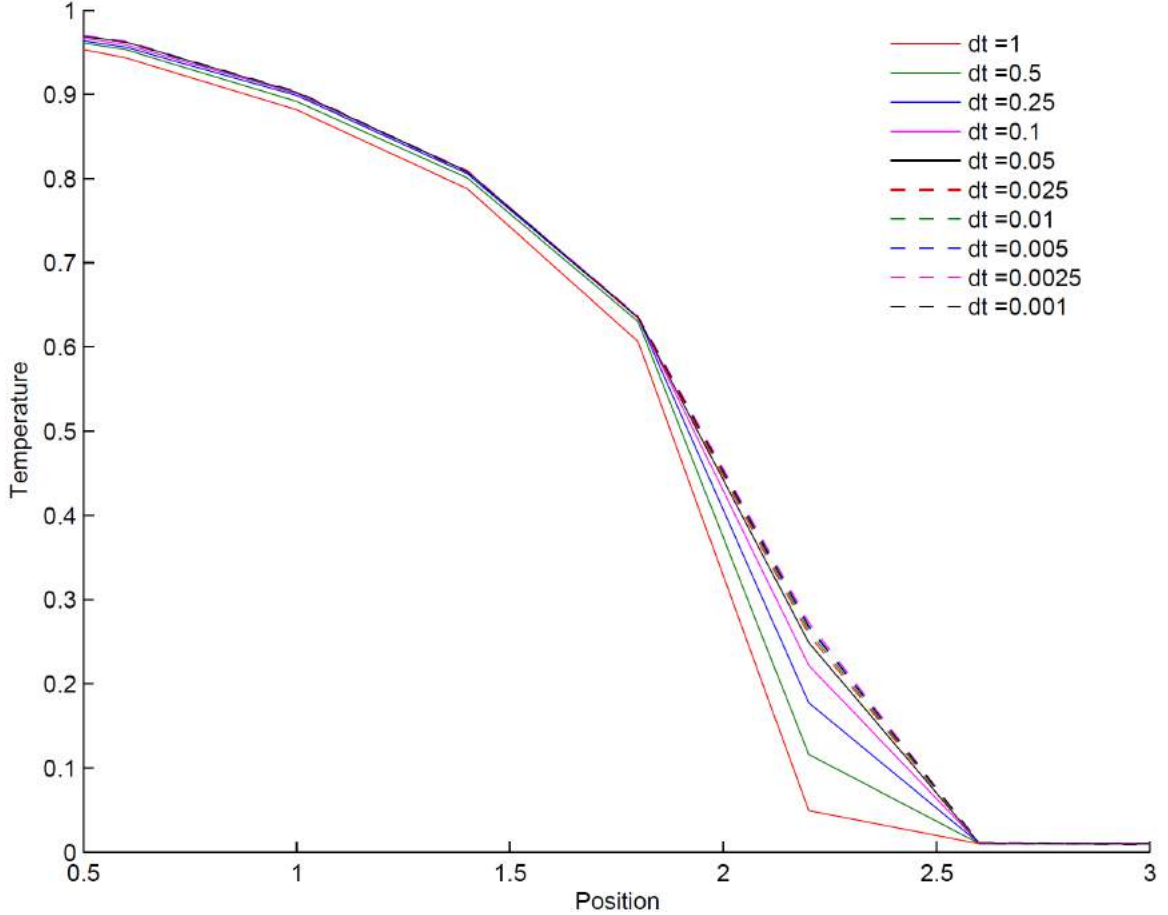
Figure 6.6: IMC solution using source tilting method at different temporal resolutions

23]. Figure 6.8 depicts a cylindrically symmetric cross section of the problem domain, showing high density material in gray and low density material in white. At x=0cm, there is a radiative source with a temperature of 0.5keV at the edge of the low density material. The high density material has a density of 10g/cm^3 and an opacity of 2000cm^{-1}. The low density material has a density of 0.01g/cm^3 and an opacity of 0.2cm^{-1}. The coefficient of specific heat at constant volume is $10^{15}\text{erg}/(g\ keV)$ for both materials. At time=0seconds the domain has a temperature of 0.05keV and the time step is $1.0\text{x}10^{-3}$seconds. The time step increases by a factor of 1.1 for each time step until a value of 1second is reached, after which, the time step is constant.

The spatial grid has a spacing of 0.1cm in the axial and radial directions. There is a sub-grid at the interface regions with initial node spacing of 0.001cm, with subsequent

119
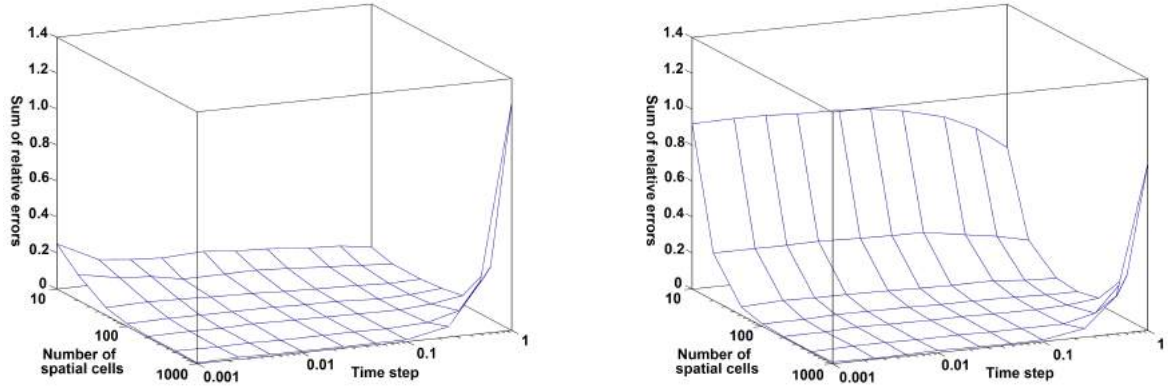
(a) IMC solution using teleportation correction method

(b) IMC solution using source tilting

Figure 6.7: Sum of relative errors for one dimensional solutions at different spatial and temporal resolutions
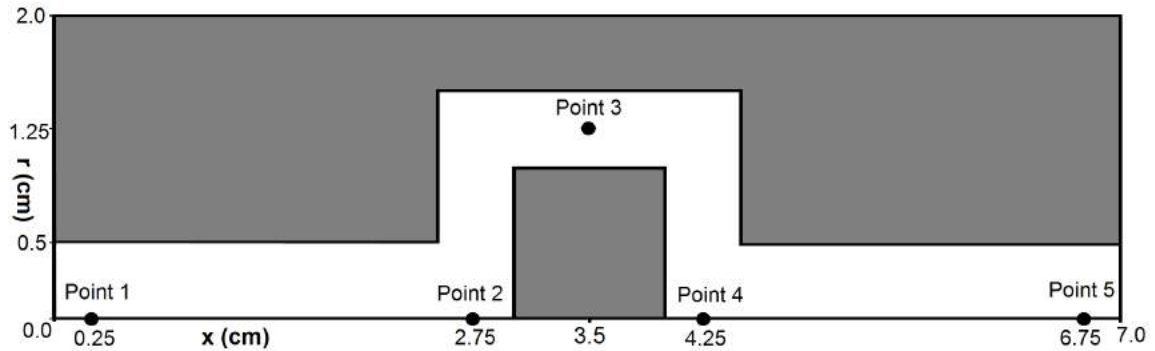
Figure 6.8: Graziani crooked pipe cross-section

node spacing set by a growth factor determined by the number of sub-grid points. In this problem, the interface between the two materials is the region of highest opacity gradient, and thus will show the largest teleportation error. The response of this solution to the spatial resolution in the interface region is used to assess the effectiveness of the teleportation correction method. Figure 6.9 shows the grid using 10 sub-grid cells.

Figure 6.10 shows the temperature change over time at the points defined in Figure 6.8. The radiative source heats the low density material near point one, and propagates through the low density material to point 2 while also heating the surrounding high density material. Re-emission of absorbed radiation and effective
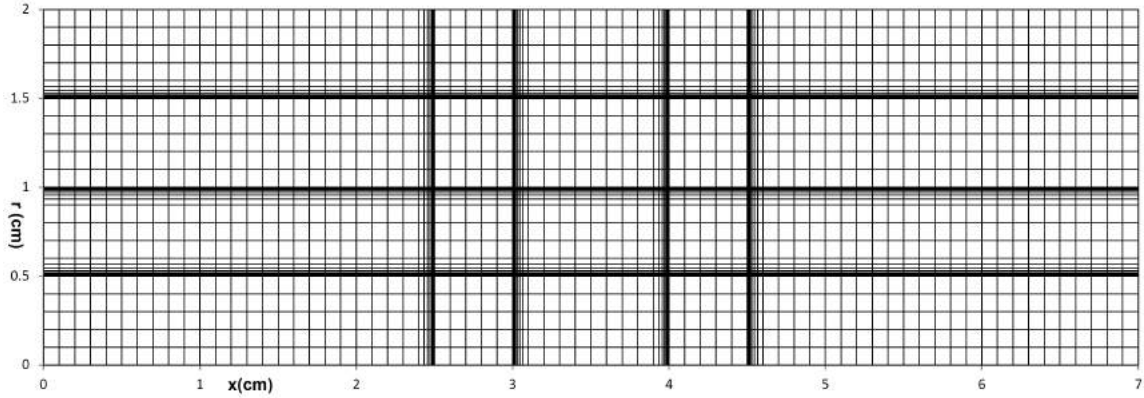
Figure 6.9: Spatial grid for Graziani crooked pipe problem using 10 sub-grid cells

scattering allow radiation to continue propagating around the corner of the pipe. This process continues through the next two corners until reaching the exit at x=7cm. For this problem, teleportation error reduces the speed of the radiative energy transport through the low density region. Teleportation error in the high density material at the interfaces causes radiative energy to transport through the high density medium faster than it should. Consequently, energy is removed from the low density material at too high a rate, reducing the rate energy transport through the low density material. The low spatial resolution teleportation correction results are consistently lower than the high resolution results, which indicates that discretization error is influencing the low resolution results. Even with this error, the teleportation correction results at lower resolution agree with the higher resolution results using the source tilting method.

Figure 6.11 shows the material temperature at x=0.25cm enlarged to focus on the region at the material interface. The dependence on spatial resolution on the speed of radiative energy propagation is similar to the dependence seen in Figures 6.3 and 6.4. The source tilting method shows faster energy transport into the higher density material from the lower density region that results in slower energy transport in the lower density material. The lower resolution results using the teleportation correction method show good agreement with the higher resolution results.
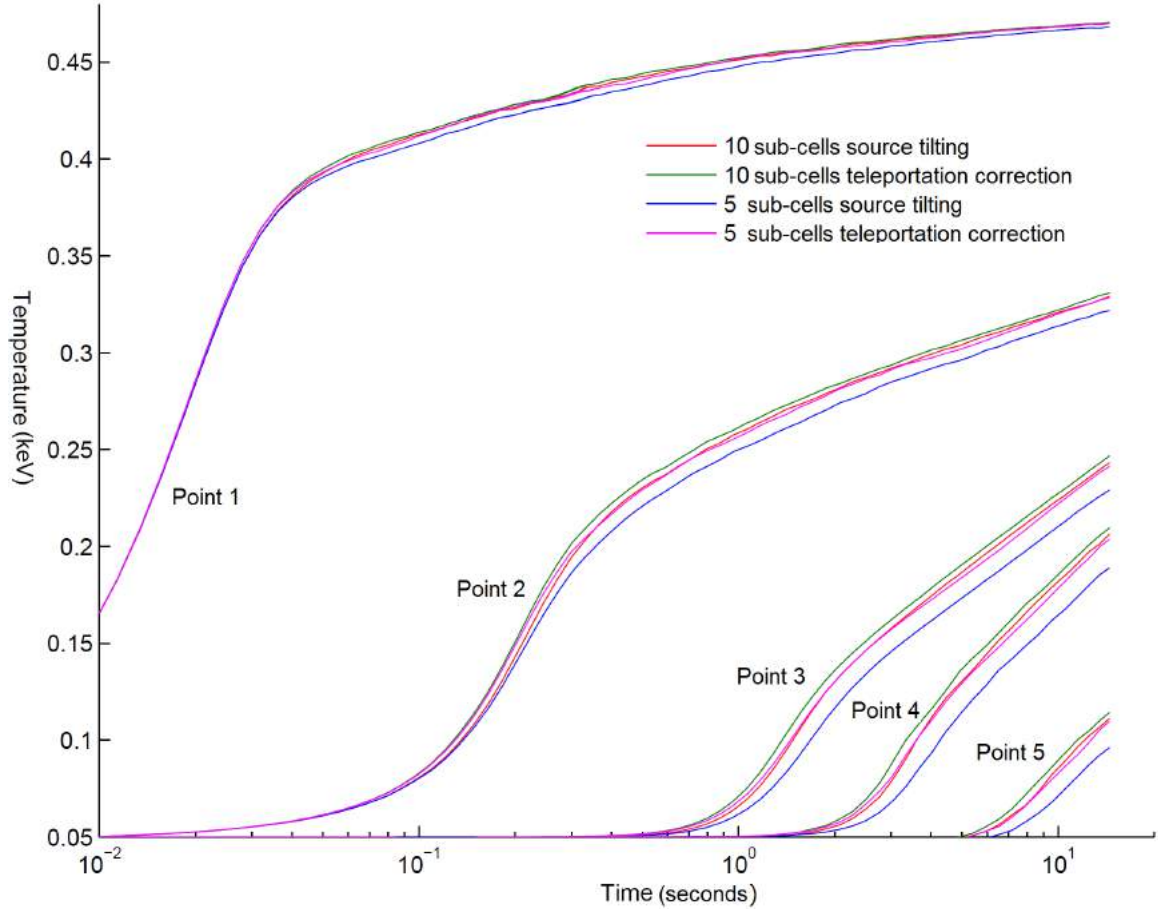
Figure 6.10: Point temperature over time for Graziani crooked pipe problem at five points

6.3 Three Dimensional Simulation Results

The teleportation correction method is applied to a three dimensional problem with four different materials arranged in concentric cylinders in this section. Figure 6.12 shows the coarse spatial grid used in this problem and the locations of the materials with distances in centimeters. This coarse grid has 30 radial nodes, 64 angular nodes, and 15 height nodes with the angular nodes cut to make a quarter cylinder. A higher resolution grid with a factor of four more nodes is used to determine the dependence of the solutions on the spatial resolution. One million particles are used for the coarse grid, and 20 million for the high resolution grid. The spatial grids can be split into a number of domains that are simulated by different groups

122
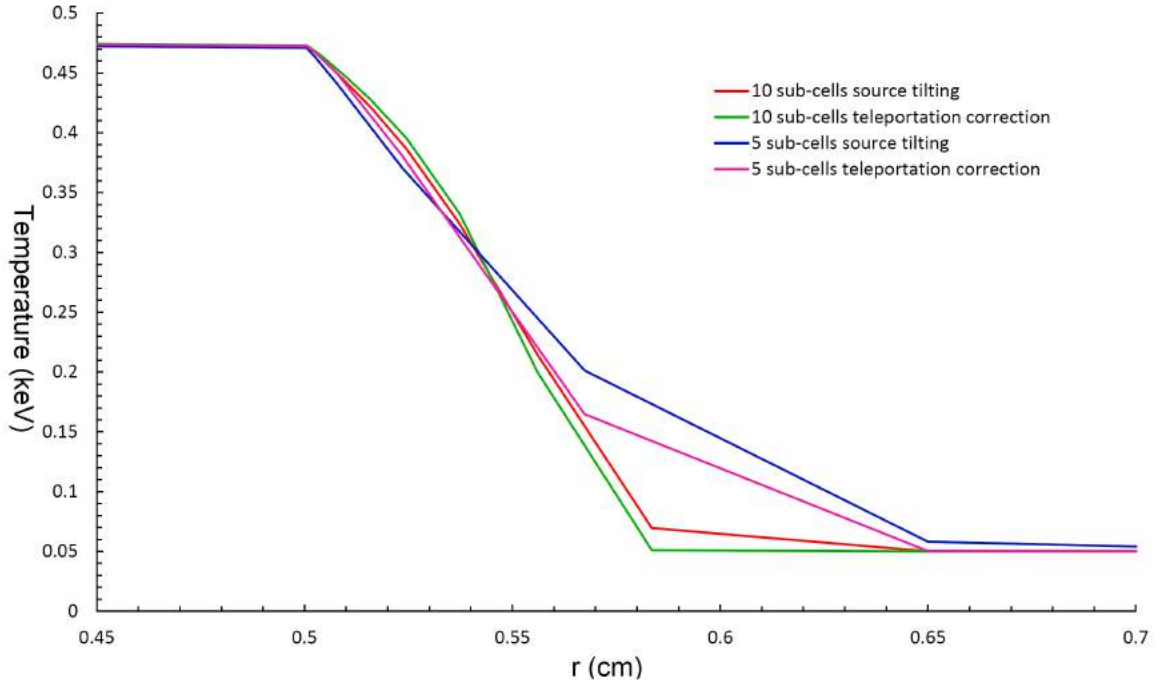
Figure 6.11: Material temperature at x=0.25cm for Graziani crooked pipe problem

of processors. Spectral properties use a 30 frequency group model interpolated for the thermodynamic properties of the medium that is detailed by Kumbera[33]. The coefficients of specific heats at constant volume are determined by tables reported by Hill[27]. There is a radiative source with a temperature of 1keV at the z=0 plane, exits at the upper plane and outer cylinder diameter, as well as reflecting boundary conditions along the angular cuts of the quarter cylinder. The medium is initially at a temperature of 0.01keV at time=0seconds, and the time step is 1.0×10^{-11} seconds with an end time of 1.0×10^{-8} seconds.

Figure 6.13 shows the temperature contours across a radial plane of the medium. The absorption coefficient and coefficient of specific heat at constant volume for the hydrocarbon material is lower than the other materials in the simulation, allowing radiation to penetrate into the hydrocarbon material relatively quickly. As the hydrocarbon material is heated, a portion of the radiation emitted by the hydrocarbon material heats the adjacent iron. The relationship between the silicon dioxide and stainless steel is similar, although silicon dioxide is heated at a slower rate than the

123
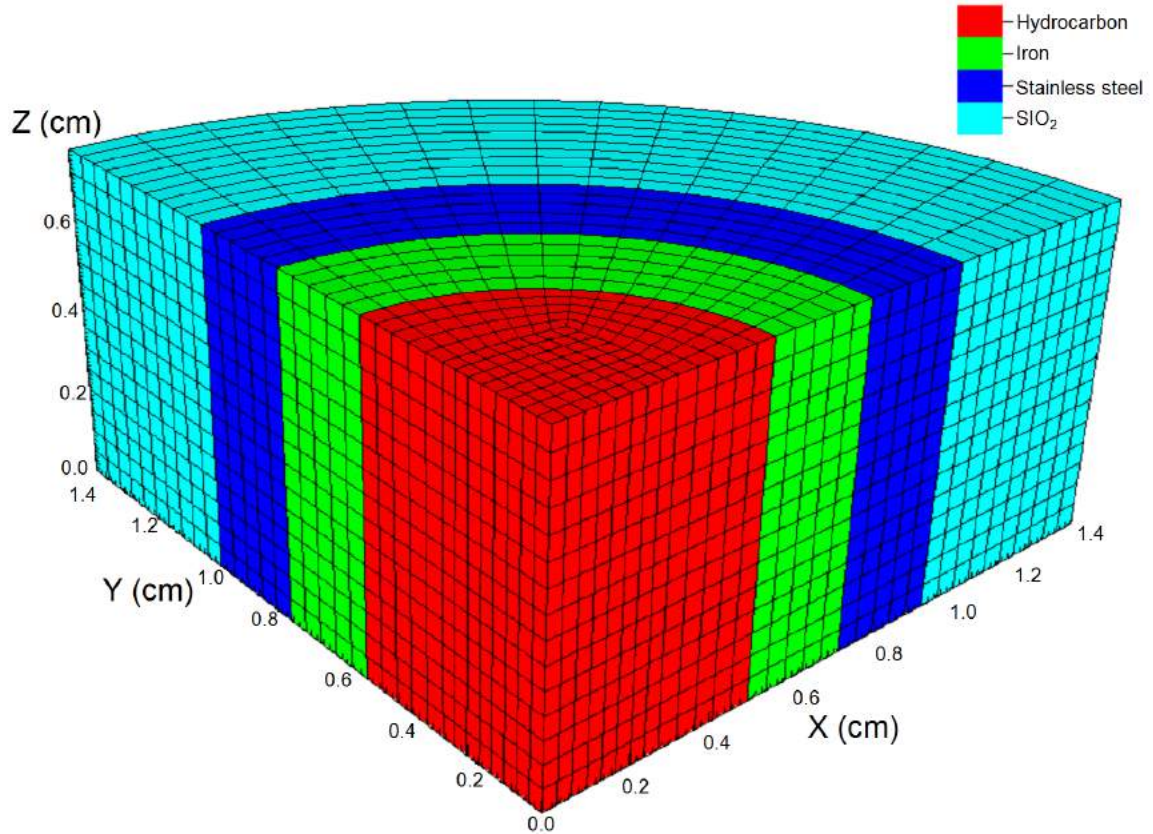
Figure 6.12: Three dimensional spatial grid showing cuts along symmetry planes

hydrocarbon. Comparing the results using the teleportation correction and source tilting, the temperature profiles are similar. The radiative wavefront for the source tilting solution penetrates farther into the medium, and the medium near the source is colder as the energy is moving into the medium too quickly. These results show that the high resolution grid requires further refinement to eliminate teleportation error when using the source tilting method.

To compare the solutions of the low and high spatial resolutions, the edge of radiative heating is found and set as the background of the low spatial resolution solutions. Figure 6.14 shows the partially transparent low spatial resolution temperature solution superimposed over the high spatial resolution temperature solution. The source tilting method shows the radiative wavefront traveling too quickly where the temperature gradients are large. Temperature gradients are highest in the iron and stainless
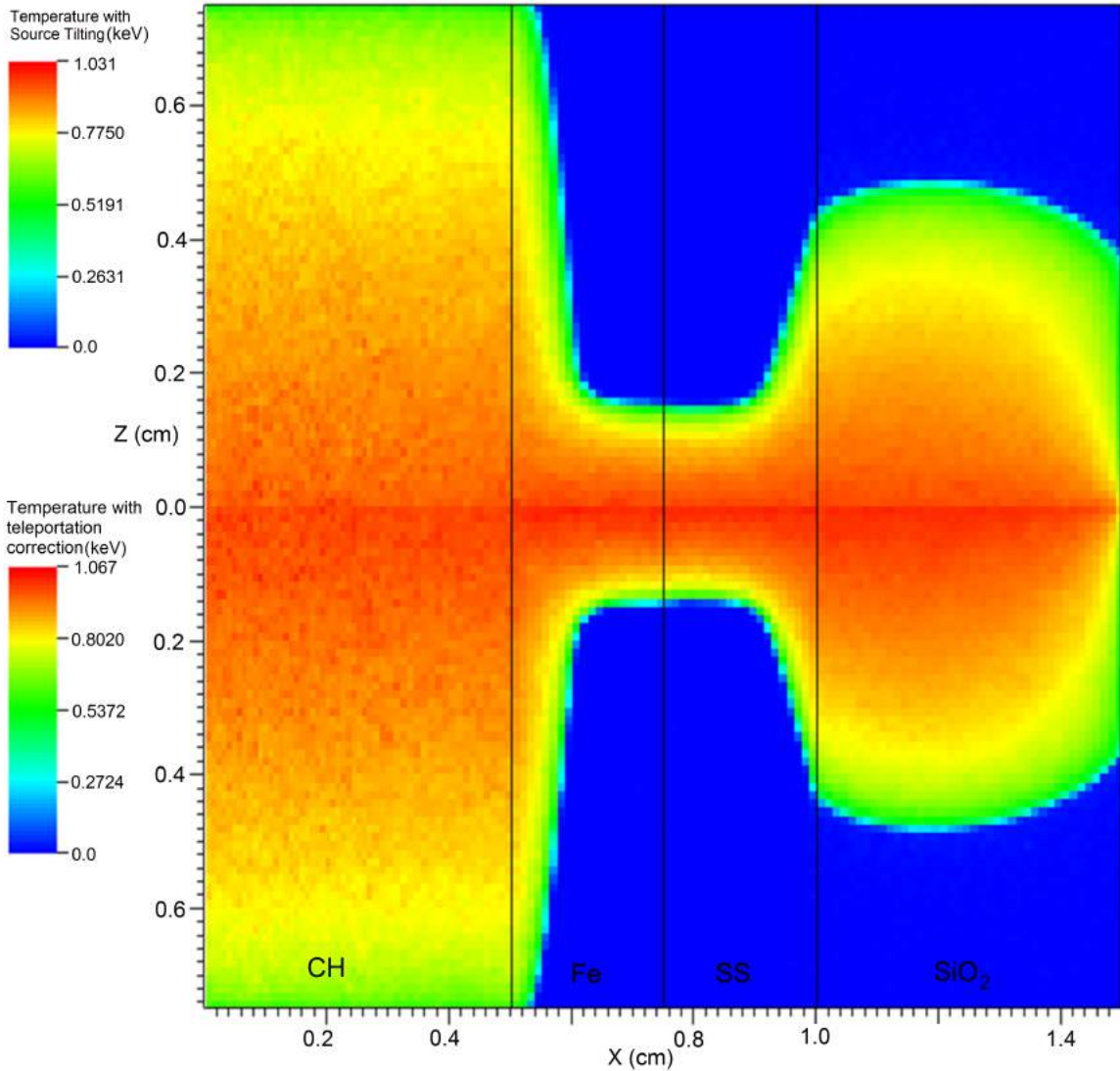
Figure 6.13: Temperature of medium along a radial plane for the high resolution spatial grid for source tilting and teleportation correction methods

steel where the higher absorption coefficients of these materials concentrate energy near the edges. In the silicon dioxide, the source tilting method shows relatively low error where there are smaller temperature gradients. The teleportation correction method shows good agreement between the high and low spatial resolutions. There is little to no radiative heating in spatial cells that do not contain some portion of the high resolution radiative wavefront, indicating that the position of the wavefront is predicted correctly.
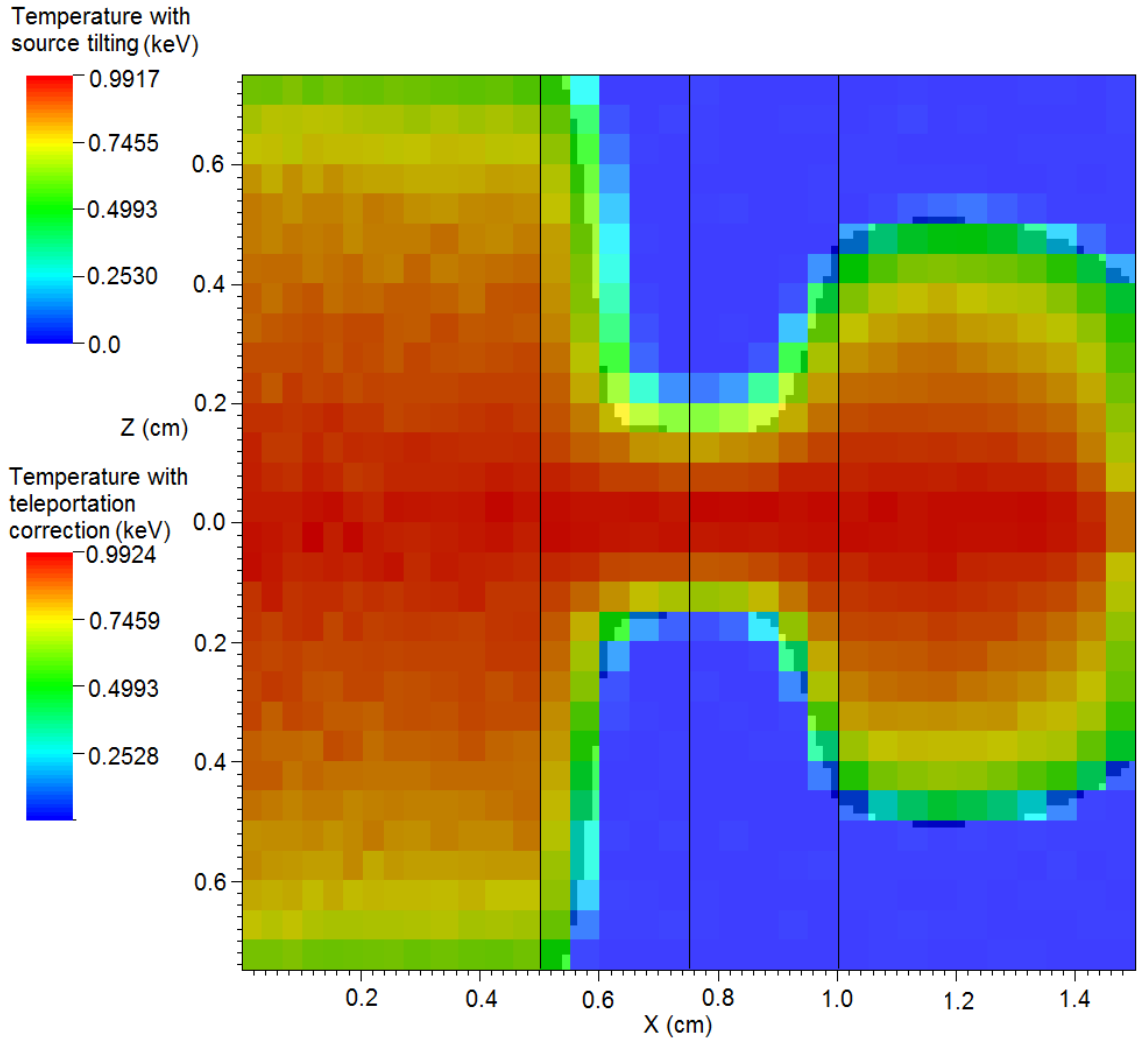
Figure 6.14: Comparison of temperature contours at low and high spatial resolutions

6.4 Computational Costs

The teleportation method requires sampling of each particle path, and sampling of absorption locations when a path is sampled. Thermal emission of particles requires a sampling of absorption locations stored in computer memory and the deletion of a location once sampled. The storage of these absorption locations can be problematic as it requires storage of a number of locations, which can be on the order of magnitude of the number of particles used in the simulation. By contrast, the source tilting method requires a sampling of the linear spatial distribution of T^4. This sampling

is relatively simple for simple geometries, but more complex geometries lead to more complex calculations to find the T^4 distribution.

Table 6.1 shows the simulation times of the teleportation correction method relative to the source tilting method. The teleportation correction method has 8.6 and 3.3 percent higher average computational costs over the source tilting method for the one and two dimensional problems respectively. The costs of the teleportation correction method do not show any trends as the number of processor cores utilized increase that would indicate a change in the parallel efficiency compared to the source tilting method.

Number of processor cores	1	8	16	32	64	128
One dimensional problem	1.104	1.078	1.156	1.087	1.036	1.054
Two dimensional problem	1.008	1.037	1.037	1.04	1.046	1.031

Table 6.1: Computational costs of teleportation correction method relative to source tilting method for one and two dimensional problems

Table 6.2 shows the computational times of the three dimensional problem at different numbers of domains and processor cores relative to the source tilting method. For this problem, the teleportation correction method has 13.1 percent lower average computational cost relative to the source tilting method. Sampling the T^4 distribution for the more complicated spatial grid of the three dimensional problem requires additional computational resources above the one or two dimensional problems. The performance of the teleportation correction method relative to the source tilting method does not show large variations as the number of domains or processor cores are changed. If the resolution necessary to minimize discretization error is significantly lower than the resolution required to minimize teleportation error using the source tilting method, then the teleportation correction method can reduce the size of the grid, reducing the computational cost of the problem.

The additional memory requirement of the teleportation correction method varies depending on the absorptivity of the medium. If the average particle energy does not

Number of domains	1			2		4		8	
Number of processor cores	1	8	16	8	16	8	16	8	16
Computational cost	0.87	0.86	0.86	0.90	0.90	0.882	0.88	0.82	0.85

Table 6.2: Computational costs of teleportation correction method relative to source tilting method for the three dimensional problem

change significantly between time steps, the number of absorption locations sampled is approximately equal to the number of particle thermal emissions. The number of dimensions required for storage of the location information, and precision required, depends on the problem. The worst case scenario is when all particles are absorbed in a time step such that the maximum number of particles are emitted in the next time step. As implemented in KULL, this scenario would increase memory utilization by a maximum of 25 percent for a three dimensional problem using double precision values to store absorption locations.

6.5   Summary

One dimensional results presented in this chapter can show significant teleportation error when using the source tilting method dependent on the spatial resolution of the simulation. Using the same conditions, the teleportation correction method shows little to no dependence of radiative energy transport on the solution spatial resolution, where the source tilting method shows faster transport of radiative energy as spatial resolution is decreased. The two dimensional crooked pipe test shows teleportation error causing a deceleration of the transport of radiative energy in the low density material due to more rapid energy transport out of the low density material into the high density material. The teleportation correction method shows some discretization error at a lower spatial resolution for the two dimensional problem, but still shows good agreement with higher resolution source tilting method results. Solutions to a three dimensional problem show teleportation error in source tilting solutions that

is dependent on spatial resolution and results in faster radiative transport into the medium. The teleportation correction method is shown to predict the location of the radiative wavefront accurately when the spatial resolution is decreased. Relative to the source tilting method, the computation time of the teleportation method is shown to be under 9 percent slower for relatively simple one dimensional problems, and over 13 percent faster for the more complex three dimensional problem.

CHAPTER VII

Summary and Conclusions

A summary of the dissertation is presented in this section including contributions to the field of radiative thermal transport of scramjets. Finally, recommendations for future research directions are presented.

7.1 Summary

The thesis began with a description of the motivation of this work and a description of scramjet propulsion systems. Scramjets can potentially operate across a wide range of hypersonic speeds; however, characterizing the safe operating range of these devices is difficult. The unstart phenomenon causes shock propagation upstream towards the inlet and subsonic flow throughout the scramjet. Experimentally characterizing unstart is difficult as flight experiments are expensive, ground testing facilities cannot fully replicate flight conditions, and no computer models have been validated with all the physics necessary to simulate unstart. The goal of the Stanford Predictive Science Academic Alliance Program (PSAAP) Center is to improve computational models for use in supersonic combustion environments and validate those models against experiments. Once a suitable computational model is validated it is necessary to sample the range of input and modeling uncertainties to quantify the probability of unstart occurring for a given operating condition.

The high temperatures and radiative species present in a scramjet combustion chamber motivated the current work to produce radiative thermal transport simulations with minimal epistemic uncertainty. The Monte Carlo Method (MCM) and Line By Line (LBL) methods were chosen for use in this thesis as they were the most accurate models available. Unfortunately, the computational costs of these models were too high to practically perform a full sensitivity analysis of the radiative thermal heat flux. As a compromise, the Discrete Ordinates Method (DOM) was chosen to conduct sensitivity analysis of radiative heat flux while the high fidelity model quantified the uncertainty of the DOM simulations.

Chapter II started with background of thermal radiation, and defined variables that were used to write the radiative thermal transport equations. The assumptions used in derivation of the transport equations were detailed while not neglecting phenomena that would affect the solution accuracy. Leading into the particle description of a MCM, the physical meaning of the terms in the radiative thermal transport equations were given. The MCM was introduced and the stochastic nature of the sampling of the solution through the use of particles was described. Teleportation error was introduced as an error specific to particle based stochastic methods that caused radiative energy to travel too quickly through the medium due to how particle emission locations were sampled. A brief description of the DOM was given to provide background for DOM solutions shown in Chapter V. The physics of radiative emission and absorption were introduced before the equations that described the shape of spectral lines were shown. The LBL spectral model was discussed with emphasis placed on the magnitude of the calculations involved, which provided justification for the use of tabulated values. Approximate spectral models were introduced which would provide background on the spectral model used for DOM solutions.

Chapter III provided details on the specific implementation that was chosen for the MCM. The radiative thermal transport equations were linearized according to

the method proposed by Fleck and Cummings[29]. The Implicit Monte Carlo (IMC) method was derived by integrating the radiative thermal transport equations over time, defining a time centering for the variables, and solving for the radiative energy density at the end of the time step. Remaining time centered and time averaged variables would be considered to be equal to the values at the start of the time step. This assumption increased the uncertainty of the method over time; however, the flowfield in scramjet radiation simulations was considered to be in equilibrium. With the equations derived, the path of a typical particle was tracked. Starting with selection of particle sources and subsequent emission, the particles were moved until a collision event, boundary, or time step end were encountered. Energy was deposited as particles moved through the medium by using a weighted absorption variance reduction technique, which terminated, particles once their energy was depleted. Once all particle paths were terminated, the sum of the radiative heat flux was used to update the medium temperature. The teleportation correction method was detailed at this point, as the implementation was linked closely to how IMC particle paths were tracked. The method sampled absorption points based on the deposition of energy and used those locations for particle emissions in the subsequent time step. Since the LBL method modeled the absorption coefficient based on the line shape equations shown in Chapter II, the LBL section in this chapter detailed the creation of the look-up tables used for sampling absorption coefficients. To reduce computational costs, an additional table of the normalized cumulative absorption coefficient was made so that a summation of the absorption coefficient tables for every particle wavenumber sampling could be avoided.

Chapter IV described the HIFiRE-2 scramjet system and showed Computational Fluid Dynamics (CFD) solutions of the flowfield. The trajectory of the HIFiRE-2 flight test vehicle was described providing context for the intended operating conditions for ground tests. The ground test experiments conducted at the Arc-Heated

Scramjet Test Facility located at the NASA Langley Research Center were described which were the basis of the CFD solutions shown in the next section. CFD++ was the software used by the AFRL to produce the HIFiRE-2 flowfield solutions that were used for the radiative thermal transport simulations. The IMC domain was defined and the relevant flow properties of temperature, pressure, and water mass fraction were visualized with the relevant flow features explained.

Chapter V presented the IMC radiation solutions for water vapor in the HIFiRE-2 scramjet. An initial assessment of the epistemic uncertainty of DOM solutions was made, using one dimensional simulations of extracted flowfield data at selected points. Eleven points were compared showing the spectrally resolved heat flux at each of the points. Results from the two methods showed good agreement with a maximum difference of six percent in the low heat flux region. Three dimensional IMC results were presented showing the heat flux to the scramjet walls for a 10 billion particle simulation. The heat flux was compared to convective heat flux found from the CFD simulation and was found to account for less than two percent of the heat flux in the majority of the scramjet. Volumetric heat flux within the scramjet was shown to illustrate the sources of heat flux within the medium. The low magnitude of absorbed heat flux by the gas illustrated why the medium was showing negative heat fluxes throughout the domain. Statistical variance of the radiation solutions using 100 million particles was found in order to quantify the variance of the larger 10 billion particle simulations. Variance was found to be less than 0.5 percent for areas showing significant heat flux. Plots of the IMC parallel computing performance showed that the code scaled well as the number of processors were increased.

The DOM solution of the heat flux was shown and then compared with the IMC solution. The relative difference between the solutions was found with DOM showing lower heat fluxes for many areas except for the forward section of the cavity flame-holder. The absolute value of the relative difference between the IMC and DOM

solutions showed that there was good agreement through most of the flow. Large relative differences shown upstream of the cavity flameholder were amplified due to the low flux in that region.

In order to quantify the uncertainty of the IMC radiative heat flux results as a result of the uncertainty of the spectral line parameters in the HITEMP database, a one dimensional problem was used to conduct a sensitivity analysis on the line parameters of groups of five lines. The parameters were perturbed based on the reported uncertainties listed in the HITEMP database and a Latin hypercube sampling of the design space. The correlation coefficients of the radiative heat flux to the walls with the spectral line parameters were found. Additionally, plots of the heat flux variations against the variations of each of the parameters were inspected for nonlinear correlations. Forty groups of lines underwent the same methodology and it was found that in all cases the line strength parameter dominated the variation seen in the heat flux. It was then reasonable to eliminate the other parameters from consideration and model the heat flux uncertainty based on the known uncertainty of the line strength parameter. The variation of the wall heat flux was found to vary linearly with the line strength parameter so the uncertainties for each line strength parameter were weighted based on the contribution of that line to the absorption coefficient at a given wavenumber point. The estimated errors in the absorption coefficients were used in the three dimensional HIFiRE-2 simulation to propagate an uncertain flux through the problem that was compared to the nominally calculated heat flux. The resulting relative error showed a relatively small range indicating that the contributions from the different parts of the spectrum change relatively little through the domain as was seen from the one dimensional simulations.

Chapter VI documented the application of the teleportation correction method to three different types of thermal radiation problems each designed to exhibit teleportation error. The setup of the one dimensional simulation was described. A plot

showing the difference between sampled absorption points and the locations of emissions highlighted the underlying mechanics of teleportation error. Solutions of the same problem at different spatial resolutions showed the independence of the solutions using the teleportation correction and the faster movement of the radiative wavefront in the source tilting results with decreasing spatial resolution. Results from temporal resolution variation were less clear. There was less variation in the results using teleportation correction, but the presence of any variation indicated that another mechanism could be affecting the results. The plots showing the sum of the relative error of solutions at different spatial and temporal resolution clearly illustrated the superior convergence of the teleportation correction for this problem.

The two dimensional Graziani crooked pipe test showed teleportation error in a different way. Energy flux through the less dense material decreased as spatial resolution was lowered which contrasts with the increase in energy flux for the one dimensional cases. The slower energy flux in the low density region was due to increased energy flux to the high density regions which was removing energy from the less dense material. Plots of temperature over time showed that the teleportation correction method predicted the location of the radiative wavefront correctly while the source tilting results showed slower energy flux for the lower resolution cases.

A three dimensional problem with four different materials arranged in concentric cylinders was used for the final test case. The low resolution results were overlayed onto the high resolution results, showing that the results using the teleportation correction method correctly simulated the propagation of radiative energy. For the source tilting method, the high opacity regions, iron and stainless steel, generated the highest temperature gradients and resulting teleportation error. The radiation in the silicon dioxide region showed the radiative wavefront at the correct position for the source tilting method due to the lower temperature gradient in this material. The computational cost of the teleportation correction method relative to the source

tilting method improved as the system became more geometrically complex and was faster than the source tilting method for the three dimensional case. This trend was likely due to the increased computational cost in source tilting of solving the emission distribution on more complicated geometries.

7.2   Conclusions

As scramjets transition from experimental to operational systems, the need for high fidelity models capable of simulating the conditions within these engines will increase. Furthermore, the payload demands of an operational system will drive the need for larger scramjet propulsion systems. Radiative heat flux becomes more influential as the volume of the scramjet increases. These two drivers are likely to increase the need for high fidelity radiative thermal transport simulations into the future.

The IMC method enables simulations of radiative thermal transport in the HIFiRE-2 scramjet with low epistemic uncertainty. Neglecting radiative heat flux in a HIFiRE-2 simulation will under-predict wall heat flux by 1-8 percent with larger relative contributions in regions with lower convective heat flux.

For the HIFiRE-2 scramjet, the epistemic uncertainties of the IMC radiative transport method and the spectral property tables is negligible compared to the uncertainty introduced by the uncertainties in the current HITEMP 2010 database. The epistemic uncertainty of radiative thermal transport due to the HITEMP 2010 database is dominated by the line intensity parameter, and can be estimated within three percent using a linear weighting of the relative contributions of absorption lines to the absorption coefficient at a given wavenumber. This estimate predicts an uncertainty of up to 24 percent of the wall radiative heat flux for the HIFiRE-2 scramjet.

The DOM solutions using an S_8 quadrature have an epistemic uncertainty of under 15 percent in regions with significant radiative heat flux. The accuracy of the DOM

using an S_8 quadrature is sufficient for quantifying the sensitivity of the radiative heat flux solutions to the uncertainty of the thermodynamic values in the flowfield solution.

The teleportation correction method presented, reduces the teleportation error relative to the source tilting method. The teleportation correction method uses up to 25 percent more memory than the source tilting method and incurs a measured computational cost up to 16 percent higher for one dimensional problems, and 15 percent lower for three dimensional problems. Furthermore, the teleportation correction method enables the use of lower spatial resolutions which significantly lowers computational costs depending on the level of acceptable spatial discretization error.

7.3   Future Work

The current IMC implementation is unable to analyze radiation of multiple species due to memory limitations. Careful elimination of wavenumber ranges that do not contribute to the solution would decrease the size of the spectral property tables while maintaining accuracy. However, the one dimensional spectrally resolved heat flux results shown in Section 5.1.1 show that most of the spectrum is important. Given the magnitude of the epistemic uncertainty introduced by the HITEMP 2010 database, the resolution of the spectral property tables could be reduced to greatly decrease memory utilization. Additionally, the 26 temperature points used for the spectral tables are currently evenly distributed, and could be decreased by changing the distribution without sacrificing accuracy with a different distribution.

Enabling the use of multiple species will allow an uncertainty quantification of the radiative heat flux due to the four dominant radiative species rather than just the portion due to water vapor. Band overlap between the radiative species will result in epistemic uncertainty of the correlated-k spectral model used in the DOM simulations.

Crow compares DOM radiative heat flux simulation results to experimental data obtained by Brown from HIFiRE-2 scramjet ground test experiments[13, 4]. This experimental data could be used to validate the IMC method coupled with the LBL spectral tables. In the event that the simulation results do not agree with the experimental results within the range of uncertainties, this comparison could also yield valuable data for the CFD model development effort. By quantifying the sensitivity of the radiative flux to the optical sensors to the variation of input thermodynamic variables, it would be possible to provide ranges of possible thermodynamic values necessary to replicate the experimental results.

As a first step to determining the impact of the radiative thermal heat flux on the operation of the HIFiRE-2 scramjet, the radiative thermal heat flux solution should be used as an energy source in a CFD simulation. If there is a significant impact on the flowfield simulation then it will be necessary to integrate a radiative thermal transport code into a CFD code. Since there is little expected radiation-turbulence coupling, it would be sufficient to update independent radiation simulations after a number of CFD iterations as the simulation converges.

To improve the memory efficiency of the teleportation correction method, the IMC code could be modified to only use the method in areas with large temperature gradients. Since the source tilting method was demonstrated to accurately predict the emission locations of particles in low temperature gradient regions this would not result in a loss of accuracy. The magnitude of temperature gradient that would trigger the use of the teleportation correction method would depend on the problem, and would likely need to be determined before the start of a simulation by trial and error.

BIBLIOGRAPHY

BIBLIOGRAPHY

[1] Ahrens, C., and E. Larsen (2000), An exact monte carlo method for linear grey radiative transfer problems, *Transactions of the American Nuclear Society*, *83*, 340–.

[2] Beer (1852), Bestimmung der absorption des rothen lichts in farbigen fiassigkeiten, *Annalen der Physik*, *162*(5), 78–88, doi:10.1002/andp.18521620505.

[3] Bowcutt, K., A. Paull, D. Dolvin, and M. Smart (2012), Hifire: An international collaboration to advance the science and technology of hypersonic flight, in *International Congress of the Aeronautical Sciences*.

[4] Brown, M., G. Herring, K. Cabell, N. Hass, T. Barhorst, and M. Gruber (2012), Optical measurements at the combustor exit of the hifire 2 ground test engine, in *Aerospace Sciences Meetings*, American Institute of Aeronautics and Astronautics.

[5] Bynum, M., A. Storch, J. Liu, and M. Gruber (2011), Combustor operability and performance verification for hifire flight 2, in *International Space Planes and Hypersonic Systems and Technologies Conferences*, American Institute of Aeronautics and Astronautics.

[6] Center, S. U. P. (2011), Predictive simulations of multi-physics flow phenomena, with application to integrated hypersonic system, *Technical report*, Stanford.

[7] Chan, T. F., G. H. Golub, and R. J. Leveque (1983), Algorithms for computing the sample variance: Analysis and recommendations, *The American Statistician*, *37*(3), 242–247.

[8] Chandrasekhar, S. (1960), *Radiative Transfer*, Dover Books on Physics Series, Dover Publications.

[9] Chase, R. (1995), A history of the nasp program from the formation of the joint program office to the termination of the hystp scramjet performance demonstration program, in *Meeting Paper Archive*, American Institute of Aeronautics and Astronautics.

[10] Cheatham, J. R. (2010), *Truncation Analysis and Numerical Method Improvements for the Thermal Radiative Transfer Equations*, University of Michigan.

[11] Crow, A. (2013), *Thermal Radiation of Supersonic Combustion Chambers*, University of Michigan.

[12] Crow, A., I. Boyd, and V. Terrapon (2011), Radiation modeling of a hydrogen-fueled scramjet, in *Fluid Dynamics and Co-located Conferences*, pp. –, American Institute of Aeronautics and Astronautics.

[13] Crow, A., I. Boyd, M. Brown, J. Liu, and I. Boyd (2012), Thermal radiative analysis of the hifire-2 scramjet engine, in *Fluid Dynamics and Co-located Conferences*, pp. –, American Institute of Aeronautics and Astronautics.

[14] Curran, E. T. (2001), Scramjet engines: The first forty years, *Journal of Propulsion and Power*, *17*(6), 1138–1148.

[15] Do, H., S. kyun Im, M. Mungal, and M. Cappelli (2011), The influence of boundary layers on supersonic inlet unstart, in *International Space Planes and Hypersonic Systems and Technologies Conferences*, pp. –, American Institute of Aeronautics and Astronautics.

[16] Duan, L., M. P. Martin, A. M. Feldick, M. F. Modest, and D. A. Levin (2012), Study of turbulence-radiation interaction in hypersonic turbulent boundary layers, *AIAA Journal*, *50*(2), 447–453.

[17] Elasser, W. M. (1938), New values for the infrared absorption coefficient of atmospheric water vapor, *Mon. Wea. Rev.*, *66*(6), 175–178.

[18] Fleck, J., and E. Canfield (1984), A random walk procedure for improving the computational efficiency of the implicit monte carlo method for nonlinear radiation transport, *Journal of Computational Physics*, *54*(3), 508–523.

[19] Fry, R. (2004), A century of ramjet propulsion technology evolution, *Journal of Propulsion and Power*, *20*, 27–58.

[20] Gentile, N. (2001), Implicit monte carlo diffusion-an acceleration method for monte carlo time-dependent radiative transfer simulations, *Journal of Computational Physics*, *172*(2), 543 – 571.

[21] Goody, R. M. (1952), A statistical model for water-vapour absorption, *Quarterly Journal of the Royal Meteorological Society*, *78*(336), 165–169.

[22] Graham, R. (2002), *Sr-71 Blackbird: Stories, Tales, and Legends*, Mbi Publishing Company.

[23] Graziani, F., and J. LeBlanc (2000), The crooked pipe test problem, *Tech. Rep. UCRL-MI-143393*, Lawrence Livermore National Laboratory.

[24] Gruber, M. (2010), Hifire flight 2 flowpath design update, *Tech. Rep. AFRL-RZ-WP-TP-2010-2247*, AFRL-RZ.

[25] Guy, R., R. Rogers, R. Puster, K. Rock, and G. Diskin (1996), The nasa langley scramjet test complex, in *Meeting Paper Archive*, American Institute of Aeronautics and Astronautics.

[26] Hass, N., M. Gruber, A. Storch, and K. Cabell (2011), Hifire direct-connect rig (hdcr) phase i scramjet test results from the nasa langley arc-heated scramjet test facility, in *International Space Planes and Hypersonic Systems and Technologies Conferences*, American Institute of Aeronautics and Astronautics.

[27] Hill, E. M. (2011), Leos user manual, *Tech. Rep. LLNL-SM-517311*, Lawrence Livermore National Laboratory.

[28] Jackson, K., M. Gruber, and S. Buccellato (2011), Hifire flight 2 project overview and status update 2011, in *International Space Planes and Hypersonic Systems and Technologies Conferences*, pp. –, American Institute of Aeronautics and Astronautics.

[29] Jr., J. F., and J. C. Jr. (1971), An implicit monte carlo scheme for calculating time and frequency dependent nonlinear radiation transport, *Journal of Computational Physics*, *8*(3), 313 – 342.

[30] Kahan, W. (1965), Pracniques: further remarks on reducing truncation errors, *Communications of the ACM*, *8*(1), 40–.

[31] Kimmel, R., and D. Adamczak (2012), Hifire-1 background and lessons learned, in *Aerospace Sciences Meetings*, American Institute of Aeronautics and Astronautics.

[32] Koch, R., and R. Becker (2004), Evaluation of quadrature schemes for the discrete ordinates method, *Journal of Quantitative Spectroscopy and Radiative Transfer*, *84*(4), 423 – 435, eurotherm Seminar 73 - Computational Thermal Radiation in Participating Media.

[33] Kumbera, M. (2003), The opacity distribution system, *Tech. Rep. UCRL-JC-148861-ABS*, Lawrence Livermore National Laboratory.

[34] Larsen, E. W., and B. Mercier (1987), Analysis of a Monte Carlo method for nonlinear radiative transfer, *Journal of Computational Physics*, *71*, 50–64.

[35] Liu, J., and M. Brown (2012), Radiative heating in hydrocarbon-fueled scramjet engines, in *Joint Propulsion Conferences*, American Institute of Aeronautics and Astronautics.

[36] Liu, J., and S. N. Tiwari (1994), Investigation of radiative transfer in nongray gases using a narrow band model and monte carlo simulation, *Journal of Heat Transfer*, *116*(1), 160–166.

[37] Liu, J., C. Tam, T. Lu, and C. Law (2006), Simulations of cavity-stabilized flames in supersonic flows using reduced chemical kinetic mechanisms, in *Joint Propulsion Conferences*, American Institute of Aeronautics and Astronautics.

[38] Mani, M., and S. N. Tiwari (1988), Investigation of supersonic chemically reacting and radiating channel flow, *Tech. Rep. CR-182726*, NASA.

[39] Mathur, T., M. Gruber, K. Jackson, J. Donbar, W. Donaldson, T. Jackson, and F. Billig (2001), Supersonic combustion experiments with a cavity-based fuel injector, *Journal of Propulsion and Power*, *17*(6), 1305–1312.

[40] Mayer, H. (1949), *Methods of opacity calculations*, AECD-1870, Oak Ridge, Tenn.,, Technical Information Branch AEC.

[41] Mazumder, S., and M. F. Modest (1999), A probability density function approach to modeling turbulence-radiation interactions in nonluminous flames, *International Journal of Heat and Mass Transfer*, *42*(6), 971 – 991.

[42] Mckay, M. D., R. J. Beckman, and W. J. Conover (2000), A comparison of three methods for selecting values of input variables in the analysis of output from a computer code, *Technometrics*, *42*(1), 55–61.

[43] Modest, F. (1993), *Radiative Heat Transfer*, McGraw-Hill Series in Mechanical Engineering, McGraw-Hill.

[44] Modest, M. (1991), The weighted-sum-of-gray-gases model for arbitrary solution methods in radiative transfer, *Journal of Heat Transfer*, *113*(3), 650–656.

[45] Modest, M. F. (1992), The Monte Carlo Method Applied to Gases with Spectral Line Structure, *Numerical Heat Transfer Part B - Fundamentals*, *22*, 273–284.

[46] Modest, M. F. (2003), Narrow-band and full-spectrum k-distributions for radiative heat transfer-correlated- k vs. scaling approximation, *Journal of Quantitative Spectroscopy and Radiative Transfer*, *76*(1), 69–83.

[47] Moin, P. (2009), Stanford psaap center overview, AST Meeting.

[48] NASAFacts (2004), Nasa hyper-x program demonstrates scramjet technologies, *Tech. Rep. FS-2004-10-98-LaRC*, NASA.

[49] Nelson, H. (1997), Radiative heating in scramjet combustors, in *Meeting Paper Archive*, American Institute of Aeronautics and Astronautics.

[50] Pauli, A., H. Alesi, and S. Anderson (2005), The development of the hyshot flight program, in *Shock Waves*, edited by Z. Jiang, ISBN 978-3-540-22497-6, p. 31, Springer-Verlag Berlin Heidelberg.

[51] Penner, S. S. (1959), *Quantitative molecular spectroscopy and gas emissivities*, Addison Wesley Pub. Co.

[52] Planck, M. (1901), Ueber das gesetz der energieverteilung im normalspectrum, *Annalen der Physik, 309*(3), 553–563.

[53] Pomraning, G. C. (1973), *The Equations of Radiation Hydrodynamics*, Pergamon Press Ltd.

[54] Rathkopf, J. A., et al. (2000), Kull: Llnl's asci inertial confinement fusion simulation code, in *Physor American Nuclear Society Topical Meeting on Advances in Reactor Physics and Mathematics and Computation into the Next Millennium*, uCRL-JC-137053.

[55] Ross, S. (2009), *Introduction to Probability and Statistics for Engineers and Scientists*, Wiley series in probability and mathematical statistics, Academic Press/Elsevier.

[56] Rothman, L., I. Gordon, R. Barber, H. Dothe, R. Gamache, A. Goldman, V. Perevalov, S. Tashkun, and J. Tennyson (2010), Hitemp, the high-temperature molecular spectroscopic database, *Journal of Quantitative Spectroscopy and Radiative Transfer, 111*(15), 2139 – 2150, xVIth Symposium on High Resolution Molecular Spectroscopy (HighRus-2009).

[57] Rothman, L. S., et al. (1998), The HITRAN Molecular Spectroscopic Database and HAWKS (HITRAN Atmospheric Workstation): 1996 Edition, *Journal of Quantitative Spectroscopy and Radiative Transfer, 60*, 665–710.

[58] Schramm, J. M., S. Karl, K. Hannemann, and J. Steelant (2008), Ground testing of the hyshot ii scramjet configuration in heg, in *International Space Planes and Hypersonic Systems and Technologies Conferences*, American Institute of Aeronautics and Astronautics.

[59] Schuster, A. (1905), Radiation Through a Foggy Atmosphere, *Astrophysical Journal, 21*, 1.

[60] Schwarzschild, K. (1906), Ueber das gleichgewicht der sonnenatmosphare, *Gottinger Nachrichten, 21*, 41–53.

[61] Segal, C. (2009), *Scramjet Engine - Processes and Characteristics*, – pp., Cambridge University Press.

[62] Swiler, L. P., and A. A. Giunta. (2007), Aleatory and epistemic uncertainty quantification for engineering applications, in *Proceedings of the Joint Statistical Meetings, American Statistical Association*.

[63] Taine, J., and A. Soufiani (1999), Gas ir radiative properties: From spectroscopic data to approximate models, *Advances in Heat Transfer, 33*, 295 – 414.

[64] Thomas, G., and K. Stamnes (1999), *Radiative Transfer in the Atmosphere and Ocean*, Cambridge Atmospheric & Space Science, Cambridge University Press.

[65] Tien, C. (1969), Thermal radiation properties of gases, *Advances in Heat Transfer*, *5*, 253 – 324.

[66] Tiwari, S., S. Pidugu, and T. Mohieldin (1999), Radiative interactions in supersonic flows of premixed hydrogen in expanding nozzles, in *Meeting Paper Archive*, American Institute of Aeronautics and Astronautics.

[67] Vincenti, W., and C. Kruger (1967), *Introduction to physical gas dynamics*, Krieger.

[68] Wang, A., and M. F. Modest (2007), Spectral monte carlo models for nongray radiation analyses in inhomogeneous participating media, *International Journal of Heat and Mass Transfer*, *50*(19-20), 3877 – 3889.

[69] Wang, L., J. Yang, M. Modest, and D. Haworth (2007), Application of the full-spectrum -distribution method to photon monte carlo solvers, *Journal of Quantitative Spectroscopy and Radiative Transfer*, *104*(2), 297 – 304.

[70] Witteveen, J., K. Duraisamy, and G. Iaccarino (2011), Uncertainty quantification and error estimation in scramjet simulation, in *International Space Planes and Hypersonic Systems and Technologies Conferences*, American Institute of Aeronautics and Astronautics.

[71] Wollaber, A. (2008), *Advanced Monte Carlo Methods for Thermal Radiation Transport*, University of Michigan.